Energy dissipation and transport in polymeric switchable nanostructures via a new energy-conserving Monte-Carlo scheme

Dissertation

zur Erlangung des mathematisch-naturwissenschaftlichen Doktorgrades

Doctor rerum naturalium

der Georg-August-Universität Göttingen

Im Promotionsprogramm PROPHYS
der Georg-August University School of Science (GAUSS) vorgelegt

von
Marcel Simon Langenberg
aus Düsseldorf

Göttingen, 2018

Betreuungsausschuss:

Prof. Dr. Marcus Müller, Institut für Theoretische Physik, Universität Göttingen
Prof. Dr. Reiner Kree, Institut für Theoretische Physik, Universität Göttingen
Prof. Dr. Cynthia Volkert, Institut für Materialphysik, Universität Göttingen

Mitglieder der Prüfungskommission:

Referent:
Prof. Dr. Marcus Müller, Institut für Theoretische Physik, Universität Göttingen
Korreferent:
Prof. Dr. Reiner Kree, Institut für Theoretische Physik, Universität Göttingen

Weitere Mitglieder der Prüfungskommission:

Prof. Dr. Annette Zippelius, Institut für Theoretische Physik, Universität Göttingen
Prof. Dr. Cynthia Volkert, Institut für Materialphysik, Universität Göttingen
Prof. Dr. Matthias Krüger, Institut für Theoretische Physik, Universität Göttingen
Prof. Dr. Stefan Klumpp, Institut für Nichtlineare Dynamik, Universität Göttingen

Tag der mündlichen Prüfung: 9. April 2018

Kurzbeschreibung

Polymere sind Materialien, die in der Industrie eine breite Anwendung finden. Die Vorteile, in der Verwendung von Polymeren, liegen in ihrer vergleichsweise einfachen Möglichkeit der Verarbeitung, z. B. in Spritzgussverfahren oder modernsten 3D-Druck-Techniken. Polymere sind Makro-Molekül-Ketten und aus einzelnen Molekülen - Repetiereinheiten - zusammengesetzt. Im einfachsten Fall können Polymere durch lineare harmonische Ketten modelliert werden. Mit einer gewissen Abstraktionsebene besitzen Polymere ein universelles Verhalten, das durch wenige Eigenschaften beschrieben werden kann. Diese Eigenschaften sind (i) eine Längenskala, definiert durch einen mittleren End-zu-End-Abstand, R_e, eines Polymers, (ii) eine isotherme Kompressibilität, κN, welche die Stärke der ungebundenen Wechselwirkungen kontrolliert und (iii) ein invarianter Polymerisierungsgrad, $\bar{\mathcal{N}}$. In den vergangenen Jahren haben Polymere einen hohen Beitrag für Hochtechnologiesektoren, wie die Halbleiter/Chipindustrie oder die Batterieforschung, geleistet. In diesem Zusammenhang ergeben sich besonders interessannte Fragestellungen, z. B.: Wie können Mechanismen in Polymeren genutzt werden, um Energietransport bzw. thermische Transporteigenschaften kostengünstig und effizient zu nutzen. Ein vielversprechender Mechanismus ist die Selbst-Assemblierung in Mikrophasenstrukturen. Diese Mikrophasenstrukturen bilden viele Grenzflächen aus. Die Grenzflächen bilden einen thermischen Widerstand, so dass thermische Transportprozesse im Material eine Richtungspräferenz bekommen.

Diese Arbeit legt den Fokus auf thermische Transporteigenschaften dieser selbstassemblierten Mikrophasenstrukturen. Ein wesentlicher Unterschied gegenüber bisherigen theoretischen Ansätzen ist ein neues Energie-Monte-Carlo-Schema **eMC**. Dieses Monte-Carlo-Schema erlaubt, Polymersysteme auf großen Zeit- und Längenskalen zu untersuchen. Bisherige Methoden setzen wegen numerischer Instabilitäten eine sehr kleine Wahl des Zeitinkrements voraus, so dass eine Untersuchung thermischer Transportprozesse auf gleichen Skalen wie **eMC** einen zu großen Einsatz von Rechenzeit benötigen würde. Mit **eMC** können Skalen betrachtet werden, die bis *dato* Kontinuumsmodellen vorbehalten waren. Ein fundamentaler Unterschied der **eMC**-Methode gegenüber Kontinuumsmodellen ist jedoch, dass lokale Eigenschaften

der zugrundeliegenden molekularen Struktur, z. B. die spezifische Wärmekapazität, Polymerkettenkonfirmationen und Dichteunterschiede, ohne erheblichen Mehraufwand aufgelöst werde können.

In der vorliegenden Arbeit werden, ausgehend von Homopolymerschmelzen, Diblockkopolymeren, Sternpolymeren und weichen kubischen Kristallen, thermische Eigenschaften eines komplexen Polymersystems im Rahmen der Möglichkeiten des **eMC**-Schemas untersucht und qualitativ mit experimentellen Beobachtungen in Bezug gesetzt. Insbesondere wird dargestellt, dass die **eMC**-Methode einen einfachen Zugang bietet, um Effekte der thermischen Leitfähigkeit bezüglich gebildeter Grenzflächen, Dichteunterschiede und molekularer Architektur zu studieren. Insbesondere ist hervorzuheben, dass die Änderung des Löslichkeitsparameters eines Sternpolymers in einer Homopolymermischung als ein Schaltvorgang betrachtet werden kann, der eine Kontrolle der thermischen Relaxierung des Sternpolymers zulässt. Ein weiterer Bestandteil dieser Arbeit ist die Bestimmung einer Zustandsdichte (Density of States) einer mikrokanonisch betrachteten weichen Polymerschmelze, ohne interne Freiheitsgrade, mit dem Ziel, Aussagen über Propagation von Phononen zu treffen. Polymerschmelzen eine Zustandsdichte zuzuschreiben ist äußerst schwierig, da sich herausgestellt hat, dass das Verhalten von Polymerschmelzen primär von inkohärenter diffusiver Natur ist, was dem Gedanken einer stehenden kohärenten Phononen-Mode im System widerspricht. Der letzte Abschnitt beschäftigt sich mit einem möglichen Kontrollmechanismus für Energietransport auf einer höheren Abstraktionsebene. Ausgehend von den gefundenen Ergebnissen, dass die thermische Leitfähigkeit durch Grenzflächen und Polymerlängen kontrolliert werden kann, können Photoschalter eingesetzt werden, um die Selbst-Assemblierung in mikrophasen-separierte Polymerschmelzen sowie die Art der Ausbildung komplexer Grenzflächenstrukturen zu kontrollieren.

Stichwörter: Akkzeptanzkriterium, Energietransport, Energie Monte-Carlo, Diblockcopolymer, Homopolymer, interner Freiheitsgrad, Kapitza-Widerstand, reversible Nicht-Gleichgewichts-Molekulardynamiksimulation, Sternpolymer, vergröberte Molekulardynamiksimulation, weicher kubischer Kristall, Zustandsdichte

Abstract

Polymers are materials that are widely used in industry. The advantages of polymers are their comparatively simple possibility of processing, e.g, injection moulding processes, 3D printers, and self-assembly. Polymers are macromolecule chains and are composed of (simple) molecular repeating units. From a certain abstraction level, polymers have a universal behaviour that can be described by a few properties only. The most important features, which are required are (i) a length scale given by the mean end-to-end distance of a polymer, R_e, (ii) an isothermal compressibility that controls the strength of the non-bonded interactions, κN, and (iii) an invariant degree of polymerisation, $\bar{\mathcal{N}}$. In recent years, polymers also had a high impact on high-tech sectors, such as the semiconductor industry or battery research. In this context, particularly interesting issues arise, e.g., which mechanisms in polymers can be used in order to be able to use energy transport or thermal transport properties inexpensively and efficiently. A promising mechanism is the self-assembly in microphase structures. These microphase structures have many interfaces. These interface structures create a thermal resistance for an energy flow that propagates through the material, so interfaces are a possibility to control thermal transport processes by assigning directional preferences.

This work focuses on the thermal transport properties of these self-assembled microphase structures. A major difference from previous theoretical approaches is a new energy Monte-Carlo scheme **eMC**. This **eMC** scheme allows polymer systems to be studied on large time and length scales. Existing methods, e.g., energy conserving dissipative particle dynamics **eDPD**, need a very small time increment due to numerical instabilities, so that a study of thermal transport processes on the same scale as **eMC** would require too much computing time. For the first time, **eMC** enables to address scales, which until now have been reserved for continuum models. However, a fundamental difference of the **eMC** method to continuum models is that local properties of the underlying molecular structure, e.g., specific heat capacity, polymer chain confirmations and density differences can be resolved without significant additional effort.

In the present thesis the properties of homopolymer melts, diblock copolymers,

star polymers and soft cubic crystals, are examined and qualitatively related to experimental observations. In particular, it is shown that the **eMC** method provides easy access to effects on thermal conductivity with respect to formed interfaces, density differences, and molecular architecture. However, it shall be emphasised that the change in the solubility parameter of a star polymer in a homopolymer mixture, is a switching process that allows controlling the thermal relaxation of the star polymer. A further part of this thesis is the determination of a phonon density of states (**DoS**) of a microcanonically regarded soft polymer melt. Determining the **DoS** of polymer melts is extremely difficult, since it has been found that the behaviour of polymer melts is primarily diffuse. In the last section, a possible control mechanism for energy transport at a higher abstraction level is discussed. Starting from the observation that the thermal conductivity can be controlled by interfaces and polymer lengths, photoswitches are used to control the self-assembly of microphase-separated polymer melts.

Keywords: acceptance criterion, coarse-grained molecular dynamic simulations, energy transport, energy Monte-Carlo, density of states, diblocks, homopolymer, internal degree of freedom, Kapitza resistance, reverse non-equilibrium molecular dynamic simulation, star polymer, soft cubic crystal.

Contents

List of Figures

1 Introduction

The power of control tactics that polymers can provide emerges by a combination of phase transitions, macromolecular architecture, and directed self-assembly, and can be further enhanced by blending in composite materials. Different types of polymers can be used to form complex structures. The formation of different phases depends on parameters such as pressure, temperature, or the materials' incompatibility . These newly formed structures surpass the material properties of the starting materials many times over. We are primarily concerned with the questions of how interfaces can change the transport properties of a material and what mechanisms at the microscopic level as well as at the coarse-grained level influence transport properties across interfaces, such as the thermal conductivity. Assuming a low level of coarse-graining without taking internal degrees of freedom into account, the vibration spectra of a soft system are studied. The density of states is related to the transport properties of the system based on mechanical vibrations. On a coarse-grained level, the new energy Monte-Carlo (**eMC**) scheme permits including molecular mechanisms like the influence of chain length, or other binding distributions, qualitatively as well as quantitatively.

Thermal properties of polymers can be used in a wide range of applications. Most of the research approaches focus on a basic understanding of heat transport to develop control tactics and provide promising ideas for future applications. First applications of polymers in electronic circuits were already patented by Gerald Pearson at Bell Labs in 1939 [1]. He invented a resettable polymeric fuse. This fuse protects electronic circuits against over current faults. If the current is too high, the device heats up. In consequence, the polymer changes from a crystalline into an amorphous state. The conductive parts are broken and the electronic circuit is physically cut. If the temperature is reduced, the polymer performs a phase transition back to crystalline phase and becomes conductive again [1]. In the last decades, this has become a standard electronic component in low-voltage main supply circuits, especially to protect USB ports and devices. Recently, a Swedish

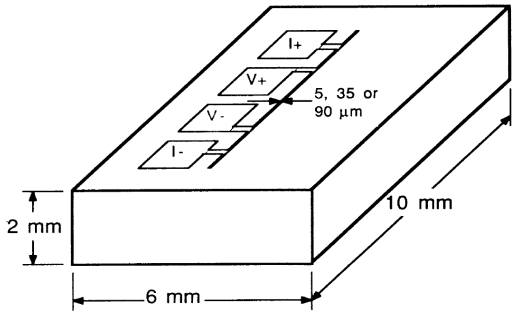

Figure 1.1 „Evaporated metal pattern produced on the face of a PMMA sample. The four pads are the connections for current leads $I+$, I and voltage leads, $V+$, V. The narrow metal line that serves as the heater and thermometer for the measurement of the thermal conductivity is at the centre of the face of the sample. Pattern made by photo-lithography (line widths 5 or 35 μm) or by evaporation through a mask (line width 90 μm)“, Reprinted with permission, Phys. Rev. B 35, 4068 (1987) [5], Copyright (1987) American Physical Society.

group invented an ionic thermo-electric gating organic transistor [2]. They made use of the Seebeck effect (also known as Peltier effect or Thomson effect), which allows the use of a thermal input at the gate of the transistor to convert a modulation in temperature to a modulation in the drain current, I [2].

Beside applications, basic research focuses on testing composite materials. These composite materials form interfaces. These interfaces cause a thermal resistance that is known as Kapitza resistance [3]. Also, elastomers with elongated liquid metal micro-droplets inclusions have been constructed. These materials are electrically insulating composites, which are highly elastic, and undergo extreme deformations (>600% strain), achieve a $\sim$ 25x increase in thermal conductivity (compared to bulk conductivity of polymethylmethacrylate (PMMA) and in a strained condition $\sim$ 50x [4].

Hence, theoretical investigation of thermal properties of polymers are a highly topical issue. Experimentally, investigation of thermal properties of polymers is very challenging. The polymers have a low glass temperature, evaporate in high vacuum, and thermal conductivity of bulk material is only one order of magnitude over vacuum. In consequence, every thermal measurement on polymers is connected with very high technical effort. This thesis is a theoretical work and does not focus on technical details of measurement. However, an introduction to some experimental setups, which allow a measurement of thermal properties, is given. This sensitizes readers to the complexity experimentalists have to handle by confirming results that have been obtained by theoretical modelling of energy transport via **eMC**.

3ω method The 3ω method is a strategy to measure the thermal conductivity. First measurements on polymers (PMMA), have been done by Cahill and Pohl in 1987 [5]. The experimental setup is sketched in fig. 1.1. The material, which is examined, is covered by a metal pattern consisting of four pads. The main idea of this method is to use the coupling between the voltage signal $U_{3\omega}$ and the change of the temperature amplitude of the heater ΔT, which allows to determine the thermal conductivity of the material, because the amplitude ΔT and phase φ depend on the thermal conductivity of the material and frequency ω. Practically, a current with frequency ω is injected to the metal structure, fig. 1.1. This corresponds to an injected thermal power with an electrical resistance R. The temperature of material and the electrical resistance have a frequency that is twice the base frequency [5]. The product of the 2ω oscillating resistance and ω oscillating current is $U_{3\omega}$, which is proportional to the temperature amplitude. In consultation with experimentalist, this method is mainly limited in the preparation by applying the metal pattern to the material - especially thin films.

Thermal reflection method The polymeric material is covered with a copper layer first. Technically, this can be done, e.g., by pulsed laser deposition. For the reflection layer, the copper is used, because it has a very good thermal conductivity. The measurement itself tracks the time-resolved reflectivity of the copper layer. Figure 1.2 represents the experimental setup and a time-resolved reflectivity of the copper layer. The red line indicates a measurement without polymers. The blue curve is a measurement of **PMMA**. In the evaluation of the measurement, the relaxation constant of this decay is related to the material's thermal conductivity. This method has been applied successfully to **PMMA** by reproducing the literature value of thermal conductivity 0.19 W/mK [6]. Beside the measurements of the bulk properties of **PMMA**, they also demonstrated that a layered tungsten/polycarbonate structure has a reduced thermal conductivity in contrast to the materials' bulk thermal properties [6]. They conclude that this can be explained by a resistance, which is induced by the formed interfaces.

Scanning thermal microscopy (SThM) The **SthM** is a technique to perform scanning thermal microscopy measurements. Therefore, a normal **AFM** probe is replaced by a probe with an integrated Palladium resistance thermometer. This thermometer will change the resistance as a function of temperature. The typical sensitivity is about 1Ω per Kelvin. These probes are commercially available, e.g.,

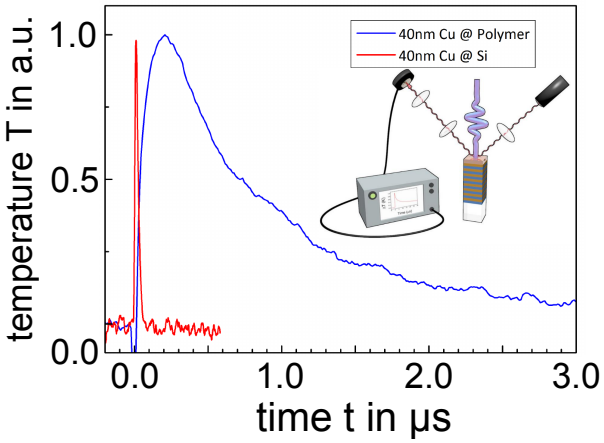

Figure 1.2 Homopolymers (**PMMA**) have been measured by thermal reflection method. Energy is placed in the copper interface and its reflection is measured. The underlying material properties control the decay of the measured signal. The relaxation constant of this decay can be related with material's thermal conductivity. Thanks to the group of Henning Ulrichs for this preliminary result.

KNT-SThM-01a by Kelvin Nanotechnology Ltd. In the last years, experimentalists made efforts to combine **SThM** with the standard 3ω method and developed 3ω SThM [7]. They performed measurements on nanowires of semiconducting polymers embedded in a matrix of aluminium and showed that there is a correlation between the orientational order and thermal conductivity. A group from the Department of Mechanical Engineering, Massachusetts Institute of Technology, was able to measure the thermal conductivity of a single nanowire. In their setup they fixed a polyethylene nano fibre between a needle and an **AFM** tip. They applied a temperature to the needle and measured the temperature at the **AFM** tip, which provided information about the thermal gradient, i.e., thermal conductivity. Surprisingly, they found out that the thermal conductivity of a single polyethylene nano fibre is about ≈ 104W m^{-1} K^{-1}, i.e., orders of magnitudes higher than the bulk properties of polyethylene 0.19 W m^{-1} K^{-1} [8].

Figure 1.3 gives an overview of some materials' thermal conductivity. One can conclude that polymers are not the best candidates to be used to improve thermal conductivities, even if single chains have been measured to have a high thermal conductivity. But the knowledge about influence of interfaces gained by the energy Monte-Carlo (**eMC**) scheme may allow to create more compact thermal polymeric insulators and gives rise to nice control tactics of energy transport in general. The

[1]Selected values of thermal conductivity under standard conditions https://en.wikipedia.org/wiki/List_of_thermal_conductivities, April 12, 2018

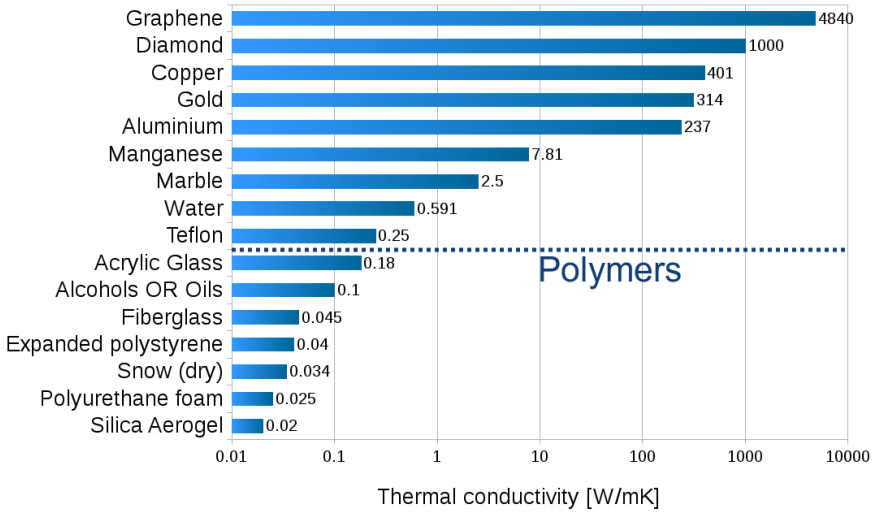

Figure 1.3 Thermal conductivity of selected materials, sorted in descending order, and plotted in a logarithmic scale. Thermal conductivity of polymers is of the order of the blue dashed line. The values are for atmospheric pressure at around 293 Kelvin [1].

experimental results suggest that thermal conductivity is influenced by orientational order, molecular architecture, and interfaces. Hence, a theoretical model is needed that captures all relevant influences. In the last decades, theoretical methods in form of efficient simulation techniques have been developed. These simulation techniques base on models, which address specific effects or physical mechanisms respectively according to a specific time and length scale. Time and length scales are one way to group these different methods. First-principle calculations using density functional theory (DFT) give rise to energies of atomic configurations, lattice configurations, vibration spectra, and force fields. Moleculardynamic simulations (MD-simulations) address the physical movements of atoms and molecules by solving classic equations of motion. Interactions of molecules, and atoms are defined by force fields or potentials respectively, which may depend on positions, charge, angle etc. This method provides access to thermodynamic properties that are not available through direct experiments. Studying these systems emphasizes that structure formation and equilibrium can be described by a minimal set of parameters: connectivity along the molecule, near-incompressibility, and repulsion. This is typical for the mesoscopic scale and specifies coarse-grained (**CG**) models. These **CG** models fluently pass over to continuum model descriptions. **CG** models are a good approach to investigate thermal properties on long time and length scales. An established technique therefore is energy conserving dissipative particle dynamics (**eDPD**) [9, 10]. But this method

has problems in numerical stability of the first-order integration scheme of stochastic differential equations of motions, which motivated us to develop a new Monte-Carlo Scheme (**eMC**) to model energy transport properties of polymers with high accuracy [11].

Outline This thesis is structured into three main parts. In the first part the theoretical principles of transport phenomena, which will end up in the thermal diffusion equation, are introduced. We give a brief introduction into the concept of phonons and density of states in general and at interfaces, respectively. The second part treats simulation techniques, viz., a detailed description of the new **eMC** scheme and how to rank **eMC** obverse other methods, i.e., **eDPD**. In the third part, the focus is on results of coarse-grained simulations performed with and without the **eMC** scheme. A rescaling of parameters will yield invariant thermal properties of the polymer melt. Stepwise, the complexity of the polymers' structure is increased, and the complexity of thermal transport that emerges is studied.

2 Theoretical Concepts

In this chapter, the fundamental concepts of transport phenomena are introduced. From this general transport phenomena, we identify the heat flux in first-order approximation and deduce an explicit form of Fourier's law. Furthermore, the thermal diffusion equation is deduced from these concepts. Finally, basic concepts of phonons and approaches to express their characteristics in analytical models are presented.

2.1 Transport phenomena

In general, transport properties are distinguished between mass, momentum, and energy transfer. Their physical mechanisms can be described in a first approximation by linear dependencies of fluxes on forces: mass diffusion (Fick's law), viscous flow (Newton's friction), and energy diffusion (Fourier's law). Assuming irreversible processes, these mechanisms follow general reciprocal relations, which have been derived by Onsager [12]. In the next section, hydrodynamic equations of a viscous fluid are derived.

2.1.1 Boltzmann equation

The Boltzmann equation is a differential equation describing the temporal evolution of a probability density function $f(\vec{r}, \vec{p}, t)$. This function depends on momentum $\vec{p}$, spatial position $\vec{r}$, and time t. Indeed, the idea is not to describe each individual particle but their probability densities. Thus, even if the underlying system is comprised of millions of particles, these particles are grouped to their chance to be encountered at a specific state defined by position and momentum. Hence, $f(\vec{r}, \vec{p}, t)\mathrm{d}\vec{p}\mathrm{d}\vec{r}$ describes the probability at time t for a particle of the underlying system, which is at position $\vec{r}$, to have a momentum in range $\mathrm{d}\vec{p}$ around $\vec{p}$, in volume

element d^3r.

$$\frac{\mathrm{d}f}{\mathrm{d}t} = \frac{\partial f}{\partial t} + \vec{v}\cdot\nabla_r f + \vec{F}\cdot\nabla_p f = \left(\frac{\partial f}{\partial t}\right)_{\mathrm{coll}} \tag{2.1}$$

This equation describes the interplay between the total time derivative of f and the collision integral $(\partial f/\partial t)_{\mathrm{coll}}$. Hence, the total differential of f, $\mathrm{d}f = \frac{\partial f}{\partial t}\mathrm{d}t + \nabla_r f d\vec{r} + \nabla_p f d\vec{p}$, has been rewritten by expression $d\vec{r} = \vec{p}\mathrm{d}t/m$ and $d\vec{p} = \vec{F}\mathrm{d}t$. $\vec{F}$ denotes the applied forces a priori independent of the velocities $\vec{v} = \frac{\vec{p}}{m}$. The most challenging part in the Boltzmann equation is the construction of the collision term. In the following considerations, the collision is based on binary collisions of two particles, which is known as „Stosszahlansatz“, at a specific position $\vec{r}$. Hence, a collision is characterised by two old momenta, $\vec{p}_{1\,\mathrm{old}}$, $\vec{p}_{2\,\mathrm{old}}$, and two new momenta, $\vec{p}_{1\,\mathrm{new}}$, $\vec{p}_{2\,\mathrm{new}}$. A collision is elastic, thus momentum and energy are conserved [13]. These momenta have a probability density, $f(\vec{r}, \vec{p}_{1\,\mathrm{old}}, t)$, which is written into a short form $f(\vec{p}_{1\,\mathrm{old}})$, $f(\vec{p}_{2\,\mathrm{old}})$, $f(\vec{p}_{1\,\mathrm{new}})$ and $f(\vec{p}_{2\,\mathrm{new}})$. The difference of old and new probability densities (the gain and loss term) is weighted by the differential cross-section of the collision $W(|\vec{p}_{1\,\mathrm{old}} - \vec{p}_{2\,\mathrm{old}}|, \vartheta)$ with scattering angle, ϑ, and the magnitude of the momentum $|\vec{p}_{1\,\mathrm{old}} - \vec{p}_{2\,\mathrm{old}}|$. The complete expression

$$\begin{aligned}\left(\frac{\partial f}{\partial t}\right)_{\mathrm{coll}} = &\int\int\int |\vec{p}_{1\,\mathrm{old}} - \vec{p}_{2\,\mathrm{old}}| \cdot W(|\vec{p}_{1\,\mathrm{old}} - \vec{p}_{2\,\mathrm{old}}|, \vartheta)\times \\ &[f(\vec{p}_{1\,\mathrm{old}})f(\vec{p}_{2\,\mathrm{old}}) - f(\vec{p}_{1\,\mathrm{new}})f(\vec{p}_{2\,\mathrm{new}})]\,\mathrm{d}\vec{p}_{1\,new}\mathrm{d}\vec{p}_{2\,new}\mathrm{d}\vartheta\end{aligned} \tag{2.2}$$

is integrated over the new momenta $\vec{p}_{1\,\mathrm{new}}$, $\vec{p}_{2\,\mathrm{new}}$ and the solid angle $\mathrm{d}\vartheta$. It can be shown that the collision term weighted by any collision invariant[1], $\chi(r, p, t)$, integrated by a momentum $\vec{p}$, is zero, because the magnitude of the momentum, $|\vec{p}_{1\,\mathrm{old}} - \vec{p}_{2\,\mathrm{old}}|$, is conserved in a collision

$$\int \chi(\vec{r}, \vec{p}, t)\left(\frac{\partial f}{\partial t}\right)_{\mathrm{coll}} \mathrm{d}\vec{p} = 0. \tag{2.3}$$

Collision invariants, $\chi(\vec{r}, \vec{p}, t)$, are mass, kinetic momentum, and kinetic energy [14]. In eq. (2.3), the right-hand side of the Boltzmann equation, i.e., total time derivative, eq. (2.1), is inserted. This expression can be used to formulate a general

[1] Collision invariants are mass, energy, and momentum. They are conserved in an elastic binary collision

balance theorem for any collision invariant $\chi(\vec{r},\vec{p},t)$

$$\int \left[\chi(\vec{r},\vec{p},t)\left(\frac{\partial f}{\partial t}+\vec{v}\cdot\nabla_r f+\vec{F}\cdot\nabla_p f\right)\right]\mathrm{d}\vec{p}=0. \tag{2.4}$$

We define that the average, $\langle M\rangle$, of any function M is expressed by $\langle M\rangle=\frac{\int Mf\mathrm{d}\vec{p}}{\int f\mathrm{d}\vec{p}}$. This allows us to rewrite eq. (2.4) into

$$\frac{\partial}{\partial t}\langle n(\vec{r},t)\chi\rangle-n(\vec{r},t)\left\langle\frac{\partial\chi}{\partial t}\right\rangle+\nabla_r\left\langle n(\vec{r},t)\chi\vec{v}\right\rangle-n(\vec{r},t)\left(\langle\vec{v}\nabla_r\chi\rangle+\left\langle\vec{F}\nabla_p\chi\right\rangle\right)=0. \tag{2.5}$$

Here, $n(\vec{r},t)=\int f(\vec{r},\vec{p},t)\mathrm{d}\vec{p}$ represents the local density close to an equilibrium stage and is independent of the velocities or momenta, respectively. Next, the general balance theorem is used to derive the hydrodynamic equations, using the collision invariant's mass, momentum, and kinetic energy. Hence, a **local balance equation for mass** is formulated by inserting $\chi=m$ into eq.(2.5), which results in the continuity equation. The change of this probability distribution is characterised by

$$\frac{\partial(mn(\vec{r},t))}{\partial t}+\nabla_r\cdot((mn(\vec{r},t))\vec{u})=\frac{\partial\rho}{\partial t}+\nabla_r\cdot(\rho\vec{u})=0. \tag{2.6}$$

$\rho=\rho(\vec{r},t)=mn(\vec{r},t))$ is the local mass density and $\vec{u}=\vec{u}(\vec{r},t)=\frac{1}{n(\vec{r},t))}\int\vec{v}f(\vec{r},\vec{p},t)\mathrm{d}\vec{p}$ is the local mean velocity averaged over all velocities that occur at position $\vec{r}$. Naturally, a local mean velocity $\vec{u}$ is only valid if velocities are distributed around a mean value, otherwise it is not meaningful to calculate $\vec{u}$. The product $\rho\vec{u}$ represents a convective flux of mass. By inserting $\chi=m\vec{v}$ in the general balance equation, eq. (2.5), one obtains the **local balance equation for the kinetic momentum**. $\mathcal{P}$ represents the pressure tensor, which includes the viscous stress tensor and the hydrostatic pressure with components $\mathcal{P}_{\mathrm{ij}}=\rho\langle(v_i-u_i)(v_j-u_j)\rangle$. This yields the local balance equation

$$\frac{\partial(\rho\vec{u})}{\partial t}+\nabla_r\cdot(\rho\vec{u}^{\,2}+\mathcal{P})=\frac{\rho}{m}\vec{F}. \tag{2.7}$$

In this notation, the gradient of the pressure tensor is defined as $\nabla_r\mathcal{P}=\sum_j\partial_j\mathcal{P}_{\mathrm{ij}}$. In case of a perfect fluid, this equation is also known as the Euler equation. A perfect fluid does not have heat conduction, shear stress, or a viscosity. The external force

$\frac{\rho}{m}\vec{F}$ is a source term and inhibits the conservation of momenta.

Finally, the **local balance equation for the energy** is derived by inserting the expression for energy, $\chi = m/2|\vec{v} - \vec{u}(\vec{r},t)|^2$, into eq. (2.5). Hence, the mean of the change of the energy by time is zero, $\langle \partial_t (m/2|\vec{v} - \vec{u}(\vec{r},t)|^2)\rangle = 0$. The internal energy, e_{int}, per unit mass is defined in terms of velocities: $e_{\text{int}} = \langle |\vec{v} - \vec{u}(r,t)|^2 \rangle$. The temporal change of the local density of energy per unit mass depends on the change of the flux $\vec{J}_Q$ and convective flux $\rho e \vec{u}$, or gradient, respectively. The balance equation for the energy is

$$\frac{\partial \rho e_{\text{int}}}{\partial t} + \nabla_r (\vec{J}_Q + \rho e_{\text{int}} \vec{u}) = -\mathcal{P} \cdot \nabla_r \vec{u}. \tag{2.8}$$

The expression on the right handside represents a source term. The convective flux is defined by $\vec{J}_Q = \rho(\vec{r},t)\langle (\vec{v} - \vec{u}(r,t)) \cdot e_{\text{int}} \rangle = \frac{\rho(\vec{r},t)}{2} \langle (\vec{v} - \vec{u}(r,t)) \cdot |\vec{v} - \vec{u}(r,t)|^2 \rangle$. The energy is not conserved, because of the source term $-\mathcal{P} \cdot \nabla_r \vec{u}$. The balance equations for mass, kinetic momentum, and internal energy lead to the hydrodynamic equations that constitute the idea of dissipative particle dynamics. However, the calculation of the heat flux and the pressure tensor needs a solution of the Boltzmann equation, because flux $\vec{J}_Q$ and pressure tensor $\mathcal{P}$ are defined by averages over functions of momenta $\vec{p}$. Thus, a solution for the Boltzmann equation, i.e., calculating an explicit form for the probability density distribution, $f(\vec{r},\vec{p},t)$, is needed. The explicit form of $f(\vec{r},\vec{p},t)$ allows for a quantitative calculation, e.g., the flux $\vec{J}_Q$. A common strategy to get solutions of the Boltzmann equation is the Chapman-Enskog expansion, for an introduction cf. [15, 16]. The main idea is to expand the probability density distribution f around a probability distribution function f^0, which is in equilibrium, by an expansion parameter ξ. The probability density distribution, f, is written in the form

$$f = \frac{1}{\xi}(f^{(0)} + \xi f^{(1)} + \xi^2 f^{(2)} + \xi^3 f^{(3)} + \dots). \tag{2.9}$$

This expansion will be valid if one claims that the influence of higher-order terms is decreasing, $f^{(0)} \gg f^{(1)} \gg f^{(2)}$. The expansion to zeroth-order $f^{(0)}$ covers a perfect fluid without heat conduction, shear stress and viscosity[2]. Hence, in a perfect fluid dissipative mechanisms are neglected. An expansion up to first-order results

[2] The expansion parameter is the dimensionless ratio between the mean free path and the characteristic length of the system. For a fluid, the mean free path is much smaller than the characteristic length of the system. Hence, if ξ is small the equilibrium distribution f_0 is weighted at most.

in hydrodynamic equations of a viscous fluid. This viscous fluid has dissipative transport coefficients, thermal conductivity, and a viscosity coefficient, respectively. The zeroth-order expansion of the Boltzmann equation is solved by the Boltzmann distribution,

$$\begin{aligned} f^{(0)}(\vec{r},\vec{p},t) &= \frac{n(\vec{r},t)}{(2\pi m k_{\mathrm{B}} T(\vec{r},t))^{3/2}} \exp\left(-\frac{m|\vec{p}-\vec{u}(\vec{r},t)|^2}{2k_{\mathrm{B}}T(\vec{r},t)}\right) \\ &= \frac{n(\vec{r},t)}{(2\pi m k_{\mathrm{B}} T(\vec{r},t))^{3/2}} \exp\left(-\frac{mU^2}{2k_{\mathrm{B}}T(\vec{r},t)}\right), \end{aligned} \tag{2.10}$$

which covers the equilibrium state. $n(\vec{r},t)$ is the local density at spatial position r and time t close to equilibrium. $T(\vec{r},t)$ is the temperature at spatial position $\vec{r}$ and time t [3]. For later calculations, the relative velocity, $\vec{U} = \frac{\vec{p}}{m} - \vec{u}(r,t)$, is defined. The Chapman-Enskog expansion, eq. (2.9), is used to expand the Boltzmann equation up to the first-order in a relaxation time approximation. Relaxation time τ in this context means that the collision term's deviations from the distribution function f from its equilibrium state f_0 are small, $\left(\frac{\partial f}{\partial t}\right)_{\mathrm{coll}} \approx \frac{f-f^{(0)}}{\tau(\vec{v})}$. Hence, τ characterises the time the system needs to relax back to an equilibration state; in general, this can depend on velocities, too. The Boltzmann equation in relaxation time approximation reads

$$\frac{\partial f}{\partial t} + \vec{v}\cdot\nabla_r f + \vec{F}\cdot\nabla_p f = -\frac{f-f^{(0)}}{\tau(\vec{v})}. \tag{2.11}$$

This expression is also known as Bhatnagar-Gross-Krook (BKG) equation [17]. Inserting the expansion, eq. (2.9), up to first-order, into the relaxation time approximation, gives the formal assumption for

$$f^{(1)} \approx -\tau(\vec{v})\left(\frac{\partial}{\partial t} + \vec{v}\cdot\nabla_r + \vec{F}\nabla_p\right) f^{(0)}. \tag{2.12}$$

Inserting[4] the Boltzmann distribution, $f^{(0)}$, eq. (2.10), into the formal assumption

[3] The local temperature $T(\vec{r},t)k = \frac{m}{3n(\vec{r},\vec{p},t)}\int |\vec{v}-\vec{u}(\vec{r},t)|^2 f(\vec{r},\vec{p},t)$, is a defined by an integral over the averaged velocity $\vec{u}$, velocity $\vec{v}$, and mass m.

[4] The Boltzmann equation is characterised by density $\rho \sim n(\vec{r},t)$, temperature, $T(\vec{r},t)$, and velocity $\vec{u}(\vec{r},t)$. Hence, calculation of the gradients ∇_r and ∇_p is non-trivial. The partial derivatives of $f^{(0)}$ are: with respect to density $\frac{\partial f^{(0)}}{\partial \rho} = \frac{f^{(0)}}{\rho}$, with respect to temperature $\frac{\partial f^{(0)}}{\partial T} = \frac{1}{T}\left(\frac{m}{k_{\mathrm{B}}T}\vec{U}^2 - \frac{3}{2}\right) f^{(0)}$, and with respect to velocity $\frac{\partial f^{(0)}}{\partial u_{\mathrm{i}}} = \frac{-mu_i}{k_{\mathrm{B}}T} f^{(0)}$. The total derivative with respect to density is zero, eq. (2.6). For the velocity u_i one uses the local balance equation of kinetic momentum, eq. (2.7) , and for temperature the local balance

for $f^{(1)}$, eq. (2.12), finally results in

$$f^{(1)} = -\tau(\vec{v}) \cdot f^{(0)} \left[\frac{1}{T} (\vec{U} \cdot \nabla_r T) \left(\frac{m}{2k_\mathrm{B}T} \vec{U}^2 - \frac{5}{2} \right) + \frac{1}{k_\mathrm{B}T} \Lambda_{\mathrm{ij}} \left(\vec{U}_\mathrm{i} \vec{U}_\mathrm{j} - \frac{1}{3} \delta_{\mathrm{ij}} \vec{U}^2 \right) \right].$$

Here, Λ_{ij} is a symmetric tensor $\frac{m}{2} \left(\frac{\partial u_\mathrm{j}}{\partial x_\mathrm{i}} - \frac{\partial u_\mathrm{i}}{\partial x_\mathrm{j}} \right)$. This result yields the flux

$$\vec{J}_Q^{(1)} = -\frac{\tau m^4}{2} \int \vec{U} \cdot U^2 \left(\frac{m}{2k_\mathrm{B}T} U^2 - \frac{5}{2} \right) \frac{\vec{U} \nabla T}{T} f^{(0)} \mathrm{d}\vec{U} \tag{2.13}$$

$$= -\bar{\lambda}_\mathrm{T} \nabla_r T = -\left(\frac{5 \cdot n(\vec{r}, t) \cdot k_\mathrm{B} T \tau}{2m} \right) \delta_{\mathrm{ij}} \nabla_r T \tag{2.14}$$

in the first-order approximation. In eq. (2.14), Fourier's law is identified: thermal flux is proportional to the temperature gradient and a local thermal conductivity. The thermal conductivity is a tensor $\bar{\lambda}_\mathrm{T}$, which is proportional to the unit matrix, $\bar{\lambda}_\mathrm{T} = \lambda \mathbb{1}$. This expression allows us to get an impression to properties that influence the thermal conductivity, i.e., density, and allows us perform simulations that focus on these different parameters, sec. 4.

2.1.2 Thermal diffusion equation (TDE)

In the previous section, the local balance equations for mass, momenta, and energy have been derived, and the flux has been calculated in first-order approximation, which allowed to identify Fourier's law, eq. (2.14). Hence, the explicit form of the thermal flux $\vec{J}^Q$ can be inserted into the local balance equation for the energy e_int, eq. (2.8), and the energy density is related to a local temperature by $\frac{2e_\mathrm{int}m}{3k_\mathrm{B}} = T$. The fluid is incompressible, and the divergence is $\nabla \vec{u} = 0$. Hence, there are no sources or sinks. Additionally, it is assumed that the mean velocity of the fluid is much smaller than the velocity $\vec{v}$, and this velocity is much smaller than the speed of sound, so that the symmetric tensor Λ vanishes [14]. Finally, the simplified form of local balance equation of energy reads

$$\rho c_p \frac{\partial T}{\partial t} - \nabla_r \cdot (\lambda \nabla_r T) = 0. \tag{2.15}$$

Here, c_p is the specific heat capacity at constant pressure per unit mass. In this equation, it is a specific heat at constant pressure, because local density and local temperature are not decoupled. If the thermal conductivity is macroscopic and

equation of energy, eq. (2.8), or temperature, respectively.

independent of spatial position, it becomes independent from the gradient. Hence, the gradients, eq. (2.15), are merged to a Laplacian,

$$\frac{\partial T}{\partial t} = \frac{\lambda}{\rho c_p} \triangle T. \tag{2.16}$$

The ratio $\frac{\lambda}{\rho c_p} = D_T$ represents the thermal diffusion constant. The energy Monte-Carlo method will be used to investigate thermal properties of a polymer melt. Later on, computational methods are presented. These methods enable us to simulate thermal transport properties in polymer melts, sec. 3.3. At this point, it is important to emphasise that the measurements of thermal conductivities rely on a temperature profile in steady-state. In the stationary state, the time derivative vanishes and the linear dependence follows from Fourier's law. Calculating solutions of a thermal diffusion equation is labourious, especially if complicated boundary conditions are introduced [18].

TDE as an initial value problem A common strategy to solve an initial-value problem of the heat equation is to use a fundamental solution. This fundamental solution is calculated by inserting a δ-distribution to the thermal diffusion equation. The fundamental solution is also called *heat kernel* and takes the form

$$H(\vec{x}, t) = \frac{1}{(4\pi D_T t)^{n/2}} \exp\left(\frac{(\vec{r} - \vec{r}')^2}{4 D_T t}\right). \tag{2.17}$$

Small n in this context is the dimension of $\vec{r}$. Given a temperature configuration $T(\vec{r}, t = 0)$ at time $t = 0$, all homogeneous initial value problems can be solved by a convolution of the heat kernel

$$T(\vec{r}, t) = \frac{1}{(4\pi D_T t)^{\frac{n}{2}}} \int_{\mathbb{R}^n} T(\vec{r}, t = 0) \exp\left(\frac{(\vec{r} - \vec{r}')^2}{4 D_T t}\right) \mathrm{d}^n r'. \tag{2.18}$$

Here, $T(\vec{r}, t = 0)$ is the initial condition of the thermal diffusion equation **TDE**. n sets the dimension that is considered. If a δ-function at position $\vec{r}$ is used as an initial condition, the integral is solved, and it remains the heat kernel. This result enables us to measure the thermal diffusion constant D_T of a polymer melt in simulations: the system can be initialised with a localised peak in the temperature profile whose decay can be tracked [11].

2.2 Analytical models of the density of states

In simulations, a density of phonon states (**DoS**) is calculated. Hence, an overview of analytical approaches to a **DoS** are presented. Phonons describe vibrations in a material. Hence, a phonon corresponds to an elastic wave and designates a normal mode of vibration. The modes can be divided in an acoustic and an optical branch. Acoustic phonons are transversal or longitudinal and exist in every basis. A three-dimensional system, which is uniformly composed by a mono-atomic basis, typically has two transversal and one longitudinal acoustic mode. These modes describe a collective movement that affects all particles, i.e., a longitudinal mode can be interpreted as a pressure wave that propagates through the system. Optical phonons are observed in systems that have at least a basis composed of two different particles. Hence, optical modes describe the opposed movement of these particles, i.e., their local movement is in a contrary phase. Therefore, the optical branch has higher frequencies than the acoustic branch [19]. Phonons are often described by coherent or incoherent characteristics. In this context, coherent acoustic phonons could be pressure or shear waves propagating ballistically in solids. Ballistic motion of particles is characterised by a mean free path, which is the time between two collisions wherein momenta are unaltered. Coherent optical phonons are modes of in-phase atomic vibrations that are extended to a specific range. Knowing all modes of a system allows us to define a phonon density of states, which, i.e., dictates the heat capacity of a material and thereby the thermal properties. Especially analytical models, i.e., the Debye model, are used to calculate the thermal boundary resistance by an acoustic mismatch model (**AMM**) or a diffusive mismatch model (**DMM**) approach. In general, all analytical models for a **DoS**, follow the same strategy: calculate the **DoS**, $D(\omega)$, by the integral

$$D(\omega)\mathrm{d}\omega = \left(\frac{L}{2\pi}\right)^3 \int_{\text{shell}} \mathrm{d}^3k. \tag{2.19}$$

The integration over the volume of the shell in k space counts all the states in the frequency interval $[\omega : \omega + \mathrm{d}\omega]$, for a given dispersion relation $\omega(\vec{k})$.

2.2.1 Einstein model of the density of states

The Einstein model was proposed by Einstein in 1907 [20, 21]. It is one of the first quantum-mechanical approaches to predict the specific heat capacity of a solid. The

model relies on several assumptions: all atoms vibrate harmonically, isotropically, and uncorrelated with the same frequency ω_E around their equilibrium positions. ω_E is the Einstein frequency and fulfils the relation $\omega_\mathrm{E}\hbar = k_\mathrm{B}\theta_E$. θ_E is the Einstein temperature. The density of states results in a delta function centred around ω_E

$$D(\omega) = 3N\delta(\omega - \omega_\mathrm{E}). \tag{2.20}$$

Here, $3N$ is the number of oscillators. This expression can be used to calculate the energy

$$E = \int_0^\infty 3N\delta(\omega - \omega_\mathrm{E}) \left(\frac{1}{2} + n(\omega)\right) \hbar\omega_\mathrm{E} \, \mathrm{d}\omega = 3Nk_\mathrm{B}\theta_\mathrm{E} \left(\frac{1}{2} + \frac{1}{\exp(\theta_E/T) - 1}\right) \tag{2.21}$$

of the system. $n(\omega)$ is the occupation probability and follows the Bose-Einstein statistics. From basic thermodynamic relations the specific heat capacity is calculated by the derivative from eq. (2.21) with respect to the temperature. This results in the specific heat capacity of a solid described by the Einstein model.

$$c_V = \left(\frac{\partial E}{\partial T}\right)_V = 3Nk_\mathrm{B} \left(\frac{\theta_\mathrm{E}}{T}\right)^2 \left(\frac{\exp(\theta_\mathrm{E}/T)}{(\exp(\theta_\mathrm{E}/T) - 1)^2}\right) \tag{2.22}$$

For high temperatures, this value becomes $3Nk_\mathrm{B}$, which is known as the Dulong-Petit value. At low temperatures, this model is not a good assumption, because it decreases with $\exp(\theta_\mathrm{E}/T)$ but it is experimentally known that it decreases with T^3, cf. eq. (2.27), [19].

2.2.2 Debye model of the density of states

The Debye model is a direct consequence of the Einstein model, because it assumes a phonon-dispersion relation that is not constant but linear: $\omega = v \cdot k$. ω represents the frequency and k represents a phonon-wave vector, which scales linearly with a phase velocity, v. The **DoS** will account for the number of modes per unit frequency. The system consists of a three-dimensional periodic cubic lattice with edge length $L = L_x = L_y = L_z$ and the volume $V = L^3$. In consequence, the phonon-wave vector has to fulfil the condition

$$\exp(i(k_x x + k_y y + k_z z)) = \exp(i(k_x(x + L) + k_y(y + L) + k_z(z + L))), \tag{2.23}$$

and can take values from $k_\mathrm{i} = \pm\frac{2n\pi}{L}$ with $n \in [0, 1, 2 \ldots, N]$, and $\mathrm{i} = x, y, z$. Each volume of $\left(\frac{2\pi}{L}\right)^3$ is allowed to have one value of a $\vec{k}$ vector. The total number is $\left(\frac{L}{2\pi}\right)^3$ times the volume of the unit sphere with radius k_D (maximum allowed vector), $N = \frac{4\pi}{3}\left(\frac{k_\mathrm{D}\cdot L}{2\pi}\right)^3$ [19]. Finally, a density of states in three dimensions is determined:

$$D(\omega) = \frac{\mathrm{d}N}{\mathrm{d}\omega} = \frac{K^2}{2\pi^2}\frac{\mathrm{d}K}{\mathrm{d}\omega} = \frac{V}{2\pi^2 v^3}\omega^2. \tag{2.24}$$

In the last step, the phonon-dispersion relation $\omega = v \cdot k$ of the Debye approximation is inserted. The form of $D(\omega)$ implies a first qualitative scaling of the **DoS** - $D(\omega) \propto \omega^2$. The maximum frequency

$$\omega_\mathrm{D} = \left(\frac{6\pi^2 v^3 N}{V}\right)^{\frac{1}{3}} \tag{2.25}$$

(Debye frequency) is determined by the maximum number of total modes N. The limiting phonon-wave vector is taken from the dispersion relation $k_\mathrm{D} = \frac{\omega_\mathrm{D}}{v}$. Integration over all possible frequencies from 0 up to ω_D yields the energy

$$E = \frac{3V\hbar}{2\pi^2 v^3}\int_0^{\omega_\mathrm{D}} \frac{\omega^3}{\exp\left(\frac{\hbar\omega}{k_\mathrm{B}T}\right) - 1}\mathrm{d}\omega \tag{2.26}$$

of the system, cf. (2.21). The multiplication by $3N$ already includes the assumption that the velocity of the phonons is independent from its polarisation. The energy, E, gives rise to the model's specific heat capacity, c_V, via the derivative of E with respect to temperature at constant volume. In the low temperature limit, the integral, $\int_0^\infty \frac{x^3}{e^x-1}\mathrm{d}x$, for $x \to \infty$ is solved by $\frac{\pi^4}{15}$. This solution gives an expression for the energy in the limit of small temperatures, $E \overset{T\to 0}{=} \frac{3\pi^2 N k_\mathrm{B} T^4}{5\theta_D^3}$. Here, $\theta_\mathrm{D} = \frac{\hbar k_\mathrm{B}}{v}\left(\frac{6\pi^2 N}{V}\right)^{1/3}$ indicates the Debye temperature in terms of ω_D. Under these conditions, the specific heat capacity at low temperatures yields

$$c_V \overset{T\to 0}{=} \frac{12\pi^2 N k_\mathrm{B}}{5}\left(\frac{T}{\theta_\mathrm{D}}\right)^3, \tag{2.27}$$

which is known as the **Debye T^3 law** [19]. At higher temperatures, this law fails because of anharmonic crystal interactions.

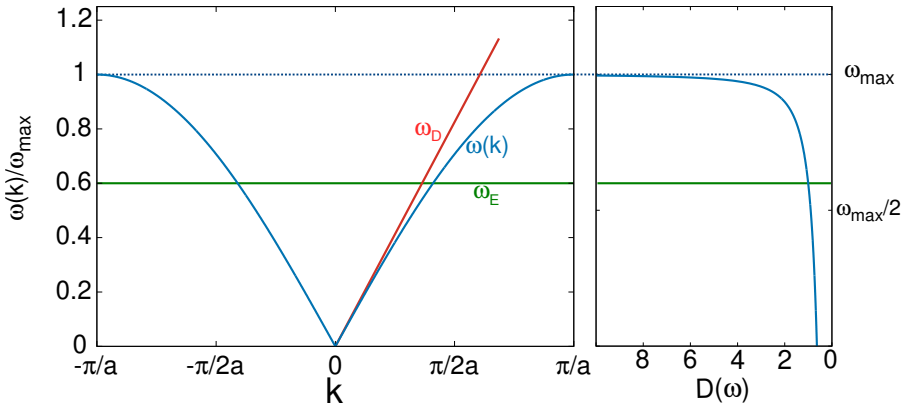

Figure 2.1 Dispersion relation $\omega(k)$ and the **DoS** of a 1D harmonic chain, eq.(2.30). ω_{max} is the maximum frequency of the system. The dispersion relation has just one acoustic branch, because segments have equal mass. For a qualitative comparison, the Einstein frequency ω_{E} and Debye frequency ω_{D} are added.

2.2.3 1D harmonic chain

The one-dimensional harmonic chain with N segments is a classic example to determine an analytical form of the **DoF**. Single mass centres m and positions x_{n} are connected by a harmonic potential with spring constant K. The equation of motion of one x_{n} is described by a coupled second-order differential equation,

$$m\ddot{x}_{\mathrm{n}} + K\left(2x_{\mathrm{n}} - x_{\mathrm{n}-1} + x_{\mathrm{n}+1}\right) = 0. \tag{2.28}$$

The ends of the chains are connected so that $x_{\mathrm{N}+1} = x_0$ (Born-von-Karman boundary condition). Inserting the ansatz $x_{\mathrm{n}}(t) = A \cdot \exp\left(ikan - \omega t\right)$ gives rise to the dispersion relation

$$\omega(k) = \frac{2K}{m}\left|\sin\frac{ka}{2}\right|. \tag{2.29}$$

The maximum frequency along the chain is given by $\omega_{\mathrm{max}}^2 = \frac{2K}{m}$. The dispersion relation can be used to calculate the density of states for a one-dimensional harmonic chain

$$D(\omega) = \frac{2Na}{\pi}\frac{1}{\sqrt{\omega_{\mathrm{max}}^2 - \omega^2}}. \tag{2.30}$$

This **DoS** can be observed in a system comprised of polymers without non-bonded interactions, cf. appx. 6.2.

2.3 Identifying the density of states of a system

The density of states (**DoS**) counts the number of states for a given interval of frequency, or energy, respectively. Calculating the **DoS** will specify transport coefficients at the lowest state. We determine a fully classic **DoS** based on the harmonic potentials given by Gaussian harmonic bonds and soft repulsive non-bonded interactions. There are two strategies that can be used to determine the **DoS** of a polymeric system.

The first strategy uses a cosine transformation of the velocity auto correlation function (**VAC**) of a soft MD fluid, which was first proposed by Rahman [22] and extended by Grest [23–25]. Their approach follows the idea of a pendulum. They instantaneously set the kinetic energy to zero and observe the different vibrational modes of kinetic temperature via a one-sided cosine transformation of relaxing temperature fluctuations.

This strategy has been expanded by performing a one-sided cosine transformation of the **VAC** and has been adopted successfully to Lennard-Jones fluids as well [26–29]. The second strategy to determine the **DoS** uses the Hessian matrix. The Hessian matrix is a harmonic approximation of the potential around a force-free state or mechanical equilibrium, respectively. This implies coefficients of this matrix can be understood as the force of particle i in direction $\alpha = \{x, y, z\}$, which acts on a particle j in direction $\beta = \{x, y, z\}$, which was deflected by δr. All other particles remain unaltered. The matrix has translational symmetry and is symmetric. The dimensions of the matrix, i.e., the number of eigenvalues is given by the number of particles times the dimensions. The square root of the eigenvalues of the matrix corresponds to the vibrational frequencies of the system. Their distribution function (normalised histogram) provides the **DoS** [21]. Negative eigenvalues or imaginary modes, respectively, correspond to instabilities and indicate that the analysed system has not been driven to its minimum potential. Hence, these modes are a consequence that a stable local equilibrium for all particles has not been reached. Before calculating the matrix coefficients via the analytical derivatives of the known potentials of the soft MD-simulations, one needs to minimise the potential energy such that the local mechanical equilibrium is found. This minimisation is done via the steepest descent method. A similar strategy has been successfully applied to super-lattices of Lennard-Jones potentials [30], [31].

2.3.1 DoS obtained by the velocity autocorrelation function

The velocity auto correlation function (**VAC**) can be connected with the **DoS** [23, 24], [26], [31]. This connection between the **VAC** and **DoS** will be verified in the following calculation. The idea of this calculation is to express all particles' explicit positions $\vec{R}$, i.e., velocities, in a sum of complex modes C_i, real modes A_i, respectively. The Hamiltonian of this system is decomposed in eigenvectors $\vec{E}_\mathrm{i}$ and eigenvalues ω_i. The eigenvectors of the system are orthogonal, $\vec{E}_\mathrm{i}\vec{E}_\mathrm{i} = \delta_\mathrm{ij}$. Hence, the complete system is described by the vector, $\vec{R}(t) = \sum_{\mathrm{i}=1}^{3N} C_\mathrm{i}\vec{E}_\mathrm{i}e^{i\omega_\mathrm{i}t}$, which has $3N$ dimensions. The derivative of this vector, $\dot{\vec{R}}(t)$, defines the system's velocity vector. The product of the velocity vector $\vec{v}(t)$ and $\vec{v}(0)$ yields

$$\vec{v}(t)\vec{v}(0) = \sum_{\mathrm{ij}} \vec{E}_\mathrm{i}\vec{E}_\mathrm{j}\left(A_\mathrm{i}\cos(\omega_\mathrm{i}t) + B_\mathrm{i}\omega_\mathrm{i}t\sin(\omega_\mathrm{i}t)\right)(-A_\mathrm{j}\omega_\mathrm{j}). \tag{2.31}$$

Here, the amplitudes A_i and B_i represent the real and imaginary part. Due to the orthogonality of $\vec{E}_\mathrm{i}\vec{E}_\mathrm{j}$ the sum reduces to

$$\vec{v}(t)\vec{v}(0) = \sum_{\mathrm{i}=1}^{3N}\left(-A_\mathrm{i}^2\omega_\mathrm{i}^2\cos(\omega_\mathrm{i}t) + A_\mathrm{i}B_\mathrm{i}\omega_\mathrm{i}^2 t\sin(\omega_\mathrm{i}t)\right). \tag{2.32}$$

Additionally, we define the **VAC** function $C(t)$ of a single particle's velocity, $\vec{v}_\mathrm{n}$, to

$$NC(t) = N\langle\vec{v}_\mathrm{n}(t)\vec{v}_\mathrm{n}(0)\rangle = \sum_{\mathrm{n}=1}^{N}\vec{v}_\mathrm{n}(t)\vec{v}_\mathrm{n}(0) = \sum_{i=1}^{3N} v_i(t)v_i(0). \tag{2.33}$$

Index i represents all $3N$ velocities of the system. The index n represents the particles. Using eq. (2.32), the single **VAC** function reads

$$C(t) = \frac{1}{N}\sum_{\mathrm{i}=1}^{3N}\left(-A_\mathrm{i}^2\omega_\mathrm{i}^2\cos(\omega_\mathrm{i}t) + A_\mathrm{i}B_\mathrm{i}\omega_\mathrm{i}^2 t\sin(\omega_\mathrm{i}t)\right) \tag{2.34}$$

From this relation we calculate the Fourier transformation

$$\int C(t)\cos(\omega t)\mathrm{d}t = \frac{1}{N}\int\left(\sum_{\mathrm{i}=1}^{3N}\left(-A_\mathrm{i}^2\omega_\mathrm{i}^2\cos(\omega_\mathrm{i}t) + A_\mathrm{i}B_\mathrm{i}\omega_\mathrm{i}^2 t\sin(\omega_\mathrm{i}t)\right)\cos(\omega t)\mathrm{d}t.$$

The first term in this expression, $\cos(\omega_\mathrm{i}t)\cos(\omega t)$ is rewritten into a delta function $\delta(\omega - \omega_i)$. The mixed term $\cos(\omega_\mathrm{i}t)\sin(\omega t)$ is zero, because of symmetry. Hence,

the Fourier transformation of **VAC** yields

$$\int C(t)\cos(\omega t)\mathrm{d}t = \frac{1}{N}\sum_{i=1}^{3N}\frac{A_\mathrm{i}^2\omega_\mathrm{i}^2}{2}\delta(\omega-\omega_\mathrm{i}) \tag{2.35}$$

With the equipartition theorem we assume that the sum of all amplitudes and modes covers systems kinetic energy and equals the systems temperature $\sum_{i=1}^{3N} A_\mathrm{i}^2\omega_\mathrm{i}^2 = \frac{3}{2}Nk_BT$. The **DoS** is observed in the expression of the sum of delta functions. Hence, eq. (2.35) results into

$$D(\omega) = \frac{1}{3Nk_BT}\int C(t)\cos(\omega t)\mathrm{d}t \tag{2.36}$$

that relates the **VAC** with the density of states of a system. This calculation assumed that the system is expressed in a $3N$ dimensional vector containing all spatial positions $\vec{R}(t)$ and velocities $\dot{\vec{R}}(t)$. This vector was rewritten into harmonics that are related to the systems **DoS**. To validate this solution, the Fourier power spectrum of the **VAC** of free harmonic chains has been calculated and compared to the analytical solution of the one-dimensional harmonic chain, cf. appx. 6.2.

2.3.2 Harmonic approximation

The system consists of N particles at spatial position $\vec{r}$ indexed by i, and j, respectively. All these particles are described by a potential $U(\{\vec{r}\})$. The potential depends only on the particle's distance $r_\mathrm{ij} = |\vec{r}_\mathrm{i} - \vec{r}_\mathrm{j}|$, and the potential is expanded around a specific minimum

$$U(\{r_\mathrm{ij}\}) \simeq U(\{0\}) + \sum_{\mathrm{j}=1}^{\mathrm{N}}\left.\frac{\partial U}{\partial r_\mathrm{ij}}\right|_0 r_\mathrm{ij} + \frac{1}{2}\sum_{\mathrm{l}=1}^{\mathrm{N}}\sum_{\mathrm{k}=1}^{\mathrm{N}}\left.\frac{\partial^2 U}{\partial r_{\mathrm{ij\,l}}\partial r_{\mathrm{ij\,k}}}\right|_0 r_{\mathrm{ijl}}r_{\mathrm{ijk}}. \tag{2.37}$$

Particles interact pairwise according to the relative distance $r_\mathrm{ij} = |\vec{r}_\mathrm{i} - \vec{r}_\mathrm{j}|$. The first term is constant and can be neglected. The second term is the force between the particles and is minimised by an instantaneous quench, which will be explained in the subsection 4.8.1. The third term is used as a harmonic approximation of the system. Therefore, it is assumed that the second derivatives for a fixed k and l are constant, $C_\mathrm{kl} = \frac{\partial^2 U}{\partial r_{\mathrm{ij\,l}}\partial r_{\mathrm{ij\,k}}}$. Thus, the force acting on a particle distance r_ij becomes

linear depending on C_{kl}.

$$\frac{\partial U(r_{\mathrm{ij}},k,l)}{\partial r_{\mathrm{ij}}^{\mathrm{l}}} = -F(r_{\mathrm{ij}},k,l) = -C_{\mathrm{kl}} r_{\mathrm{ij}}^{\mathrm{k}} \tag{2.38}$$

This linear coefficients can be calculated by the system's Hamiltonian. In the simplest case the system's Hamiltonian takes the form

$$\mathcal{H}(\{\vec{r}\}) = \sum_{\mathrm{bonds}} \frac{k}{2}(\vec{r}_{\mathrm{i}} - \vec{r}_{\mathrm{j}})^2. \tag{2.39}$$

$\{\vec{r}\}$ represents all spatial positions of the particles in the system. $\vec{r}_{\mathrm{i}}$ and $\vec{r}_{\mathrm{j}}$ represent the spatial position of particles i and j. The sum iterates over all bonds with a harmonic constant k. This Hamiltonian is considered in one-, two-, and three-dimensional case. The systems mainly have been considered to test the eigenvalue solver routines.

One-dimensional harmonic system The simplest case is a one-dimensional system that contains N particles. Every particle in the system has two neighbours $\mathrm{i}-1$ and $\mathrm{i}+1$. The first and last particle are connected to a ring such that the two particles with id $\mathrm{i}=1$ and $\mathrm{i}=N$ are connected. In one dimension, the matrix has size $N \times N$. Matrix $M_{\mathrm{n,m}}$ entries can be distinguished between

- same particle, $M[\mathrm{n}=\mathrm{i};\mathrm{m}=\mathrm{i}] = \sum_{\mathrm{neigh}=1}^{2}(-1)\cdot k = -2\cdot k$
- different particle, but bonded $M[\mathrm{n}=\mathrm{i};\mathrm{m}=\mathrm{j}] = 1\cdot k$
- different particle, not bonded $M[\mathrm{n}=\mathrm{i};\mathrm{m}=\mathrm{j}] = 0$.

The eigenvalues, $\lambda_{\mathrm{i}} = \sqrt{\omega_i}$, give a spectrum that yields the **DoS**, $D(\omega) = \frac{1}{N}\sum \delta(\omega - \omega_{\mathrm{i}})$, of this system. The solution that is observed by this procedure agrees with the solution for the one-dimensional harmonic chain, eq.(2.30). The **DoS** also can be calculated for higher dimensions.

Two-dimensional harmonic system In the two-dimensional system, every particle has four neighbours. Thus, particles form a squared grid and the number of particles in each direction calculates to $\sqrt{N} = N_x = N_x$. Periodic boundaries are applied to each direction. The size of the matrix is $2N$. Its entries $M[n(\mathrm{id},\mathrm{idim}), m(\mathrm{jd},\mathrm{jdim})]$ are characterised by n and m, which are functions of the applied direction idim and a particle's id. The functions m and n are equal but for consistency of the matrix

indices they are distinguished and named differently. The entries of the harmonic matrix are distinguished between

- same particle, $M[n(\mathrm{i},\mathrm{idim});m(\mathrm{i},\mathrm{idim})] = \sum_{\mathrm{neigh}=1}^{4}(-1)\cdot k = -4\cdot k$
- different particle, but bonded $M[n(\mathrm{i},\mathrm{idim});m(\mathrm{j},\mathrm{idim})] = 1\cdot k$
- different particle, not bonded $M[n(\mathrm{i},\mathrm{idim});m(\mathrm{j},\mathrm{idim})] = 0$
- all cross terms between different direction, idim ! = jdim are zero.

Three-dimensional harmonic system Periodic boundaries are applied to x, y, and z direction. The number of particles is N, and they are apportioned in each direction to $\sqrt[3]{N} = N_x = N_y = N_z$ segments. The size of the Hessian matrix is dimension times number of particles, $3N$, and its entries $M[n(\mathrm{id},\mathrm{idim}),m(\mathrm{jd},\mathrm{jdim})]$ are characterised by n and m are functions of the applied direction idim and a particle's id. The matrix entries are distinguished between

- same particle, $M[n(\mathrm{i},\mathrm{idim});m(\mathrm{i},\mathrm{idim})] = \sum_{\mathrm{neigh}=1}^{6}(-1)\cdot k = -6\cdot k$
- different particle, but bonded $M[n(\mathrm{i},\mathrm{idim});m(\mathrm{j},\mathrm{idim})] = 1\cdot k$
- different particle, not bonded $M[n(\mathrm{i},\mathrm{idim});m(\mathrm{j},\mathrm{idim})] = 0$
- all cross terms between different direction, idim ! = jdim are zero.

Each atom/interaction centre has six nearest neighbours connected by a harmonic spring $k = 1$. Figure 2.2 shows the resulting frequency spectra in the case of one, two and three dimensions. The **DoS** of the systems consider: 6144 particles in the one-dimensional, 78x78 particle in the two-dimensional, and 18x18x18 in the three-dimensional case. The size of the matrix is always (dimension)$\times N_{\mathrm{particles}}$. In contrast to a harmonic matrix approximation analytic/numeric calculations, e.g., for a dispersion relation, have also been conducted [21, 32]. There, the equilibrium position is determined by $\vec{x}_{ijk} = \mathrm{i}\cdot a\cdot\hat{e}_{\mathrm{i}} + \mathrm{j}\cdot a\cdot\hat{e}_{\mathrm{j}} + \mathrm{k}\cdot a\cdot\hat{e}_{\mathrm{k}}$. The indices i, j, k determine the three-dimensional localisation within the lattice. The distance between two bonded particles is equally set to a. The maximum number of atoms to each direction $\hat{e}_{\mathrm{i}},\hat{e}_{\mathrm{j}},\hat{e}_{\mathrm{k}}$ is $\sqrt[3]{N}$ so that the total number of particles is N. For a given direction of the wave vector k, one can calculate a dispersion relation, which gives rise to a band structure. In the case of a simple cube one can distinguish between points with a high symmetry: Γ is related to the centre of the Brillouin

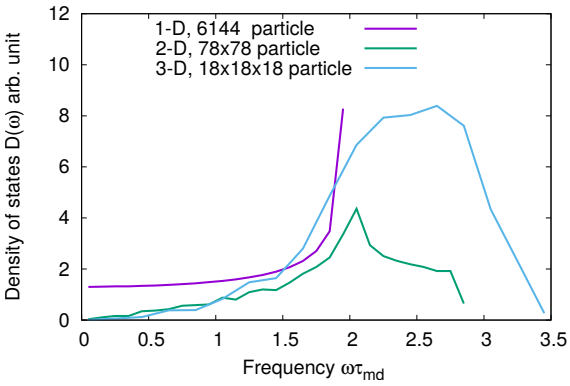

Figure 2.2 DoS for (i) linear one-dimensional harmonic chain (ii) two-dimensional lattice with 4 harmonic bonded nearest neighbours (iii) three-dimensional lattice with 6 harmonic bonded nearest neighbours. Frequencies of the **DoS** are calculated by the square root of eigenvalues $\omega = \sqrt{\lambda_{\mathrm{i}}}$ of the harmonic matrix $M_{\mathrm{n}\times m}$. **DoS** is a histogram of all these frequencies. The one dimensional solution fits to the calculated one of the harmonic chain, cf. fig.2.1.

zone, M represents the centre of an edge, R represents the corner, and X represents the centre of a face. The band structure enables us to calculate a **DoS**, too.

Three-dimensional random harmonic fluid For solids, there are approaches to relate the vibrational spectra to a random sparse matrix [33]. For polymers, the approach they presented could be adopted. Harmonic potentials have the advantage that their second derivatives can be related to a constant that is structurally independent of the underlying coordinates. Hence, an approach to relate a fluid with a random sparse matrix without quenching procedure might be possible. The sum of each row is zero and the main diagonal entry takes the number of harmonic interactions. The number of interactions could be derived systematically, e.g., by a pair correlation function. This number of interactions defines the occupation density of the matrix entries.

2.4 Phonons at interfaces and the density of states

We have introduced some analytical models for the **DoS** and calculated, i.e., the specific heat capacity of a material and thereby its thermal properties. Assuming that the transport properties and specific heat capacity of a material are given by phonon properties, especially the influence of interfaces emerged as a specific interest. In general phonons can be found coherent or incoherent. This behaviour can be motivated by the decay rate of a propagating wave. If the decay rate is fast, there is a high damping in the system and the phonon propagation has a diffusive character. Vice versa, if the decay is slow, propagating modes can be observed in the spirit of acoustic waves. For each of these limits, there exists a main model: the

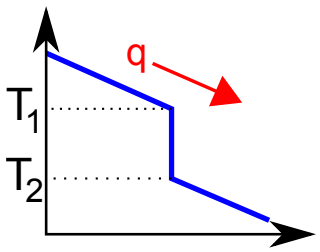

Figure 2.3 In the presence of an energy current, $\dot{q}$, an interfacial resistance, $R_{\text{interface}} = \frac{\Delta T}{\dot{q}}$, gives rise to a temperature jump, $\Delta T = T_1 - T_2$.

acoustic mismatch model (AMM) [34] and the diffuse mismatch model (DMM) [35]. These two models behave fundamentally different, especially at interfaces. On the one hand, there is a reflection of phonons, which is similar to optics, at the interface (AMM). On the other hand, there is an elastic diffusive scattering at the interface [36] (DMM). These two models analytically predict the transport characteristic across an interface or a thermal boundary resistance

$$R_{\text{interface}} = \frac{\Delta T}{\dot{q}}. \tag{2.40}$$

Thermal resistance is defined by a sudden temperature change, $T_1 - T_2 = \Delta T$, across the interface. $\dot{q}$ is the thermal current (per unit area) across the interface. The influence of interfaces on thermal transport properties was found by Kapitza, who performed experiments with liquid helium in 1941 [3]. In the next section the main steps of the derivation of the **AMM** and **DMM** model are presented in order to connect these models with resistances at interfaces observed by simulations. Figure 2.4 summarises the main assumption

2.4.1 Acoustic mismatch model (AMM)

The acoustic mismatch model was introduced by Khalatnikov in 1952 [34]. The model predicts a transmission coefficient α, which is the ratio of transmitted and incident energy [5]. Historically, this model has been developed to be applied for low temperature systems [37], because, for these systems, the interface appears smooth, and perfect that modes can vibrate longitudinally, parallel-transversally and perpendicular- transversally. The **AMM** is an analogue to the Fresnel equations, the transmission and reflection of light that occurs moving from one medium into another medium. These transmission coefficients α_{i} can be influenced by phonon mode, wave vector, frequency, and temperature. These influences are limited in the **AMM** model, because the materials are isotropic, the transmission coefficient

[5] here, α follows the common notation and will be a transmission probability of phonons

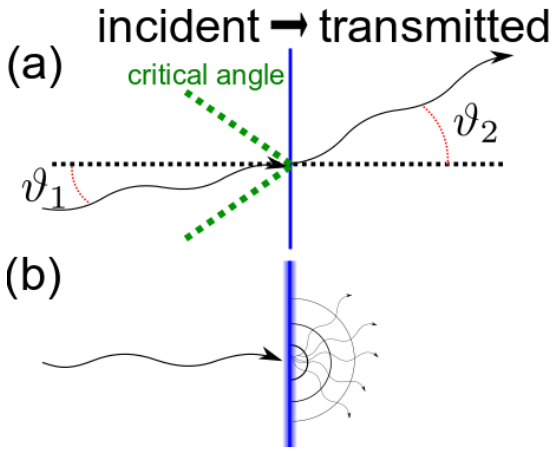

Figure 2.4 (a) an incident wave is reflected or transmitted at the interface, acoustic impedance of material controls the outgoing angle, i.e., similar to optics (b) an incident wave is scattered diffusive, i.e., loses memory.

is independent of the temperature, and non-harmonic interactions are neglected [35, 36, 38]. Incident waves are travelling at the same speed in all directions [36]. The speed of the phonons, c_1, in material 1 is

$$c_1 = \frac{1}{\sqrt{\sum_{\mathrm{j}} c_{\mathrm{j}}^{-2}}}. \tag{2.41}$$

Here, j represents the summation over transversal (T) and longitudinal (L) waves, i.e., c_{j} takes two values for speed of sound c_{T} and c_{L}. In principle, one can add an additional index according to the material property, which dictates the characteristics of incident phonons. The transmission probability coefficient between two materials, 1 and 2, calculates to [36, 37],

$$\alpha_{1\to 2} = \frac{\frac{4\rho_2 c_2}{\rho_1 c_1}\frac{\cos(\theta_2)}{\cos(\theta_1)}}{\left(\frac{\rho_2 c_2}{\rho_1 c_1} + \frac{\cos(\theta_2)}{\cos(\theta_1)}\right)}. \tag{2.42}$$

ρ_1 is the material one's density, θ_1 is the incident angle to the normal of the interface, fig. 2.4. The product of the density and speed of sound is the characteristic specific acoustic impedance z. The model will give the total heat q transferred from first to second material across unit interface. Therefore, the angle dependence ϑ of the transmission probability α is integrated out, which yields the integrated transmission coefficient

$$\Gamma_{1\to 2} = \int_0^{\theta_c} \alpha_{1\to 2} \sin\theta \cos\theta \mathrm{d}\theta. \tag{2.43}$$

θ_c is the critical angle given by Snell's law, $\theta_c = \arcsin(c_1/c_2)$. Here, $\Gamma_{1\to2}$ typically is a numerical value that depends on the system, which is considered [35]. Finally, the flux across the interface q, eq. (2.40), is formulated. This flux is given by the difference of the total heat Q transferred from $1 \to 2$ and $2 \to 1$ per unit area. q results in [35, 36]

$$q_{\mathrm{AMM}} = \frac{k_{\mathrm{B}}^4 \pi^2}{60\hbar^3} \left((T_1^4 - T_2^4) \frac{\Gamma_{1\to2}}{c_1^2} \right). \tag{2.44}$$

Here, c_1 is the speed of the phonons in material 1, eq. (2.41). The flux q_{AMM} across the interface has been calculated by a forward flux, $Q_{1\to2}$, and a backward one , $Q_{1\to2}$ [6]. In the calculation for $Q_{1\to2}$, an isotropic Debye fluid has been assumed. Therefore, the Bose-Einstein statistics and the density of states of the Debye model, sec. 2.2.2, have been used [35]. Finally, inserting eq. (2.44) into eq. (2.40), the thermal resistance of **AMM** results into

$$\begin{aligned} R_{\mathrm{interface}}^{\mathrm{AMM}} &= \frac{\Delta T}{q_{\mathrm{AMM}}} = \left(\frac{Q_{1\to2} - Q_{2\to1}}{A} \right)^{-1} \Delta T \\ &= \frac{(T_1 - T_2)}{\left(\frac{k_{\mathrm{B}}^4 \pi^2 (T_1^4 - T_2^4)}{60\hbar^3 c_1^2} \cdot \Gamma_{1\to2} \right)} = \left(\frac{k_{\mathrm{B}}^4 \pi^2 (T_1^2 + T_2^2)(T_1 + T_2)}{15\hbar^3 c_1^2} \cdot \Gamma_{1\to2} \right)^{-1}. \end{aligned} \tag{2.45}$$

The flux was divided by surface area A, because the flux q_{AMM} is expressed per unit area. The resistance $R_{\mathrm{interface}}^{\mathrm{AMM}}$, eq. (2.45), still depends on the temperature difference of the two media. Therefore, we consider the limit that the difference, ΔT, goes to zero eq. (2.45) that yields

$$\lim_{\Delta T \to 0} R_{\mathrm{interface}}^{\mathrm{AMM}} = \left(T_2^3 \frac{k_{\mathrm{B}}^4 \pi^2}{15\hbar^3 c_1^2} \cdot \Gamma_{1\to2} \right)^{-1}. \tag{2.46}$$

For a given non-analytical form of a **DoS**, one performs a numerical integration of $Q_{1\to2}$ and $Q_{2\to1}$ [39, 40].

[6] The complete integration has been expressed by $Q_{1\to2} = \frac{1}{2} \sum_{\mathrm{j}} \Gamma_{1\to2} \int_0^{\omega_D} \left(\frac{\mathrm{d}D_{1\to2}^{\mathrm{Debye}}(\omega,T)}{\mathrm{d}T} \hbar\omega \right) \mathrm{d}\omega$. Here, ω_D is the Debye frequency on the incident side 1 and $\mathrm{d}D_{1\to2}^{\mathrm{Debye}}(\omega,T) = \frac{\omega^2 \mathrm{d}w}{2\pi c_{1\to2} \cdot (\exp(\hbar\omega/k_{\mathrm{B}}T) - 1)}$ represents the Debye-**DoF**s with Bose Einstein statistics [35, 36].

2.4.2 Diffusive mismatch model (DMM)

The diffusive mismatch model (**DMM**) was first introduced by Swartz and Pohl in 1989, and it is a high-temperature model. The main difference between the **AMM** and **DMM** is the calculation of the transmission probability: (i) it fulfils detailed balance (ii) the interface causes a diffusive scattering [35]. Hence, a phonon looses the memory of where it came from, what mode it had and all correlations between incoming and outgoing phonons are ignored [35]. With this approximation, the transmission coefficient is

$$\alpha_{\mathrm{i}\to 3-\mathrm{i}}(\omega) = \frac{\sum_{\mathrm{j}} c_{3-\mathrm{i,j}}^{-2}}{\sum_{\mathrm{j}} c_{\mathrm{i,j}}^{-2}}.$$

i is the kind of material respectively or side of the incident phonon, i.e., for $(i = 1) \to (3 - (i = 1)) \Rightarrow 1 \to 2$ and $(i = 2) \to (3 - (i = 2)) \Rightarrow 2 \to 1$. The notation $\mathrm{i} - 3$ results from the detailed balance and denotes the side opposite to side i. The summation over j represents the transverse (T) or longitudinal (L) parts, i.e., speed-of-sound transverse, c_T, and speed-of -sound longitudinal, c_L. Again, the phonon velocities and phonon densities were assumed by the Debye-model, for a detailed derivation of eq. (2.47) cf. [35]. In a diffusive approach, angle dependency does not exist and the calculation of the flux, Γ, eq. (2.43), can be done straightforward. This can be used to calculate the complete flux across the interface:

$$q_{\mathrm{DMM}} = \frac{k_{\mathrm{B}}^4 \pi^2}{\hbar^3 120} \left(T_1^4 \sum_{\mathrm{j}} c_{1,\mathrm{j}}^{-2} \alpha_{1\to 2} - T_2^4 \sum_{\mathrm{j}} c_{2,\mathrm{j}}^{-2} \alpha_{2\to 1} \right). \tag{2.47}$$

This equation can be used to calculate the thermal boundary resistance, $R_{\mathrm{interface}}^{\mathrm{DMM}}$. In the limit that the difference of temperatures goes to zero the resistance at the interface is given by

$$\lim_{\Delta T\to 0} R_{\mathrm{interface}}^{\mathrm{DMM}} = \left(\frac{k_{\mathrm{B}}^4 \pi^2}{\hbar^3 30} \left(\sum_{\mathrm{j}} c_{1,\mathrm{j}}^{-2} \right) \alpha_{1\to 2} T_2^3 \right)^{-1}. \tag{2.48}$$

In principle, **AMM** is a low-temperature model and **DMM** a high-temperature model. Beyond the two described models, there are approaches that use a real density of states (**DoS**) instead of the Debye model's **DoS**. Hence, they include a real **DoS** (or exact phonon-dispersion, specific heat etc.), which improves the accuracy of thermal resistance's theoretical prediction [36, 39, 40].

3 Simulation techniques

In this chapter, existing and new techniques to perform simulations on the mesoscale are presented. On this level of coarsening, effects between the atomistic and macroscopic scale are in the focus. To better delineate the scales, a rough distinction regarding the magnitude of length and time scale, as well as the number of particles, is given. On the atomistic or rather quantum mechanical level, the typical length scale is $l \approx 0.5$ nm, the time scale is $\Delta t = 10^{-17} s$, and problems that can be exactly solved, are limited by a countable number, e.g., H, H_2^+, He. Density functional theory numerically gives access to a system containing 10^3 particles. The dynamics of the system is given by the Schrödinger equation and corresponding Hamiltonian mechanics. The macroscopic level has a typical length scale of $l \gtrsim 10$ μm. The time scale is on the order of seconds. If these systems are described by continuum model descriptions, e.g., Navier-Stokes equations, these continuum models capture the collective behaviour of 10^{23} particles and more. Hence, even if the underlying fluid is quite complex one can define new dimensionless characteristics such as the Reynolds number, which is the ratio between inertia and viscous forces, that describe the macroscopic properties. The mesoscopic scale enters inbetween these two scales. Hence, the particle number is much larger than one and the dynamics of the system can be captured by the thermal diffusion equation. The challenge on the mesoscale consists of including the relevant interactions in a minimal set of interactions to describe macroscopic observables. This can be implemented by a top-down or bottom-up approach. In this thesis, a coarse-grained model that captures the relevant interactions required to bring about the universal aspects of soft matter phenomena including energy transport is developed. This accounts for an investigating of thermal effects on a universal coarse-grained scale also allows us to mimic systems on large time scales.

In this chapter, the new energy-conserving Monte-Carlo scheme (**eMC**) is introduced. This scheme generates the microcanonical ensemble of particle coordinates, momenta, and internal energies. Moreover, the system conserves energy and mo-

menta locally according to the microcanonical ensemble. This method can be understood as an improvement of the existing energy-conserving dissipation particle dynamics **eDPD**, because using a Monte-Carlo scheme prevents the problem of discretisation errors of a first-order integration scheme. Hence, to create a numerically stable integration scheme of **eDPD**, one has to put significant effort into the stochastic part of the Wiener Process. A Wiener process is a continuous-time stochastic process, which has normal distributed independent increments. The derivation of **eMC** also clarifies the connection to microcanonical partition function: It is distinguished between model characteristics that are necessary to represent the microcanonical ensemble and model properties that are chosen in order to mimic a physically realistic dynamics.

A logical consequence, which increases the stability of **eDPD**, is to reduce the integration step, hence typical integration time-steps of **eDPD** are in the order of $\delta t = 0.00002$ [41],[42]. This fact makes it computationally difficult to reach the large length and time scales of collective phenomena in soft matter by eDPD. Also, it is difficult to adapt the given equations of motion to more complex structures, i.e., how does friction and noise depends on different particle types. Nevertheless, **eDPD** has been established as a standard tool to investigate thermal transport properties. To clarify the scope of **eMC** some typical topics **eDPD** is used for are mentioned. Early work in the late nineties are shaped by work of Avalos, Mackie, and Ripoll who worked out the practical benefits and give basic assumptions and calculations to perform and verify **eDPD** simulations. At this time their focus was on heat-flow and specific heat capacities [43–45]. As soon as **eDPD** became popular, simulation studies have addressed: shock-waves, e.g., propagating shock and detonation waves [46], shock-wave induced damage in lipid bilayers [47], shock-to-detonation transition in a reactive **eDPD** liquid [48], thermo-mechanical processes [49], modelling mesoscopic solidification using dissipative particle dynamics [50], and convection in liquids [41]. However, all of these applications would directly benefit from **eMC** cf. sec. 3.3.

To account the **eMC** scheme to a broad ground, the key aspects of dissipative particle dynamics (**DPD**) are revised, energy-conserving particle dynamics **eDPD**, respectively. The new **eMC** scheme bases on a general decomposition of microcanonical partition function, and uses the underlying physical process, e.g., thermal relaxation of internal **DoF**s to propose a new configuration, which is accepted by the Metropolis rate [51]. The Monte-Carlo scheme can be understood as an integration scheme of infinite-order, which always guarantees that the equilibrium distribution

corresponds to the microcanonical ensemble.

3.1 Dissipative particle dynamics with energy conversion

The method of dissipative particle dynamics **DPD** was first developed by Hoogerbrugge et al. [52]. They claimed that a classic **MD** simulation takes too many details into account, which in principle are not necessary to observe the physically correct hydrodynamic behaviour of a fluid. Therefore, they introduced a fluid particle, representing molecules, which had been lumped together to an effective particle. Based on these particles they constructed a model to describe the universal characteristics of a fluid by a coarse-grained model with a minimal set of parameters. This model relies on two main requirements: (i) local momentum conservation to obtain hydrodynamic behaviour and (ii) a repulsive interaction, which limits density fluctuations. All other characteristics of the fluid are captured by friction and noise. Hence, a coarse-grained "fluid particle" is affected by three forces (i) a conservative force, which is freedom of choice but in common soft repulsive, (ii) a dissipative force, which reduces particle's kinetic energy proportional to the velocity, (iii) a random force, which drives Brownian dynamics via fluctuations. Hence, the force that acts on a particle i is the sum of pairwise interactions of particle i and j

$$\vec{F}_{\mathrm{i}} = \sum_{\mathrm{i}\neq\mathrm{j}} \left(\vec{F}^{\mathrm{C}}_{\mathrm{ij}} + \vec{F}^{\mathrm{D}}_{\mathrm{ij}} + \vec{F}^{\mathrm{R}}_{\mathrm{ij}} \right), \tag{3.1}$$

which consist of the conservative (C), dissipative (D), and random part (R). The dissipative and random forces take the form

$$\vec{F}^{\mathrm{D}} = -\gamma \omega_{\mathrm{D}}(\vec{r}_{\mathrm{ij}})(\vec{e}_{\mathrm{ij}}\vec{v}_{\mathrm{ij}})\vec{e}_{\mathrm{ij}}, \tag{3.2}$$

$$\vec{F}^{\mathrm{R}} = \sigma \omega_{\mathrm{R}}(\vec{r}_{\mathrm{ij}})\vec{e}_{\mathrm{ij}}\xi_{\mathrm{ij}}. \tag{3.3}$$

$\vec{r}_{\mathrm{ij}} = \vec{r}_{\mathrm{i}} - \vec{r}_{\mathrm{j}}$ denotes the distance vector between particles i and j. Hence, $\vec{e}_{\mathrm{ij}}$ represents the unit vector from the i-th to th j-th particle [53]. $\vec{v}_{\mathrm{ij}} = \vec{v}_{\mathrm{i}} - \vec{v}_{\mathrm{j}}$ is the velocity vector between particles i and j. This expression uses the modified form of Espanol, who substantiated Hogerbrugge's idea to a theoretical framework of stochastic differential equations **SDE**. They showed that the form of the dissipative and random forces has to be chosen such that they recover the Gibbs distribution recovered as the stationary

solution to the Fokker-Planck equation [53]. The random force is controlled by ξ_{i}, which mimics Gaussian white noise. The mean value of ξ_{i} is equal to zero and two time-steps t_1 and t_2 are independent without any history. The variance of the two random variables ξ controlling the random force between particle i and j at time t_1 and t_2 is linear in the time increment $\mathrm{d}t$. Hence, two sequenced time-steps t_1 and t_2 can be described by $\langle \xi_{\mathrm{i}_1\mathrm{j}_1}(t_1)\xi_{\mathrm{i}_2\mathrm{j}_2}(t_2)\rangle = (\delta_{\mathrm{i}_1\mathrm{i}_2}\delta_{\mathrm{j}_1\mathrm{j}_2} + \delta_{\mathrm{i}_1\mathrm{j}_2}\delta_{\mathrm{j}_1\mathrm{i}_2})\delta(t_1 - t_2)$ [53]. To control the range of dissipative and random force weighting functions ω_{D} and ω_{R} are introduced [1]. Espanol demonstrated that the steady-state solution of the Fokker-Planck equations yields the Gibbs distribution by selecting of $\omega_{\mathrm{R}}^2(r) = \omega_D(r)$ and $\sigma^2 = 2\gamma k_{\mathrm{B}}T$. For ω_{R}, one uses the function $2(1 - r/r_c)$, which is also consistent with Hoogerbrugge [52]. In summary, the stochastic equations of motion of dissipative particle dynamics are

$$\mathrm{d}\vec{r}_{\mathrm{i}} = \frac{\vec{p}_{\mathrm{i}}}{m_{\mathrm{i}}}\mathrm{d}t, \tag{3.4}$$

$$\mathrm{d}\vec{p}_{\mathrm{i}} = \left(\sum_{\mathrm{i}\neq\mathrm{j}} \vec{F}_{\mathrm{ij}}^{C}(r_{\mathrm{ij}}) - \sum_{\mathrm{i}\neq\mathrm{j}} \gamma\omega_{\mathrm{D}}(r_{\mathrm{ij}})\left(\vec{e}_{\mathrm{ij}}\cdot\vec{v}_{\mathrm{ij}}\right)\vec{e}_{\mathrm{ij}}\right)\mathrm{d}t + \sum_{\mathrm{i}\neq\mathrm{j}} \sqrt{2k_{\mathrm{B}}T\gamma\omega_{\mathrm{D}}(r_{\mathrm{ij}})}\vec{e}_{\mathrm{ij}}\mathrm{d}W_{\mathrm{ij}}. \tag{3.5}$$

Here, the random variable ξ_{ij}, which controls the random force between two particles, is replaced by an increment, $\mathrm{d}W_{\mathrm{ij}} = \mathrm{d}W_{\mathrm{ji}}$, of the Wiener process. In this process the mean value of increments is zero and their variance is linear in the time increment $\mathrm{d}t$. The increments themselves are uncorrelated, i.e., a new increment is totally independent and does not know anything about the increment before.

The **DPD** method cannot recover a system's real specific heat capacity, because most of the vibrational modes, which store specific heat, have been integrated out. Sequentially, Avalos and Espanol expanded **DPD** and introduced an additional degree of freedom (**DoF**) to each particle, internal energy e [9, 10]. This **DoF** is described by an internal entropy $s(e)$. Therefore, they expanded the stochastic equations of motion (3.4) and (3.5) formulated an equation of motion for the additional **DoF** - the internal energy e. This additional equation for the internal energy considers two parts: (i) a thermal relaxation to address viscous heating, (ii) a mechanical energy part. The mechanical energy part which is added to the internal **DoF**, e, is the reversed part of energy which is dissipated in the velocities.

[1] Here, the weighting function ω_{D} has nothing to do with Debye frequency, which was introduced in the previous chapter.

Hence, the total sum of mechanical energy that is potential and kinetic energy, and internal energy is conserved in **eDPD**. Thus, the **eDPD** equations take the form

$$\mathrm{d}\vec{r}_\mathrm{i} = \frac{\vec{p}_\mathrm{i}}{m_\mathrm{i}}\,\mathrm{d}t, \tag{3.6}$$

$$\mathrm{d}\vec{p}_\mathrm{i} = \left(\sum_{\mathrm{i}\neq\mathrm{j}} \vec{F}^C_{\mathrm{ij}}(r_\mathrm{ij}) - \sum_{\mathrm{i}\neq\mathrm{j}} \gamma\omega_\mathrm{D}(r_\mathrm{ij})\,(\vec{e}_\mathrm{ij}\cdot\vec{v}_\mathrm{ij})\,\vec{e}_\mathrm{ij}\right)\mathrm{d}t + \\ + \sum_{\mathrm{i}\neq\mathrm{j}} \sqrt{2k_\mathrm{B}T_\mathrm{loc}\gamma\omega_\mathrm{D}(r_\mathrm{ij})}\vec{e}_\mathrm{ij}\mathrm{d}W^\nu_\mathrm{ij}, \tag{3.7}$$

$$\mathrm{d}e_\mathrm{i} = \frac{m}{2}\left[\sum_\mathrm{j}\left(\omega_\mathrm{D}(r_\mathrm{ij})\gamma_\mathrm{ij}(\vec{v}_\mathrm{ij}\vec{e}_\mathrm{ij})^2 - 2k_\mathrm{B}T_\mathrm{loc}\gamma_\mathrm{ij}\omega^2_\mathrm{R}(r_\mathrm{ij})\right)\mathrm{d}t - \right. \\ \left. - \sum_\mathrm{j}\sqrt{2k_\mathrm{B}T_\mathrm{loc}\gamma_\mathrm{ij}}\omega_\mathrm{R}(r_\mathrm{ij})(\vec{v}_\mathrm{ij}\vec{e}_\mathrm{ij})\mathrm{d}W^\nu_\mathrm{ij}\right] + \\ + \sum_\mathrm{j}\kappa_\mathrm{ij}\left(\frac{1}{T_\mathrm{i}} - \frac{1}{T_\mathrm{j}}\right)\omega^e_\mathrm{D}(r_\mathrm{ij}) + \sum_\mathrm{j}\alpha_\mathrm{ij}\omega^e_\mathrm{R}(r_\mathrm{ij})\mathrm{d}W^e_\mathrm{ij}. \tag{3.8}$$

Here, κ_ij is the intrinsic thermal heat conductivity between two particles. The inverse temperatures $1/T_\mathrm{i}$, $1/T_\mathrm{j}$, are related to the derivative of internal entropy with respect to internal energy. Instead of a thermodynamic temperature T, a local temperature T_loc is used, which is obtained by the local internal temperature of a particle. The relation $(\omega(r)^e_\mathrm{R}(r))^2 = \omega(r)^e_\mathrm{D}(r)$ provides the range of forces as $\omega_\mathrm{D} = \omega^2_\mathrm{R}$. The first term of eq. (3.8) quantifies the mechanical energy, which is dissipated by velocity, i.e., momentum, eq. (3.7) to conserve total energy. The second part is related to the thermal relaxation. With the expression $\mathrm{d}W^e_\mathrm{ij}$, they introduced an additional Wiener Process that is symmetric, such that the random energy that is added to particle i's energy, is subtracted from particles j's one. Espanol and Mackie postulated that there is no correlation between the time differentials $\mathrm{d}W^e_\mathrm{ij}$ and $\mathrm{d}W^\nu_\mathrm{ij}$ [9, 10]. To solve these equations of motion (3.6), (3.7), and (3.8), one has to perform a first-order integration scheme. This is accompanied by a discretisation, which leads to serious discretisation errors. Even if **eDPD** was successfully applied to various problems and research fields, problems would remain inaccessible, because of an inefficient numerically unstable implementation, which is influenced by the two stochastic parts of energy fluctuation in the internal degrees of freedom controlled by $\mathrm{d}W^e_\mathrm{ij}$ and dissipative part in velocities controlled by $\mathrm{d}W^\nu_\mathrm{ij}$. Therefore, it remains the question of how to solve the stochastic equations exactly [54]. Eventually, this question can be solved by the energy-conserving Monte-Carlo scheme **eMC**, which

can be understood in terms of a thermostat coupling internal and external degrees of freedom via parallel momenta. Next, two common thermostats are introduced to ease the understanding of how **eMC** acts.

3.2 Excursion: thermostats

A thermostat couples particles in a NVE ensemble to a heat bath, which results in the ensemble NVT. In this section two thermostats are introduced, because the **eMC** scheme facilitates the understanding in terms of a thermostat. The two thermostats are the Lowe-Andersen and the Peters thermostat.

3.2.1 Lowe-Andersen thermostat

DPD can be conceived as a thermostat that locally conserves momentum. An alternative approach to dissipative particle dynamics is a thermostat, e.g., Lowe-Andersen thermostat [55]. This thermostat solves the time-step problem of **DPD** because one can apply an integration scheme to microcanonical **DoF**s, and apply a thermostat that does a thermalisation that does not involve a time-step. The update procedure of the thermostat acts on particle pairs, which interact via non-bounded forces. The update of two interacting particles is controlled by a collision rate $\Gamma \cdot \Delta t$. If a uniform random number ξ_c between [0,1] is smaller than the collision rate, the relative velocity in the parallel direction of the particle pair is updated. The update of momenta is

$$\vec{p}_{\text{new i}} = \vec{p}_{\text{old i}} + \mu_{\text{ij}} \left(\xi_r \sqrt{k_{\text{B}} T / \mu_{\text{ij}}} - (\vec{v}_{\text{i}} - \vec{v}_{\text{j}}) \vec{e}_{\text{ij}} \right) \vec{e}_{\text{ij}}, \tag{3.9}$$

$$\vec{p}_{\text{new j}} = \vec{p}_{\text{old j}} - \mu_{\text{ij}} \left(\xi_r \sqrt{k_{\text{B}} T / \mu_{\text{ij}}} - (\vec{v}_{\text{i}} - \vec{v}_{\text{j}}) \vec{e}_{\text{ij}} \right) \vec{e}_{\text{ij}}. \tag{3.10}$$

μ_{ij} represents the reduced mass $\frac{m_{\text{i}} m_{\text{i}}}{m_{\text{i}} + m_{\text{j}}}$. The unit vector $\vec{e}_{\text{ij}}$ corresponds to the direction of the connection of particles i and j such that $\vec{e}_{\text{ij}} = \frac{(\vec{r}_i - \vec{r}_j)}{|(\vec{r}_i - \vec{r}_j)|}$. ξ_r is a random number drawn from a Gaussian distribution with unit variance. This thermostat is similar to the **eMC** method, because it decouples pairs of particles into two statistically independent parts: the velocity of the centre of mass and a relative velocity. The Lowe-Andersen thermostat allows controlling the friction and noise by the collision rate Γ. A collision goes along with a change of the velocity. Calculating a velocity autocorrelation function will show that vibrational modes are destroyed by this.

3.2.2 Peters thermostat

Drawing completely new, uncorrelated relative momenta according to eq. (3.10) significantly perturbs the trajectories (in comparison to the microcanonical scheme, Newton's equation of motion) [56]. Therefore, Peters came up with an improved generalised scheme of the Lowe-Andersen thermostat. The main idea is to perform a partial re-equilibration of the relative velocity. This partial re-equilibration of the momenta,

$$\vec{p}_{\text{new i}} = \vec{p}_{\text{old i}} + \mu_{\text{ij}} \left(-\alpha(\vec{v}_{\text{ij}} \cdot \vec{e}_{\text{ij}}) + \sqrt{2\alpha - \alpha^2}\vec{v}_{\text{ij}}^{EQ} \right) \vec{e}_{\text{ij}}, \tag{3.11}$$

$$\vec{p}_{\text{new j}} = \vec{p}_{\text{old j}} - \mu_{\text{ij}} \left(-\alpha(\vec{v}_{\text{ij}} \cdot \vec{e}_{\text{ij}}) + \sqrt{2\alpha - \alpha^2}\vec{v}_{\text{ij}}^{EQ} \right) \vec{e}_{\text{ij}}, \tag{3.12}$$

can be controlled by the parameter $0 < \alpha < 1$. For $\alpha = 1$, the scheme falls back to update scheme of Lowe-Andersen, eq. (3.10). The velocity v_{ij}^{EQ} is drawn from a normal distribution with variance $k_{\text{B}}T/\mu_{\text{ij}}$. The only difference between the Peters and Lowe-Andersen thermostat is given by the partial re-equilibration of the relative velocity

$$v_{\text{new ij}} = (1 - \alpha)v_{\text{ij}} + \sqrt{2\alpha - \alpha^2} \cdot v_{\text{ij}}^{EQ}. \tag{3.13}$$

The old and new relative velocities $v_{\text{ij new}}$ satisfy a Maxwell-Boltzmann distribution, because sum of independent Gaussian variables will also satisfy a Gaussian distribution [56]. One advantage of the Peters thermostat is that optical and acoustic phonon vibrations can propagate through the system and are not disturbed by the thermostat. Peters thermostat allows to control the correlations in a more gentle way by introducing the re-equilibration constant α. Especially, identification of the **DoF**s of system through a Fourier transformation of the velocity autocorrelation function is an advantage. Even if the partial change of the velocities keeps correlations, when the **DoS**s are calculated, the thermostats are switched off.

3.3 Energy Monte-Carlo scheme

In the previous section, **eDPD** has been introduced. We conclude that the first-order integration scheme for the stochastic differential equations of motion (**SDE**) inhibits an implementation that is fast and numerically stable. Even if there are thermostats for **DPD** models, e.g., Peters thermostat there is not any known strategy to expand

these approach to the additional **DoF** used in **eDPD**. **eMC** strategy overcomes this limitation of **SDE** and previous methods by combining microcanonical molecular-dynamics (**MD**) simulations, soft repulsive non-bonded potential and Gaussian bonds, with a force biased Monte-Carlo scheme that couples the internal **DoS**s to the outer ones and acts similar to the strategy of a thermostat, e.g., Lowe-Andersen (cf. sec. 3.2.1) or Peters (cf. sec. 3.2.2) [54–57]. Our **eMC** scheme guarantees that the equilibrium distribution corresponds to the microcanonical ensemble by infinite order.

In the next section, the new **eMC** scheme is deduced. We explain the microcanonical partition function and systematically derive the acceptance criterion, which samples this microcanonical partition function, and give an explanation how to address the internal **DoF**s. The **eMC** scheme (i) generates the microcanonical ensemble of particle coordinates and momenta, and internal energies, and (ii) mimics a realistic dynamics [11].

3.3.1 Microcanonical partition function

The **eMC** scheme utilizes a coarse-grained description on a microcanonical level. In order to map thermal properties, e.g., specific heat capacity, **DoF**s, which have been integrated out, have to be taken into account. These **DoF**s are specified by translation, rotation, vibration, etc., but time and length scale of these **DoF**s are independent of the scale **eMC** addresses, i.e., vibrational frequencies are located in the tera-hertz regime and their contribution to the universal energy transport phenomena is limited. Hence, several atoms along the molecular backbone are lumped into an effective, coarse-grained interaction centre and an additional internal **DoF** e, which represents all the **DoF**s $\{q\}$, which have been integrated out, fig. 3.1. Hence, the **eMC** scheme will distinguish external and internal **DoF**s. The internal **DoF** - internal energy, e, - is related to an internal entropy

$$s(e_\mathrm{i}) = k_\mathrm{B} \ln \left(\int \mathrm{d}\{q_\mathrm{i}\} \delta[e_\mathrm{i}(\{q_\mathrm{i}\}) - e] \right) . \tag{3.14}$$

This entropy quantifies the number of states a coarse-grained interaction centre has at a specific energy e. Here, i represents a coarse-grained particle's index. The **eMC** scheme samples a microcanonical partition function, which relies on the assumption that there is no coupling between the internal **DoF**s $\{q\}$ and the external **DoF**s (coarse-grained particles' momenta and spatial positions). Hence, the system's total

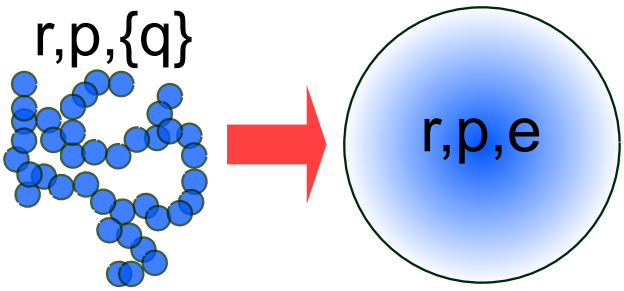

Figure 3.1 Several atoms along the molecular backbone are lumped into an effective, coarse-grained interaction centre. **DoF**s $\{q\}$, which have been integrated out, are captured by one collective **DoF**, which is the internal energy, e.

sum of the energy is given by two independent parts (i) the Hamiltonian of all external **DoF**s, $\mathcal{H}(\{r\},\{p\}) = \sum_{\mathrm{i}} \frac{\vec{p}_{\mathrm{i}}^2}{2m_{\mathrm{i}}} + \sum_{\mathrm{i}<\mathrm{j}} V(\vec{r}_{\mathrm{i}} - \vec{r}_{\mathrm{j}})$, (ii) the sum of all particles' internal energy $e_{\mathrm{i}}(\{q_{\mathrm{i}}\})$. The partition function reads

$$\mathcal{Z}_{\mathrm{mc}} = \int \prod_{\mathrm{i}} \frac{\mathrm{d}\vec{r}_{\mathrm{i}}\mathrm{d}\vec{p}_{\mathrm{i}}}{(2\pi\hbar)^{3nN} n!} \mathrm{d}\{q_{\mathrm{i}}\} \times \\ \times \delta\left(\sum_{\mathrm{i}} \frac{\vec{p}_{\mathrm{i}}^2}{2m_{\mathrm{i}}} + \sum_{\mathrm{i}<\mathrm{j}} V(\vec{r}_{\mathrm{i}} - \vec{r}_{\mathrm{j}}) + e_{\mathrm{i}}(\{q_{\mathrm{i}}\}) - \mathbf{E}_{\mathrm{total}} \right). \tag{3.15}$$

Here, i represents a summation over all particles. n is the number of polymers, N is the number of segments. $\vec{p}_{\mathrm{i}}$ corresponds to the momenta and $V(\vec{r}_{\mathrm{i}} - \vec{r}_{\mathrm{i}})$ denotes a pair potential, which depends on the distance vector between two particles. **DoF**s $\{q_i\}$ are integrated out via the entropy relation, eq. (3.14). The microcanonical partition function is integrated over $\mathrm{d}\{q\}$ for each coarse-grained particle i. Each particle sustains an internal energy, which defines the particles' number of states via the entropy $s(e)$, fig. 3.1. The microcanonical partition function now reads

$$\mathcal{Z}_{\mathrm{mc}} = \int \prod_{\mathrm{i}} \frac{\mathrm{d}\vec{r}_{\mathrm{i}}\mathrm{d}\vec{p}_{\mathrm{i}}\mathrm{d}e_{\mathrm{i}}}{(2\pi\hbar)^{3nN} n!} \underbrace{\exp\left(\sum_{\mathrm{i}} \frac{s_{\mathrm{i}}(e_{\mathrm{i}})}{k_{\mathrm{B}}} \right)}_{\text{integrated out } \mathbf{DoF}\mathrm{s}} \times \\ \times \delta\left(\sum_{\mathrm{i}} \frac{\vec{p}_{\mathrm{i}}^2}{2m_{\mathrm{i}}} + \sum_{\mathrm{i}<\mathrm{j}} V(\vec{r}_{\mathrm{i}} - \vec{r}_{\mathrm{j}}) + \sum_{\mathrm{i}} e_{\mathrm{i}} - \mathbf{E}_{\mathrm{total}} \right). \tag{3.16}$$

e_{i} are the internal energies of the particles, and s_{i} relates to the internal entropy, which quantifies the number of states of particle i at given internal energy. This microcanonical partition function will be sampled by the **eMC** scheme. Like a thermostat **eMC** updates particles' internal energies and parallel momenta, which

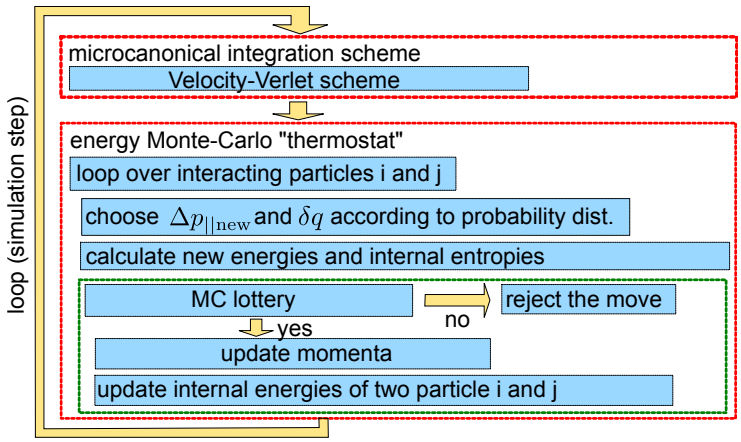

Figure 3.2 Flow chart illustrates the implementation of the **eMC** scheme. It is separated between external and internal **DoF**s by (i) a microcanonical integration scheme (ii) **eMC** lottery with a criterion, which accepts or rejects the new proposed state, modified version from [11].

are accepted according to a Metropolis rate. The external **DoF**s are captured by microcanonical molecular-dynamic, which uses a time-reversible and symplectic Velocity-Verlet integration scheme. The full scheme is illustrated by figure 3.2. New internal energies and parallel momentum are proposed

$$[p_{||}, e_{\mathrm{i}}, e_{\mathrm{j}}]_{\mathrm{old}} \rightarrow [p_{||}, e_{\mathrm{i}}, e_{\mathrm{j}}]_{\mathrm{new}},$$

where the proposed state is accepted with a specific probability by an acceptance criterion (green box fig. 3.2). In the next subsection the microcanonical partition function is rewritten to derive an acceptance criterion for an update procedure of pairs of particles.

3.3.2 eMC: acceptance criterion

eMC acts pairwise on particles i and j at spatial position $\vec{r}_{\mathrm{i}}$,$\vec{r}_{\mathrm{j}}$ with distance $|\vec{r}_{\mathrm{i}} - \vec{r}_{\mathrm{j}}| < \sigma$. σ is chosen equivalent to the range of the soft interaction. In principle, also other choices are possible, e.g., bonded particles interact independent from interaction range. **eMC** couples kinetic energy from external **DoF** to the internal **DoF**s and vice versa. Despite insertion of kinetic energy to external **DoF**s, the local momentum stays unaltered. Hence, the relative momentum is decomposed into a parallel and perpendicular one. According to the Lowe-Andersen thermostat, sec. 3.2.1, this is a free choice, i.e., also an update of the perpendicular momentum is possible. To conserve the centre of mass momentum $\vec{P}$, a relative momentum

$\Delta\vec{p}$ is added to particle j's momentum $\vec{p}_\mathrm{i}$ and subtracted to particle i's momentum $\vec{p}_\mathrm{j}$. Particles have a mass m_i, m_j, and a reduced mass $\mu = \frac{m_\mathrm{i} m_\mathrm{j}}{m_\mathrm{i}+m_\mathrm{j}}$. The centre of mass momentum is $\vec{P} = \vec{p}_\mathrm{i} + \vec{p}_\mathrm{j}$ and the relative momentum is $\Delta\vec{p} = \frac{\mu}{m_\mathrm{j}}\vec{p}_\mathrm{i} - \frac{\mu}{m_\mathrm{i}}\vec{p}_\mathrm{j}$. Inverting these linear relations for centre of mass and relative momenta, one obtains

$$\vec{p}_\mathrm{i} = \frac{\mu}{m_\mathrm{j}}\vec{P} - \Delta\vec{p}, \tag{3.17}$$

$$\vec{p}_\mathrm{j} = \frac{\mu}{m_\mathrm{i}}\vec{P} + \Delta\vec{p}. \tag{3.18}$$

The decomposition is sketched in fig. 3.3 [11]. The relative momentum is decomposed to $\Delta\vec{p} = p_{||}\vec{e}_\mathrm{ij} + \vec{p}_\perp$. $\vec{e}_\mathrm{ij}$ is the unit vector $(\vec{r}_\mathrm{i} - \vec{r}_\mathrm{j})/|\vec{r}_\mathrm{i} - \vec{r}_\mathrm{j}|$. The parallel momenta $p_{||}$ are drawn according to the Maxwell-Boltzmann distribution,

$$P_{T^\mathrm{loc}_\mathrm{old}}(\Delta p_{||\mathrm{new}}) = \frac{1}{\sqrt{2\pi\mu k_\mathrm{B}\bar{T}^\mathrm{loc}_\mathrm{old}}} \cdot \exp\left(-\frac{\Delta p^2_{\parallel\mathrm{new}}}{2\mu k_\mathrm{B}\bar{T}^\mathrm{loc}_\mathrm{old}}\right). \tag{3.19}$$

$T^\mathrm{loc}_\mathrm{old}$ is the local internal temperature of particle i and j, $T^\mathrm{loc}_\mathrm{old} = (T_\mathrm{i} + T_\mathrm{j})/2$. This is a choice, which is not necessary that the choice $T^\mathrm{loc}_\mathrm{old}$ does not have any physical consequence. The temperatures are defined by the derivative of entropy with respect to energy, $T = \left(\frac{\partial s}{\partial e}\right)^{-1}$. The parallel component connects implicit and explicit **DoF**s. Hence, the internal **DoF**s also act like a local heat bath similar to Lowe-Andersen's thermostat because an update takes out or puts in energy into the particle pair i and j, via the expression $\delta\mathcal{T} = \frac{\left(\Delta p^2_{||new} - \Delta p^2_{||old}\right)}{2\mu}$.

The decomposition of momenta allows to rewrite the microcanonical partition function, eq. (3.16), into a microcanonical ensemble,

$$\begin{aligned}\Omega_{\mathrm{mc}} =& \frac{1}{(2\pi\hbar)^{3nN} n!} \int \prod_\mathrm{i} \mathrm{d}\vec{r}_\mathrm{i} \prod_{\mathrm{i}>2} \mathrm{d}\vec{p}_\mathrm{i}\mathrm{d}e_\mathrm{i} \exp\left(\sum_{\mathrm{i}>2} \frac{s(e_\mathrm{i})}{k_\mathrm{B}}\right) \\ &\times \left[\int \mathrm{d}\vec{P}\mathrm{d}^2\Delta p_\perp \mathrm{d}\Delta p_\parallel \mathrm{d}e_1 \mathrm{d}e_2 \exp\left(\frac{s(e_1)+s(e_2)}{k_\mathrm{B}}\right)\right] \\ &\times \delta\left(\frac{\Delta p^2_\perp + \Delta p^2_\parallel}{2\mu} + \frac{\vec{P}^2}{2M} + \sum_{\mathrm{i}<j} V(\vec{r}_\mathrm{i} - \vec{r}_\mathrm{j}) + e_\mathrm{i}(\{q_\mathrm{i}\})\right).\end{aligned} \tag{3.20}$$

which represents all states of the system that are accessible at a fixed total energy. Thus, this sets the base for the **eMC** scheme. The numbers 1 and 2 represent an explicit pair of particles that the product $\prod$ over the entropies $s(e_\mathrm{i})$ starts at $\mathrm{i} = 3$. The explicit pair of particles is presented in the form of decomposed momenta.

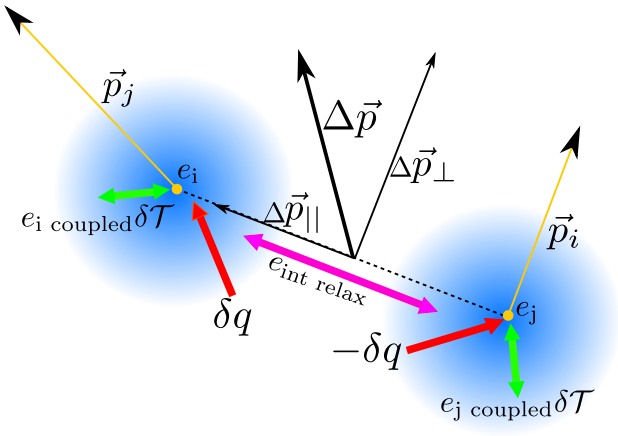

Figure 3.3 Two particles interact for a time Δt. The momenta are decomposed to conserve local momentum, eq. (3.18), (3.17). The energy will be changed by a thermal relaxation with a thermal conductivity κ_{int} between particles a random heat flux δq and a random contribution of kinetic energy $\delta\mathcal{T}$ [11].

$V(\vec{r}_\mathrm{i} - \vec{r}_\mathrm{j})$ denotes a potential acting between pairs of particles. With the condition that **eMC**'s update of parallel momentum and internal energies conserves the total energy of the system, the statistical weight of the two-particle problem is identified by

$$\mathrm{d}\Delta p_{||}\mathrm{d}e_\mathrm{i}\mathrm{d}e_\mathrm{j}\exp\left(\frac{s(e_\mathrm{i})+s(e_\mathrm{j})}{k_\mathrm{B}}\right) = \text{const.} \tag{3.21}$$

The relevant statistical weight of a particle pair remains fully flexible due to the choice of $s(e)$. Hence, particles' entropies $s(e)$ fully cover local equilibrium material properties like specific heat capacity c_V. A Monte-Carlo scheme always relies on detailed balance. The detailed-balance condition is

$$W(\mathcal{S}'|\mathcal{S})P(\mathcal{S}) = W(\mathcal{S}|\mathcal{S}')P(\mathcal{S}'). \tag{3.22}$$

The probability $P(\mathcal{S})$ to be in state $\mathcal{S}$ multiplied by a transition probability W to evolve from state $\mathcal{S}$ to $\mathcal{S}'$ is equal to probability $P(\mathcal{S}')$ in state $\mathcal{S}'$ multiplied by a transition probability W to come from state $\mathcal{S}'$ to $\mathcal{S}$. In our case, the state $\mathcal{S}'$ respectively $\mathcal{S}$ is characterised by three new/old proposed variables: (i) the parallel momentum, which results from the decomposition of the momenta $\vec{p}_1$ and $\vec{p}_2$ of two pairwise interacting particles, (ii) internal energy of the first particle, (iii) internal energy of the second particle. We insert the statistical weight of the two-particle problem into eq. (3.22) and split the probabilities. p_prop is the proposal probability

and p_{acc} the acceptance probability,

$$p_{\mathrm{acc}}^{(+)} \cdot p_{\mathrm{prop}}^{(+)}(\Delta p_{||\,\mathrm{old}}, e_{\mathrm{i\,old}}, e_{\mathrm{j\,old}}) \cdot \exp\left(\frac{s_{\mathrm{i}}(e_{\mathrm{i\,old}}) + s_{\mathrm{j}}(e_{\mathrm{j\,old}})}{k_{\mathrm{B}}}\right) = \tag{3.23}$$

$$p_{\mathrm{acc}}^{(-)} \cdot p_{\mathrm{prop}}^{(-)}(\Delta p_{||\,\mathrm{new}}, e_{\mathrm{i\,new}}, e_{\mathrm{j\,new}}) \cdot \exp\left(\frac{s_{\mathrm{i}}(e_{\mathrm{i\,new}}) + s_{\mathrm{j}}(e_{\mathrm{j\,new}})}{k_{\mathrm{B}}}\right). \tag{3.24}$$

The $^{(+)}$ denotes the forward step and the $^{(-)}$ denotes the backward step. The **eMC** update scheme acts on internal energies e_{i}, e_{j}, and parallel momentum $p_{||}$, but the proposal probability of parallel momentum and new internal energies can be decoupled. The proposal probability is factorised and the probability distribution of parallel momenta is inserted

$$\frac{p_{\mathrm{acc}}^{(+)}}{p_{\mathrm{acc}}^{(-)}} = \frac{P(\Delta p_{||\,\mathrm{old}})}{P(\Delta p_{||\,\mathrm{new}})} \cdot \frac{P(e_{\mathrm{i\,old}}, e_{\mathrm{j\,old}})}{P(e_{\mathrm{i\,new}}, e_{\mathrm{j\,new}})} \cdot \frac{\exp\left(\frac{s_{\mathrm{i}}(e_{\mathrm{i\,new}})+s_{\mathrm{j}}(e_{\mathrm{j\,new}})}{k_{\mathrm{B}}}\right)}{\exp\left(\frac{s_{\mathrm{i}}(e_{\mathrm{i\,old}})+s_{\mathrm{j}}(e_{\mathrm{j\,old}})}{k_{\mathrm{B}}}\right)}. \tag{3.25}$$

This expression specifies the acceptance criterion $p_{\mathrm{acc}}^{(+)}/p_{\mathrm{acc}}^{(-)}$ to sample the micro-canonical partition function independent of the underlying model properties that are chosen in order to mimic physically realistic dynamics. Of coarse, the probabilities $P(e_{\mathrm{i\,new}}, e_{\mathrm{j\,new}})$ and $P(e_{\mathrm{i\,new}}, e_{\mathrm{j\,new}})$ have to be constructed so that total energy of the system is conserved. Hence, a reasonable form for the proposal probability of new internal energies is deduced and the choice of updating the internal energies is expounded. Here, the focus is on physically realistic dynamics. Realistic dynamics dictates the update of two internal energies that correspond to a pair of particle – without an explicit formulation of the distribution factor of energy to internal **DoF**s,

$$e_{\mathrm{i\,new}} = e_{\mathrm{i\,old}} + \delta q_{\mathrm{old}} + \kappa_{\mathrm{int}}\left(\frac{\partial s_{\mathrm{i}}}{\partial e_{\mathrm{i\,old}}} - \frac{\partial s_{\mathrm{j}}}{\partial e_{\mathrm{j\,old}}}\right)\Delta t - \delta\mathcal{T} \cdot (\text{distr. factor}), \tag{3.26}$$

$$e_{\mathrm{j\,new}} = e_{\mathrm{j\,old}} - \underbrace{\delta q_{\mathrm{old}}}_{\text{noise}} - \underbrace{\kappa_{\mathrm{int}}\left(\frac{\partial s_{\mathrm{i}}}{\partial e_{\mathrm{i\,old}}} - \frac{\partial s_{\mathrm{j}}}{\partial e_{\mathrm{j\,old}}}\right)\Delta t}_{\text{thermal relaxation}} - \underbrace{\delta\mathcal{T} \cdot (\text{distr. factor})}_{\text{exchange of } \delta\mathcal{T}}. \tag{3.27}$$

The update of energies is influenced by a random noise, a deterministic thermal relaxation controlled by the inverse internal temperatures, which are calculated by derivative of entropy with respect to energy, and a distribution factor, which controls the split of kinetic energy $\delta\mathcal{T}$ to the particles' internal energy. The form of the equation guarantees that the newly proposed state leaves the total energy of the

system unaltered, $\frac{\Delta p_{\parallel}^2}{2\mu} + e_\mathrm{i} + e_\mathrm{j} = \text{const.}$ [2]. The random noise is drawn according to a Gaussian distribution

$$\delta q_\mathrm{old} \Leftarrow P(\delta q_\mathrm{old}) = \frac{1}{\sqrt{2\pi\sigma_q}} \exp\left(-\frac{\delta q_\mathrm{old}^2}{2\sigma_q}\right). \tag{3.28}$$

The distribution is normalised according to the $\sigma_q = 2\kappa_\mathrm{int}\Delta t$. κ_int denotes the thermal relaxation constant between particles i and j. Also, other probability distributions are possible, but in the limit that the number of **DoF**s, which have been integrated out, is large, a Gaussian distribution is a good choice to describe additional thermal fluctuations, i.e., distribution follows central limit theorem. In the update of internal energies, the main idea introducing this random part is that the deterministic energy exchange is accompanied by a random one δq.

The deterministic thermal relaxation part is controlled by its thermal relaxation constant κ_int and the difference of the inverse temperatures. Finally, the split of kinetic energy difference $\delta\mathcal{T} = \frac{\left(\Delta p_{||\ \mathrm{new}}^2 - \Delta p_{||\ \mathrm{old}}^2\right)}{2\mu}$ to the internal energies, e_i and e_j, is specified. Hence, the goal is to formulate an expression, which splits the exchange of $\delta\mathcal{T}$. Energy change is chosen such that the sum of the internal entropies s_i and s_j of particles i and j is maximal. δe_i is the change of internal energy of particle i,

$$MAX\left(s_\mathrm{i}(e_{\mathrm{i\ old}} + \delta e_{\mathrm{i\ old}}) + s_\mathrm{j}(e_{\mathrm{j\ old}} + \delta\mathcal{T} - \delta e_{\mathrm{i\ old}})\right). \tag{3.29}$$

The maximum value is deduced by expanding this equation for small δe_i and $\delta\mathcal{T}$ to first-order and differentiate

$$\underbrace{\frac{\partial s_\mathrm{i}}{\partial e_\mathrm{i}} - \frac{\partial s_\mathrm{j}}{\partial e_\mathrm{j}}}_{\text{Zero for equilibrium}} + \frac{\partial^2 s_\mathrm{i}}{\partial e_\mathrm{i}^2}\delta e_\mathrm{i} + \frac{\partial^2 s_\mathrm{j}}{\partial s_\mathrm{j}^2}\delta e_\mathrm{i} + \frac{\partial^2 s_\mathrm{j}}{\partial e_\mathrm{j}^2}\delta\mathcal{T} + \mathcal{O}(\delta e^2) = 0. \tag{3.30}$$

The first two terms correspond to the thermal relaxation, which is assumed to be zero for the equilibrium. Solving this equation for δe_i leads to an expression that corresponds to the energy exchange between internal and external degrees of freedom. Thus, equation (3.26) and (3.27) can be expanded by an explicit term to

[2] This condition already sustained the statistical weight of the two-particle problem in the microcanonical ensemble, eq. (3.20).

distribute the energy to internal energies,

$$e_{\mathrm{i\ new}} = e_{\mathrm{i\ old}} + \delta q_{\mathrm{old}} + \kappa_{\mathrm{int}} \left(\frac{\partial s_{\mathrm{i\ old}}}{\partial e_{\mathrm{i\ old}}} - \frac{\partial s_{\mathrm{j\ old}}}{\partial e_{\mathrm{j\ old}}} \right) \Delta t - \left(\frac{\frac{\partial^2 s_{\mathrm{j\ old}}}{\partial e^2_{\mathrm{j\ old}}}}{\frac{\partial^2 s_{\mathrm{i\ old}}}{\partial e^2_{\mathrm{i\ old}}} + \frac{\partial^2 s_{\mathrm{j\ old}}}{\partial e^2_{\mathrm{j\ old}}}} \right) \delta \mathcal{T}, \quad (3.31)$$

$$e_{\mathrm{j\ new}} = e_{\mathrm{j\ old}} - \delta q_{\mathrm{old}} - \kappa_{\mathrm{int}} \left(\frac{\partial s_{\mathrm{i\ old}}}{\partial e_{\mathrm{i\ old}}} - \frac{\partial s_{\mathrm{j\ old}}}{\partial e_{\mathrm{j\ old}}} \right) \Delta t - \underbrace{\left(\frac{\frac{\partial^2 s_{\mathrm{i\ old}}}{\partial e^2_{\mathrm{i\ old}}}}{\frac{\partial^2 s_{\mathrm{i\ old}}}{\partial e^2_{\mathrm{i\ old}}} + \frac{\partial^2 s_{\mathrm{j\ old}}}{\partial e^2_{\mathrm{j\ old}}}} \right)}_{\text{weights } \delta\mathcal{T} \text{ to specific heat}} \delta \mathcal{T}. \quad (3.32)$$

A visualisation of eq. (3.31) and (3.32) is shown in figure 3.3. The yellow point represents the particles' centre of mass. The green arrow indicates the exchange of internal and external energy, which is given by the last part of equation (3.31). The red arrows represent the thermal noise (the analogue is the second part of equation (3.31)) and the magenta arrow indicates the deterministic thermal relaxation, κ_{int}. In eq. (3.19) and (3.28) the parallel momentum, $\Delta p_{\parallel}$, and thermal noise, δq_{new}, are Gaussian distributed. Thus, the new parallel momentum $\Delta p_{\parallel new}$ is drawn according to Gaussian distribution, referring to equation (3.19). The thermal noise of the interaction is characterised by δq. The fluctuations of δq are controlled by the probability distribution (3.28). The form of this noise was chosen to be Gaussian, which can be motivated by the spirit of a thermostat controlled by a heat bath with normalisation $\sigma_{\mathrm{q\ old}}$. The proposed new state gives rise to determine the old state δq_{old} (3.31) and δq_{new} by the reverse step of equation (3.31)

$$\begin{aligned} \delta q_{\mathrm{old}} =& e_{\mathrm{i\ new}} - e_{\mathrm{i\ old}} - \kappa_{\mathrm{int}} \left(\frac{\partial s_{\mathrm{i\ old}}}{\partial e_{\mathrm{i\ old}}} - -\frac{\partial s_{\mathrm{j\ old}}}{\partial e_{\mathrm{j\ old}}} \right) \Delta t \\ &+ \left(\frac{\frac{\partial^2 s_{\mathrm{j\ old}}}{\partial e^2_{\mathrm{j\ old}}}}{\frac{\partial^2 s_{\mathrm{i\ old}}}{\partial e^2_{\mathrm{i\ old}}} + \frac{\partial^2 s_{\mathrm{j\ old}}}{\partial e^2_{\mathrm{j\ old}}}} \right) \delta \mathcal{T}, \end{aligned} \quad (3.33)$$

$$\begin{aligned} \delta q_{\mathrm{new}} =& e_{\mathrm{i\ old}} - e_{\mathrm{i\ new}} - \kappa_{\mathrm{int}} \left(\frac{\partial s_{\mathrm{i\ new}}}{\partial e_{\mathrm{i\ new}}} - \frac{\partial s_{\mathrm{j\ new}}}{\partial e_{\mathrm{j\ new}}} \right) \Delta t \\ &- \left(\frac{\frac{\partial^2 s_{\mathrm{j\ new}}}{\partial e^2_{\mathrm{j\ new}}}}{\frac{\partial^2 s_{\mathrm{i\ new}}}{\partial e^2_{\mathrm{i\ new}}} + \frac{\partial^2 s_{\mathrm{j\ new}}}{\partial e^2_{\mathrm{j\ new}}}} \right) \delta \mathcal{T}. \end{aligned} \quad (3.34)$$

$\delta\mathcal{T}$ denotes the change of kinetic energy caused by the insertion of the drawn parallel momentum of particles i and j. Thus, the general acceptance criterion, eq. (3.25),

results in

$$\frac{p_{\text{acc}}^{(+)}}{p_{\text{acc}}^{(-)}} = \sqrt{\frac{\sigma_{p\ \text{old}}\sigma_{q\ \text{old}}}{\sigma_{p\ \text{new}}\sigma_{q\text{new}}}} \exp\left(\frac{s_{\text{i}}(e_{\text{i new}}) + s_{\text{j}}(e_{\text{j new}}) - s_{\text{i}}(e_{\text{i old}}) - s_{\text{j}}(e_{\text{j old}})}{k_{\text{B}}}\right) \times \\ \times \exp\left(-\frac{\Delta p_{\parallel\ \text{old}}^2}{2\sigma_{p_{\parallel\ \text{old}}}} + \frac{\Delta p_{\parallel\ \text{new}}^2}{2\sigma_{p_{\parallel\ \text{new}}}} + \frac{\delta q^2{}_{\text{old}}}{2\sigma_{q_{\text{old}}}} - \frac{\delta q^2{}_{\text{new}}}{2\sigma_{q_{\text{new}}}}\right). \tag{3.35}$$

Here, the deterministic thermal relaxation is accompanied by the random one given by the probability distribution $P(\delta q_{\text{old}})$ of the random noise δq. We will accept a step if a random number ξ_r will be smaller than the acceptance criterion of the current step. The random number ξ_r is uniformly distributed between $[0, 1]$.

$$p_{\text{acc}} = \min\left[1, \frac{P_{\bar{T}_{\text{new}}^{\text{loc}}}(\Delta p_{\parallel\text{old}})}{P_{\bar{T}_{\text{old}}^{\text{loc}}}(\Delta p_{\parallel\text{new}})} \frac{P(\delta q_{\text{new}})}{P(\delta q_{\text{old}})} \frac{e^{\frac{s(e_{\text{i new}})+s(e_{\text{j new}})}{k_{\text{B}}}}}{e^{\frac{s(e_{\text{i old}})+s(e_{\text{j old}})}{k_{\text{B}}}}}\right] \tag{3.36}$$

Finally, the key aspects of **eMC** method are:

- The acceptance criterion is based on the decomposed microcanonical partition function. Hence, the Monte-Carlo scheme is flexible to the choice of internal entropies $s(e)$ and the related physical mechanisms that control the proposed new internal energies, i.e., entropy must be differentiable with respect to energy, e.

- The algorithm works independently from the choice of the form of the internal entropy.

- The internal thermal relaxation parameter, κ_{int}, can be addressed to an underlying complex structure, i.e., this allows to distinguish between intra- and inter-molecular thermal relaxation.

- It is numerically more stable than a first-order **eDPD** scheme. Hence, it gives access to study collective processes on long time and length scales.

Table 3.1 concludes main characteristics, i.e., parameters of **eMC**. They are structured into their dependence onto external or internal **DoF**s. The right column gives information about connection and dependencies of other parameters. At this point, **eMC** is the only method that allows to decouple the physics of internal **DoF** and a classic microcanonical integration scheme via one universal Monte-Carlo scheme.

parameter	description	dependence
microcanonical properties - external **DoF**		
R_e	averaged end-to-end distance	
$\bar{\mathcal{N}}$	degree of polymerisation	$\bar{\mathcal{N}} = (\rho b^3)^2 N$
N	number of segments	$\bar{\mathcal{N}}$
$b\sigma^{-1} = 1$	averaged harmonic bond distance	$\bar{\mathcal{N}}$
$\rho_0 \sigma^3$	density of the system	$\bar{\mathcal{N}}$
v_ij	soft interaction parameter	eq. (3.52)
	(other potentials are possible)	
$\Delta p_{\|\|\mathrm{old}}$	couples int.& ext. energy	$\Delta p_{\|\|} \leftarrow P(\Delta p_{\|\|})$, eq. (3.19)
	drawn from Gaussian distr.	
$\delta\mathcal{T}$	difference in kinetic energy	$\Delta p_{\|\|}, \alpha_\mathrm{couple}$
α_couple	controls correlation between	
	$\Delta p_{\|\|\mathrm{old}}$, $\Delta p_{\|\|\mathrm{new}}$	–
$T^\mathrm{ext} k_\mathrm{B}$	external temperature	$\frac{2}{3}\left\langle \frac{m_\mathrm{i}}{2} v_\mathrm{i}^2 \right\rangle_N$,eq. (3.53)
$\mathrm{d}\tau_{md}^\mathrm{verlet}$	increment of integration	
thermal properties - internal **DoF**		
e_int	internal energy	$k_\mathrm{B} T$
$s(e_\mathrm{int})$	internal entropy	$c_V \ln(e)$
c_V	internal specific heat capacity	exp. data
	$\partial_e(s(e))$ and $\partial_e^2(s(e))$ have to exist.	
δq	thermal noise	eq. (3.28)
κ^int	internal (intra or inter)	
	thermal relaxation constant	
κ_inter	determin. relax. of $e_\mathrm{i}, e_\mathrm{j}$	c-g. particle type
κ_intra	determin. relax. of $e_\mathrm{i}, e_\mathrm{j}$	c-g. architecture
κ_{intra}	maximal relaxation	max. $s(e)$, eq. (3.38)
$T^\mathrm{int} k_\mathrm{B}$	internal temperature [11]	$\frac{\langle e \rangle}{c_v/k_\mathrm{B}+1}$
$\mathrm{d}\tau_{md}^\mathrm{eMC}$	increment of call eMC	

Table 3.1 An overview about obligatory and free choices of the **eMC** scheme. It is distinguished between internal and external **DoF**s.

3.3.3 eMC: limiting cases of thermal conductivity

Two limiting cases of the **eMC** scheme are considered. In the first case the internal thermal relaxation constant κ_{int} equals zero. Thus, there is no internal coupling between two interacting particles any more. In consequence, the internal energy acts like a local thermostat only. If a portion of energy is added to a single particle's internal energy, this energy will relax such that kinetic and internal temperature end up in thermal equilibrium. We conclude that the internal **DoF**s, e_{i} and e_{j}, only interact via $\Delta p_{\parallel}$, and the acceptance probability reads

$$p_{\text{acc}} = \min\left[1, \frac{P_{\bar{T}^{\text{loc}}_{\text{new}}}(\Delta p_{\parallel \text{old}})}{P_{\bar{T}^{\text{loc}}_{\text{old}}}(\Delta p_{\parallel \text{new}})} \frac{e^{\frac{s(e_{\text{i new}})+s(e_{\text{j new}})}{k_{\text{B}}}}}{e^{\frac{s(e_{\text{i old}})+s(e_{\text{j old}})}{k_{\text{B}}}}}\right]. \tag{3.37}$$

In the second case the maximum relaxation is deduced. The maximum thermal relaxation corresponds to an instantaneous equal temperature of two interacting internal **DoF**s. The maximum of internal thermal relaxation is reached if an over damping of internal energies starts. Due to the discreteness of Δt, the cold particle could become hotter than the hot particle, if $\kappa^{\text{int}}\Delta t$ were chosen non-physically large. The maximal value of κ_{int} immediately equilibrates the local temperatures, $\frac{\partial s_{\text{i}}}{\partial e_{\text{i}}}\Big|_{e_{\text{i}}+\delta e_{\text{i}}^{\text{int}}} = \frac{\partial s_{\text{j}}}{\partial e_{\text{j}}}\Big|_{e_{\text{j}}-\delta e_{\text{i}}^{\text{int}}}$. This requirement yields

$$\kappa^{\text{int}}_{\text{max}}\Delta t \approx \frac{-1}{\frac{\partial^2 s_{\text{i}}}{\partial e_{\text{i}}^2} + \frac{\partial^2 s_{\text{j}}}{\partial e_{\text{j}}^2}} = \frac{c_{\text{i}}^{\text{loc}} c_{\text{j}}^{\text{loc}} T_{\text{i}}^{\text{loc2}} T_{\text{j}}^{\text{loc2}}}{c_{\text{i}}^{\text{loc}} T_{\text{i}}^{\text{loc2}} + c_{\text{j}}^{\text{loc}} T_{\text{j}}^{\text{loc2}}}. \tag{3.38}$$

If κ_{int} was chosen higher than this limiting value the acceptance rate will decrease, cf. fig. 4.5.

3.4 Universal, soft, coarse-grained model of polymer melt

The **DoF**s, which have been integrated out, have to be specified by a functional form. If the **DoF**s are lumped together to an internal energy, they are in equilibrium with themselves and have no dynamics. Hence, the internal **DoF** of each particle - internal energy e is controlled by an entropy energy relation $s(e)$, which quantifies the internal states of the internal **DoF** at a given energy e. All states are equilibrium states. The form of the internal entropy has to be differentiable with respect to

internal energy to be related to inverse temperature, $\partial s(e)/\partial e = 1/T_{\mathrm{loc}}$. The simulations are performed on a level where polymers have universal behaviour. Therefore, the universal description is restricted that the coarse-grained model reproduces the invariant property R_{e}, at a specific temperature T in equilibrium [11]. The system will have bonded and non-bonded interactions, bonded interactions will be harmonic and non-bonded will be covered by a density approximation, which is related to the particles' spatial positions. Hence, the Hamiltonian, $\hat{\mathcal{H}}$, is comprised of three parts: (i) kinetic energy $\hat{\mathcal{T}} = \sum_i \frac{\mathbf{p}_i^2}{2m}$, (ii) bonded interactions, $\hat{\mathcal{H}}_{\mathrm{b}}$, and (iii) non-bonded interactions, $\hat{\mathcal{H}}_{\mathrm{nb}}$.

Bonded interactions are described by entropic springs. This choice implies that particles mimic a Gaussian distribution along the polymer chain and exhibit random-walk-like statistics.

$$\hat{\mathcal{H}}_{\mathrm{b}} = \frac{3k_{\mathrm{B}}T}{2b^2} \sum_{i}^{nN} \Delta\mathbf{r}_i^2. \tag{3.39}$$

Here, $\Delta\mathbf{r}_i$ represents the distance between bonded particles, and ${R_{\mathrm{e}}}^2 = b^2N$ denotes the unperturbed end-to-end distance of the polymer. Coincidentally, the related statistical segment length $b = \sigma$ is the smallest relevant length scale in the model. The number of polymers is n. The number of spatial positions that form each polymer is $N+1$, consequently the number of bonds is $(N+1)-1 = N$. Hence, the sum runs over all nN bonds. Our coarse-grained model is parametrised to reproduce the invariant property, R_{e}, at a specific temperature T in equilibrium. Thus, we choose $k_{\mathrm{conf}} = k_{\mathrm{B}}T/b^2$. In the subsequent work, the non-equilibrium simulation, k_{conf} is fixed, i.e., it does not depend on the local temperature.

Non-bonded interactions are assumed to be of the form $\hat{\mathcal{H}}_{\mathrm{nb}} = \sum_{\mathrm{i}<\mathrm{j}} V(\mathbf{r}_{\mathrm{i}} - \mathbf{r}_{\mathrm{j}})$ with a soft pair potential, V. This soft repulsion stems for the excluded volume on the atomistic scale. In our coarse-grained model, the strength of this repulsion is chosen large enough to restrain fluctuations of the total density on the smallest relevant length scale of the coarse-grained description, i.e., we do not attempt to reproduce the isothermal compressibility of the underlying atomistic description. In accord with previous studies, we choose $V(\mathbf{r})/k_{\mathrm{B}}T = K_{\mathrm{iso}}v(\mathbf{r})$ where K_{iso} quantifies the inverse isothermal compressibility. The potential form is $v(\mathbf{r}) = \frac{15}{2\pi\rho\sigma^3}(1 - \frac{|\mathbf{r}|}{\sigma})^2$

for $|\mathbf{r}| < \sigma$ and 0 otherwise with an averaged density $\rho_0 = n(N+1)/V$ [11].

$$\hat{\mathcal{H}}_{\mathrm{nb}} = \sum_{\mathrm{i<j}} V(\mathbf{r}_\mathrm{i} - \mathbf{r}_\mathrm{j}) \approx \frac{K_{\mathrm{iso}} k_\mathrm{B} T N}{2} \cdot \frac{\rho_0 R_e^3}{N} \int \frac{\mathrm{d}^3 r}{R^3} (\hat{\phi}(\mathbf{r}) - 1)^2 \tag{3.40}$$

$$= \frac{K_{\mathrm{iso}} k_\mathrm{B} T \rho_0}{2} \int \mathrm{d}r^3 (\hat{\phi}(\mathbf{r}) - 1)^2 \tag{3.41}$$

Here, $\hat{\phi}(\mathbf{r}) = \frac{1}{\rho} \sum_\mathrm{i} \delta(\mathbf{r} - \mathbf{r}_i)$ are the local normalised densities. The fluctuations of the local normalised density are on the length scale ΔL and scale like $\Delta L^3 \langle (\hat{\phi} - \langle \hat{\phi} \rangle)^2 \rangle = \frac{1}{K_{\mathrm{iso}} \rho}$. This can also be characterised by a correlation length $\xi = b/\sqrt{12 K_{\mathrm{iso}}}$. [3] Under this assumption, we fix $k_{\mathrm{comp}} = k_\mathrm{B} T K_{\mathrm{iso}}$, where T characterizes the equilibrium thermodynamic state, at which the model is parametrised. Recollect the main idea we want to find a functional form of the internal entropy $s(e)$. Every degree of freedom, which has been integrated out cannot contribute to the conformational entropy, in order to this they have to be recovered by a collective degree of freedom - internal energy. Hence, the total free energy of the system is fixed and invariant under the level of coarse-graining. The idealised partition function of the system can be expressed by

$$Z_\mathrm{k} = \int \frac{\mathrm{d}r^{3(N+1)n} \mathrm{d}p^{3(N+1)n}}{h^{3(N+1)n} n!} \exp\left(- \frac{\hat{\mathcal{H}}(\{r\}, \{p\})}{k_\mathrm{B} T} \right)$$

$$= \int \frac{\mathrm{d}r^{3(N+1)n} \mathrm{d}p^{3(N+1)n}}{h^{3(N+1)n} n!} \exp\left(- \frac{\hat{\mathcal{T}} + \hat{\mathcal{H}}_\mathrm{b}(\{r\}) + \hat{\mathcal{H}}_{\mathrm{nb}}[\hat{\phi}(\{r\})]}{k_\mathrm{B} T} \right). \tag{3.42}$$

The partition function can be related to a free energy, which will be our invariant quantity, $\frac{F}{k_\mathrm{B} T} \sim -\ln(Z_\mathrm{k})$. The canonical ensemble at temperature T and the free energy are decoupled into two contributions of (i) Gaussian chains - the conformational part, (ii) the non-bounded energy, which has been replaced by density fluctuations [11]. If consecutive coarse-graining is applied, contribution of the internal **DoF**s are taken into account, too. The conformational part is calculated from the Hamiltonian, $\mathcal{H}_\mathrm{b}(\{r\})$, where each bond contribution of distance between bonded particles $\Delta \mathbf{r}_i$

[3] This correlation length characterizes the crossover from intramolecular density fluctuations on short length scales to an almost incompressible liquid on large length scales. The correlation length can be calculated by the structure factor of a homopolymer melt in a random phase approximation [58], which is utilised for small wave vectors, $qR_e \ll 1$, $S(q) \propto \frac{1}{1+(\xi q)^2}$, with $\xi = b/\sqrt{12 K_{\mathrm{iso}}}$.

decouples into a Gaussian integral

$$\begin{aligned}&\frac{F_{\mathrm{conf}}}{k_{\mathrm{B}}T} \sim -\frac{3}{2}nN\ln(k_{\mathrm{B}}T/k_{\mathrm{conf}}),\\ \Rightarrow&\frac{E_{\mathrm{conf}}}{k_{\mathrm{B}}T} \sim \frac{3}{2}nN, \quad \frac{S_{\mathrm{conf}}}{k_{\mathrm{B}}} \sim \frac{3}{2}nN\ln(k_{\mathrm{B}}Te/k_{\mathrm{conf}}).\end{aligned}$$

The end-to-end distance R_{e} always represents an invariant property at a specific temperature T in equilibrium. The contribution of density fluctuations scales as follows

$$\begin{aligned}&\frac{F_{\mathrm{comp}}}{k_{\mathrm{B}}T} \sim \frac{1}{2}(V/\xi^3)\ln(K_{\mathrm{iso}}\rho\xi^3) = -\frac{1}{2}\frac{nN}{\rho\xi^3}\ln(k_{\mathrm{B}}T/k_{\mathrm{comp}}\rho\xi^3),\\ \Rightarrow&\frac{E_{\mathrm{comp}}}{k_{\mathrm{B}}T} \sim \frac{1}{2}\frac{nN}{\rho\xi^3}, \quad \frac{S_{\mathrm{comp}}}{k_{\mathrm{B}}} \sim \frac{1}{2}\frac{nN}{\rho\xi^3}\ln(k_{\mathrm{B}}Te/k_{\mathrm{comp}}\rho\xi^3).\end{aligned}$$

ξ is the correlation length of density fluctuations, because the free energy is claimed to be invariant under successive coarse-graining. Hence, the free energy difference of two consecutive coarse-grained steps is described by an internal free energy - $F_{\mathrm{int}} = F - F'$. Before following this approach, we condition the directive that (i) the form of $\hat{\mathcal{H}}_{\mathrm{b}}$ is invariant under coarse-graining, i.e., lumping two particles into a new, coarser particle, $N \to N' = N/2$, only the parameter b changes according to $b \to b' = \sqrt{2}b$ for the physically relevant property R_{e} to remain invariant [59]. Additionally, it is required that (ii) in the soft, coarse-grained model, the ratio ξ/b remains unaltered under coarse-graining, corresponding to an invariant K_{iso}. The approach has to be independent from temperature, which could be considered a contradiction, but we will consider situations that deal with small temperature gradients only. We perform a top-down approach and use experimental data, which will include a temperature dependency. The major part of external degrees of freedom, spatial positions, and momenta that have been integrated out will enter into the internal energy contribution per segment. N' indicates the number of coarser particles of a chain, which remain by successively lumping two particles together. On a high level of coarse graining, the energy and entropy take the form

$$\frac{e}{k_{\mathrm{B}}T} \sim \frac{1}{2}N/N'(3\alpha + \frac{\beta}{\rho\xi^3}) \quad , \frac{s}{k_{\mathrm{B}}} \sim \frac{1}{2}N/N'(3\alpha + \frac{\beta}{\rho\xi^3})\ln k_{\mathrm{B}}T + \mathrm{const.} \tag{3.43}$$

Therefore, eliminating temperature, we obtain the universal form,

$$s(e) = c_V \ln(e) + \mathrm{const}, \tag{3.44}$$

after multiple coarse-graining steps of a Gaussian polymer melt. c_V is related to the specific heat of the internal-energy reservoir. In our top-down modelling scheme the parameters, averaged end-to-end distance R_e, density $\rho {R_\mathrm{e}}^3/N$, specific heat capacity c_V/k_B are taken in comparison to experimental data. These model parameters determine the thermodynamics of our universal, soft, coarse-grained model. For a given entropy $s(e)$ of internal **DoF**s, we express the first and second derivatives, $\frac{\partial s}{\partial e} = \frac{1}{T^\mathrm{loc}(e)}$ and $\frac{\partial^2 s}{\partial e^2} = -\frac{1}{c^\mathrm{loc} T^\mathrm{loc}}$, via the local temperature $T^\mathrm{loc}(e)$ and specific heat $c^\mathrm{loc}(e)$ of the particle [11]. This form also allows a rescaling of the simulation parameter, which permits observation of steady-state temperature profiles, i.e., thermal conductivities, invariant to explicit discretisation of polymers' segments, sec. 4.2. Due to the flexibility of internal entropy in **eMC**, also other forms of coarse-grained models for complex molecules can enter in $s(e)$, i.e., models derived by first principle calculations [60].

3.5 Details on the implementation

In the previous section, the **eMC** method was introduced. In the following, details about the implementation are discussed. The implementation of the coarse-grained model has to recover (i) conformational (ii) thermodynamic (iii) dynamic properties. The **eMC** scheme has been devised by the idea of a thermostat, momenta and coordinates of a coarse-grained particle are updated by a short molecular-dynamics **MD** simulation using the Velocity-Verlet integration scheme. This scheme locally conserves momentum and energy, but leaves the internal **DoF**s unaltered. Thus, the Velocity-Verlet scheme is presented and details on parametrisation of non-bonded potential to recover χN and $\kappa_\mathrm{iso} N$ are discussed.

3.5.1 Integration scheme - Velocity-Verlet

The external **DoF**s interact via bonded and non-bonded potentials, pairwise forces $f(r) = -\nabla_r V(r)$, respectively. The simulation uses a microcanonical integration scheme - Velocity-Verlet algorithm - to integrate the equations of motion of explicit **DoF**s. The Velocity-Verlet integration scheme

$$\vec{x}(t+\Delta t) = \vec{x}(t) + \vec{v}(t)\Delta t + \frac{\Delta t^2}{2}\vec{f}(t) + \mathcal{O}(\Delta t^3), \tag{3.45}$$

$$\vec{v}(t+\Delta t) = \vec{v}(t) + \frac{(\vec{f}(t) + \vec{f}(t+\Delta t))}{2}\Delta t + \mathcal{O}(\Delta t^3), \tag{3.46}$$

approximates the exact integration by two half steps with a step with constant coordinates, and a step with constant velocities [61]. The algorithm satisfies two aspects. Firstly, the scheme is time reversible. Thus if a step of the form $\vec{x} \to \vec{x}(t + \Delta t)$ is applied, one inverts the velocity $v(t + \Delta t) \to -v(t + \Delta t)$ and performs a Velocity-Verlet step again. The new position $\vec{x}(t + 2\Delta t)$ is equal to the starting position $\vec{x}(t)$. This is important, because if two particle pairs get a new velocity drawn from a probability distribution that corresponds to the same velocity with different sign, the position will be the same like before, i.e., it ensures a detailed balanced Monte-Carlo move. Secondly, the numeric solution is very close to the true Hamiltonian and for time-step $\Delta t \to 0$ approaches the true Hamiltonian - symplectic [62, 63].

3.5.2 Potentials

The coarse-graining procedure reduces the explicit degrees of freedom to a minimal set of potentials and parameters: isothermal compressibility, κN, invariant degree of polymerisation, $\bar{\mathcal{N}}$, averaged end-to-end distance, R_e, and in case of polymer blends incompatibility, χN, is added [64]. Bonds are represented by a harmonic potential, which yields the polymers to be a Gaussian chain and fulfil Rouse dynamics.

$$V_{\mathrm{b}}(|r|) = \frac{E_B}{2}|r|^2 \tag{3.47}$$

Here, E_B is the harmonic bonding constant, r is in units of σ. Likewise $E_B\sigma^2/k_BT = 3$ is chosen resulting in an averaged bond distance of $b\sigma^{-1} = 1$. Non-bonded interactions are realised by a soft repulsive interaction. The soft characteristics are a result of the coarsening procedure [64]. Qualitatively summarised, two coarse-grained particles can overlap while the particles that they represent, have a strict volume exclusion. Non-bonded potential

$$V_{\mathrm{nb}}(|r|) = \frac{v_{ij}}{2}(1 - |r|)^2 \tag{3.48}$$

has a cut-off distance at $r = 1\sigma$. The soft repulsion is controlled by interaction constant, v_{ij}. To map this constant onto incompressibility, κN, and incompatibility parameter, χN, one can formulate the Hamiltonian, eq. (3.49), approximately by a pairwise interaction, eq. (3.50). It is assumed that packing effects are negligible and the radial pair distribution function equals $g(r) = 1$, which is a good assumption

for dense systems of soft coarse-grained particles.

$$\mathcal{H}_{\mathrm{nb}} = \frac{k_{\mathrm{B}}T\sqrt{\bar{\mathcal{N}}}}{R_e^3}\int \mathrm{d}r^3 \left(\frac{\kappa N}{2}(\hat{\phi}_{\mathrm{A}}+\hat{\phi}_{\mathrm{B}})^2 + \chi N\hat{\phi}_{\mathrm{A}}\hat{\phi}_{\mathrm{B}}\right) \tag{3.49}$$

$$\approx \sum_{\mathrm{i<j}} V_{\mathrm{nb}}(r-r') = \frac{1}{2}\sum_{\mathrm{ji}} V_{\mathrm{nb}}(r-r') \tag{3.50}$$

Here, $k_{\mathrm{B}}T$ sets the energy. $\bar{\mathcal{N}}$ is the invariant degree of polymerisation and R_e the averaged end-to-end distance. In eq. 3.50, the self-interaction in the virial has been neglected. Afterwards, the non-bonded potential is inserted and eq. 3.50 rewritten into an integral form, and expanded for density $\phi(r) = \rho_0^{-1}\sum\delta(r-r_i)$.

$$\mathcal{H}_{\mathrm{nb}} \approx \frac{1}{2}\int \mathrm{d}r \int \mathrm{d}r' \rho_0^2 \phi(r)\left(\phi(r) + \nabla\phi(r)(r-r') + \dots\right) V(r-r')$$

This integral is solved for a spherical symmetry. Hence, 4π follows from integration over $\mathrm{d}\vartheta$ and $\mathrm{d}\varphi$.

$$\mathcal{H}_{\mathrm{nb}} = \frac{4\pi\rho_0^2}{2}\int \mathrm{d}|r|\cdot|r|^2 \left(\frac{v_{\mathrm{ij}}}{2}(1-|r|)^2\right)\int \mathrm{d}r\hat{\phi}^2 = \frac{1}{2}\rho_0^2\frac{\pi r_0^3}{30}\int \mathrm{d}\hat{\phi}^2 \tag{3.51}$$

Combining this with eq. (3.49) yields the relation

$$v_{\mathrm{ij}} = \frac{15\cdot k_{\mathrm{B}}T\cdot(\kappa+\chi)N\sqrt{\bar{\mathcal{N}}}}{\pi R_e^3\rho_0^3 r_0^3} \approx \frac{15(\kappa+\chi)}{\pi\rho_0 r_0}. \tag{3.52}$$

This equation relates the isothermal compressibility κN and incompatibility χN of two monomer types A and B to the interacting constant v_{ij} of the soft bonded potential, eq. (3.48).

3.5.3 Temperatures

The simulation couples **eMC** to a microcanonical integration scheme. Hence, system can be characterised by different approaches of temperature. One possibility is to relate the kinetic energy with an averaged **kinetic temperature** of the system.

$$T^{\mathrm{ext}}k_{\mathrm{B}} = \frac{2}{3}\left\langle\frac{m_{\mathrm{i}}}{2}\vec{v}_{\mathrm{i}}^2\right\rangle_N \tag{3.53}$$

The average runs over N particles. m represents the mass and v is the velocity of the i-th particle. Assuming that N is large one defines the external temperature

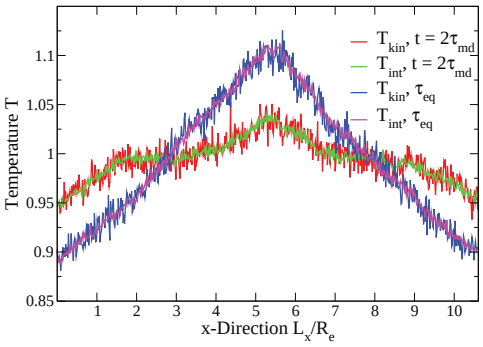

Figure 3.4 Snapshot of temperature profiles of internal and kinetic temperature in a transient and stationary state of a **RNEMD** simulation. $\kappa^{\text{int}}\tau_{\text{md}}/(k_{\text{B}}T^2) = 100$. T is in reduced units $k_{\text{B}}T = 1$. In real units it matches a temperature around $\approx$ 400 Kelvin. Hence, the system is above the glass temperature [11].

according to the volume of slabs chosen to perform the **RNEMD** technique. The **internal temperature** is defined by the inverse of the derivative of the internal entropy. Therefore, the microcanonical partition function is calculated considering that internal **DoF** are only related to an internal temperature.

$$\mathcal{Z}_{\text{mc}} = \frac{1}{N!}\int_0^E \mathrm{d}e_1 \cdots \int_0^E \mathrm{d}e_N \exp\left(\sum_{\text{i}} s(e_{\text{i}})\right)\delta(E - \sum_{\text{i}} e_{\text{i}}) \tag{3.54}$$

N denotes the number of energies e_{i}, and the entropy takes the form $s(e) = c_V \ln(e)$. The delta function is expressed in a Fourier representation.

$$\begin{aligned}\mathcal{Z}_{\text{mc}} &= \frac{1}{N!}\int_0^E \mathrm{d}e_1 \cdots \int_0^E \mathrm{d}e_N \prod_i e_{\text{i}}^{c_V}\frac{1}{2\pi}\int_{-\infty}^{\infty}\mathrm{d}k \exp\left(ikE - \sum_{\text{i}} ike_{\text{i}}\right)\\ &= \frac{1}{N!}\int_{-\infty}^{\infty}\mathrm{d}k \exp(ikE)\left[\int_0^E \mathrm{d}e\; e^{c_V}\exp(-ike)\right]^N\end{aligned}$$

The integral for $\left[\int_0^E \mathrm{d}e\; e^{c_V}\exp(-ike)\right]$ is replaced by a Debye function $g(kE)$, $\left[E^{c_V+1}\int_0^1 \mathrm{d}x\; x^{c_V}\exp(-ikEx)\right] = [E^{c_V+1}g(kE)]$.

$$\mathcal{Z}_{\text{mc}} = \frac{1}{N!2\pi}E^{N(c_v+1)-1}\underbrace{\int_{-\infty}^{\infty}\mathrm{d}(kE)\exp(ikE)g^N(kE)}_{2\pi K} = \frac{K}{N!}E^{N(c_V+1)-1}$$

K is an integration constant. Finally, the microcanonical partition function is used to calculate the entropy.

$$\frac{S(E)}{k_{\text{B}}} = \ln(\mathcal{Z}_{\text{mc}}) = (N(c_V+1)-1)\ln(E) - N\ln(N) + N + \ln(K) \tag{3.55}$$

The expression $N!$ has been replaced by Sterling's formula $\ln(N!) = N\ln(N) - N + \mathcal{O}(ln(N))$. The inverse temperature is given by the derivative of the internal entropy with respect to energy. Hence, the internal inverse temperature reads

$$\frac{1}{T(E)} = \frac{\partial S}{\partial E} = \frac{(N(c_V + 1) - 1)}{E} = \frac{c_V + 1}{\langle e \rangle} - \mathcal{O}\left(\frac{1}{N}\right). \tag{3.56}$$

Figure 3.4 presents a temperature profile of a homopolymer melt. However, the temperature gradient was created, the internal and kinetic temperature coincide, excluded fluctuations. If energy is added to internal **DoF**s internal temperature immediately changes while the kinematic temperature follows with a delay according to relaxation from internal to external **DoF**s.

3.5.4 RNEMD simulation

The **eMC** scheme enables us to mimic energy transport properties of polymers. Therefore, strategies to measure thermal properties are discussed. To investigate thermal properties of the polymer melt, a constant heat flux is applied to the system. The system is divided into slabs of the size σ. Particles are organised by a box structure. Each box has the size σ^3. This size is given by the cut-off distance of non-bonded soft interaction. Thus, a particle in a specific box interacts with particles that are distributed to 26 surrounding boxes + 1 box containing the particle itself. Hence, this box structure is already there, each box is flagged if it is associated with the hot slab or cold slab, respectively. At the centre of the system a hot slab is considered. At the leftmost side the cold slab is considered, fig. 3.5. Now, an external flux will transport energy from the cold to the hot slab. Subsequently, polymers will compensate this unbalanced state. The balance emerges in form of a thermal profile in steady-state, i.e., it is a linear response of to the externally driven system. This strategy is known by the term **r**everse **n**onequilibrium **m**olecular **d**ynamics simulation (**RNEMD**) and was applied to particles' momenta first [65]. $\dot{q}$ represents the constant flux that is applied to the system.

$$\dot{q} = -D_T \frac{\mathrm{d}T}{\mathrm{d}x} = \text{const.} \tag{3.57}$$

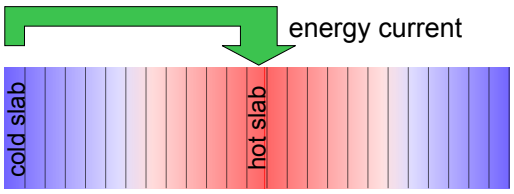

Figure 3.5 The system is a period box. This box is subdivided along the x axis into small slabs. The **RNEMD** strategy to applies an external thermal current to the system. At a constant rate, energy is moved from cold to hot slab that the system's response is a temperature profile in steady-state. A move can be created via treating particles' (i) internal energy (ii) external/kinetic energy. To get an impression of an temperature profile cf. fig. 3.4.

The flux is constant. Thus, eq. (3.57) is integrated. The integration leads to a linear temperature profile

$$\lim_{t\to\infty} T(x,t) = -\frac{D_T}{\dot{q}} \cdot x + T_0. \tag{3.58}$$

$T_0 = 1$ is the reference temperature at spatial position $x = 0$. Depending on the problem two different cases of transferring energy between cold and hot slab are considered.

Energy to internal DoFs The flux will act on particles' internal **DoF** - internal energy, e. Depending on the amount of energy, which has to be transported in a time interval Δt, small portions are equally subtracted from all particles' internal energies that belong to the cold slab. This energy is equally distributed to all particles' internal energies that belong to the hot slab. The maximum of energy that can be transported, is given by an interplay between (i) the maximum energy that can be subtracted by internal **DoF**s (ii) rapidity of internal thermal relaxation, videlicet the energy which has been taken out of particles' internal **DoF** has to be recovered by surrounding particles, [11].

Energy to external DoFs If the **eMC** routine is switched off, there is no coupling between internal and external **DoF**s. Hence, the energy flux has to be done by external **DoF**s. Again, the system is divided into slabs of size σ. The original **RNEMD** strategy proposed by Müller-Plathe is: search for the hottest particle in the cold slab and swap this particle with the coldest particle into the hot slab [65]. But this strategy causes a lot of fluctuations in the current itself such that a steady-state condition is not stable and fluctuates. For transferring of kinetic

energy from cold to the hot region the velocities of all particles that belong to the hot (cold) slab, are rescaled. This strategy enables the transport of exactly the amount of energy that is dictated by the flux.

3.6 Single chain in mean field

It was pointed out that the time and the length scale polymers show universal behaviour. In consequence this universal scale can be represented by a minimal set of parameters. Polymers are formed by monomers, which are connected via Gaussian bonds, and interact via a soft bonded potential. To observe dynamics induced by directed self assembly (**DSA**) one can formulate explicit equations of motion and solve them via an integration scheme or Velocity-Verlet, respectively. In the single chain in mean field (**SCMF**), pairwise non-bonded interactions are represented by a quasi-instantaneous field approximation [66]. In consequence, chains, i.e., monomers, exclusively interact via these quasi-instantaneous fields. Only local interactions accordingly, e.g., harmonic bonded potentials are taken into account explicitly. The advantage of the quasi-instantaneous field approximation is that the computationally intensive part of calculating the non-bonded pairwise interactions is replaced by a quasi-instantaneous field. Hence, the displacement of a polymer, i.e., segment, is done via Monte-Carlo scheme, smart Monte-Carlo scheme, respectively. The scalability and computational efficiency of this method comes into play, because the scheme only needs one global communication: update the density fields, which leads to a new quasi-instantaneous field approximation.

According to this thesis, the **SCMF** method has been used in two cases. Firstly, the framework allows to set up complex systems, e.g., star polymers quite accurately and helps to pre-equilibrate the systems before performing sustained simulations. Secondly, from collaboration with the department of chemical physics, University of Göttingen, we worked out a possible dependence of photoswitches (cis/trans azobenzene) on directed self assembly. Therefore we expanded the **SCMF** implementation, i.e., **SO**ft coarse-grained **M**onte-Carlo **A**cceleration [4], by introducing an additional scaling constant for the harmonic bond parameter [5]. This parameter can be interpreted to represent the influence of the cis/trans azobenzene photoswitches on level of a coarse-grained description, sec. 4.9.

[4] A complete description of the implementation and benchmarks for different architectures is available in [67].

[5] Newest version of the code is always available on Git-Lab `https://gitlab.com/InnocentBug/SOMA.git`, April 12, 2018.

4 Simulation results

In this chapter, results of the investigation of thermal properties of polymer melts are presented. They are obtained by coarse-grained molecular dynamic simulations performed with the **eMC** method. Simulated systems are comprised of structures of monomers, soft cubic crystals, homo-, diblock-, and star polymers. The dynamic and static characteristics of these structures are studied. Consequently, thermal properties in equilibrium, steady-state, and non-equilibrium conditions are investigated. In addition, phonon properties of a system with a low level of coarse-graining are studied. These systems are treated without an additional **DoF** internal energy, e, (without **eMC** thermostat). To observe a density of states, a soft fluid is quenched. In the quenched state, the Hessian matrix is computed and the corresponding eigenvalues are calculated. Finally, preliminary results on photo switches are presented. Photoswitches enable us to change the structural phase of a diblock copolymer melt and give rise to a control tactic of energy transport by controlling the systems' interfaces.

4.1 Parametrisation - energy Monte-Carlo

Coarse-grained parameter. **eMC** is a general method to simulate energy-transport phenomena. Therefore, a soft coarse-grained molecular dynamics simulation, which allows us to reproduce thermal properties of polymers, has been implemented. In a top-down approach, experimental values can be used to parametrise all values of the simulation. Representative for this technique is a minimal set of universal parameters to describe real system's behaviour: isothermal compressibility $K_{\text{iso}}N$ [1], invariant degree of polymerisation $\bar{\mathcal{N}} = (\rho b^3)^2 N$ (ρ is a number density, N

[1] to avoid confusion with thermal relaxation constant κ_{int}, we consistently changed the common notation $\kappa N = K_{\text{iso}}N$

number of segments [2]), averaged end-to-end distance R_e, and in case of polymer blends incompatibility, χN, is added [64]. At this point, it is worth to mention that simulation parameters typically depend on the temperature. Both, the isothermal compressibility $K_{iso}N$ and the incompatibility parameter χN are proportional to the inverse temperature. In consequence, the soft interaction v_{ij} also fits into a single temperature only. Hence, temperature differences are kept small.

Reduced units Simulations are performed in reduced units, because data types, e.g., floats, have a limited accuracy. The accuracy benefits from magnitudes of the order of 1. In consequence, we set the range σ of the non-bonded interactions equal to the statistical segment length, $\sigma = b$, and measure all length scales in these units, i.e., $\sigma = b = 1$. All energies are measured in units of the thermal energy at which the equilibrium properties of our coarse-grained model correspond to that of the underlying chemically realistic model, i.e., $\epsilon = k_B T = 1$ [11]. The time scale in the simulation is characterised by τ_{md}. In many cases, the time scale of a simulation τ_{md} is redefined in Rouse relaxation times, $\tau_r = \frac{\xi N^2 b^2}{3\pi^2 k_B T} = \frac{N b^2}{3\pi^2 D}$. [59]. It corresponds to the longest relaxation time of a polymer and permits an invariant connection between systems that have been discretised differently with respect to their chain discretisation. The time scale of an experiment is determined by the diffusion/relaxation time of a polymer, $\langle \vec{x}^2 \rangle = 6Dt$, and the diffusion constant of an experiment is mapped on the time scale of the simulation, sec. 4.3.1.

Internal DoF **eMC** method adopts the idea of **eDPD** by reintroducing degrees of freedom that have been integrated out to a coarse-graining procedure by one additional **DoF**, i.e., internal energy. This internal energy, e, is determined by a top-down approach, which equally distributes specific heat capacity of a real system of polymers to a coarse-grained one. To describe the relation between energy and entropy, we use the universal form $s(e) = c_V \ln(e)$ from sec. 3.4. In case of high coarse-graining, reducing the number of segments $N' \to N/2$ implies an increase of specific heat capacity $c_v' \to 2c_v$. Internal energies interact and exchange energy between each other. This is captured by an internal thermal relaxation constant, κ_{int}. Investigating the real time of the internal **DoF**s in the simulation is quite challenging. Especially in our case, we deal with two time scales: a time scale of the integration step according to the Velocity-Verlet scheme, τ_{md}, and the time

[2] A typical order of magnitude for the invariant degree of polymerisation is 10^4 or $\sqrt{N} \approx 64$ respectively.

increment we apply for calling the **eMC** update. If it is not specified in a different way, we set all time steps to the same increment. This means we call the **eMC** routine once in each integration step, i.e., update of momenta and positions for each pair of particles that interacts in a specific interaction range σ. The real time scale (to compare to experiments) will be observed by the diffusion, which is characterised by Rouse dynamics of a polymer, in the bulk, sec. 4.3.1.

Energy conservation First simulations will cover static properties. To validate the implementation, it is useful to study all kind of energies. By definition, the **eMC** method has been constructed so that energy is conserved by a local **eMC** move. In consequence, the change of the system's energy is influenced by the choice of the microcanonical integration scheme: Velocity-Verlet integration. The integration step is $\mathrm{d}t = 0.005$. Hence, the Velocity-Verlet scheme practically ensures an energy-conserving system. Although typical simulation times are 10000 τ_{md}, global energy only changes by a fraction of 10^{-6}, which is covered by the uncertainty induced by the data types representing momenta and spatial positions as well as finite $\mathrm{d}t$ in the Velocity-Verlet scheme.

4.2 Invariant polymer melt - rescaling of properties

Thermal properties that are observed by simulation, should be independent of the degree of coarse-graining. In analogy to the universal equilibrium statistics of the Gaussian chain model, the universal conformational motion, i.e., Rouse dynamics, the internal energy of a coarse-grained segment, and its internal entropy converge towards a universal form for highly coarse-grained models. Hence, a polymer melt composed of homopolymers exhibits the same thermal behaviour independent from N - the explicit discretisation into chain segments at a fixed invariant degree of polymerisation $\bar{\mathcal{N}}$.

In order to investigate how the model parameter behave under coarse-graining, we assume that the specific heat capacity of the system is dominated by the internal **DoF**s. In consequence, specific heat capacities of the explicit **DoF**s play a sub-dominant role. The averaged end-to-end distance R_e of a chain defines an invariant length scale in the system. The energy that is transported in one step $\mathrm{d}t$ calculates to: rnecurrent$A$ $\mathrm{d}t$ [3]. The cross-sectional area A is defined in units of R_e^2 such that

[3] We chose the expression *rnecurrent* to be consistent with the input parameter of the implemen-

Discretisation:	N=64	N=32
$\sigma = b$	$\sigma_{64} = b_{64} = R_e/\sqrt{N_{64}}$	$\sigma_{32} = b_{32} = b_{64}\sqrt{2}$
c_V	$c_{V\,64}$	$c_{V\,32} = 2c_{V\,64}$
$\rho_0 R_e^3$	$\rho_{64} = \frac{N_{64} n_{\text{poly}}}{V}$	$\rho_{32} = \frac{\rho_{64}}{2}$
$\rho\sigma^3$	$\rho_{64}\sigma_{64}^3 = \rho_{64} b_{64}^3 = \frac{\sqrt{\bar{N}}}{\sqrt{N_{64}}}$	$\rho_{32}\sigma_{32}^3 = \sqrt{2}\rho_{64} b_{64}^3$
$\kappa_{\text{int}} \sim \lambda T^2 \frac{\sigma}{(\rho\sigma^3)^2}$	$\kappa_{\text{int}\,64} \sim \lambda T^2 \frac{R_e}{\sqrt{\bar{N}}}$	$\kappa^{\text{int}\,32} \sim \frac{\kappa_{int\,64}}{\sqrt{2}}$

Table 4.1 A coarse-grained system of homopolymers is systematically reduced from $N = 64$ to $N = 32$ segments. Hence, the system is invariant under polymers' end-to-end distance R_e, statistical segment length, density, and internal thermal relaxation are rescaled. V represents the total volume in units of R_e^3.

the same energy is transported to the same invariant area.

Under these requirements, we can determine all parameters through a top-down approach leaving the length scale R_e and global energy invariant. One coarsening step $k = 1$ follows an iterative strategy by reducing the explicit discretisation of a chain from $N' = N/2$. In the following, we discuss the rescaling of all relevant parameters. The internal specific heat increases by a factor of 2, because two internal **DoF**s are lumped to one new internal DoF. The scaling of the internal thermal relaxation constant κ_{int} is estimated by the energy transfer across a plane of area A. The energy transport per **eMC** step is given by the number of particle pairs that straddle the plane, $\rho A\sigma \cdot \rho\sigma^3$, and the mean energy transfer, $\kappa_{\text{int}}\Delta t\frac{\nabla T\sigma}{T^2}$, by a single pair [11, 45]. The corresponding heat current, $j \sim \rho^2\sigma^4\kappa_{\text{int}}\frac{\nabla T\sigma}{T^2}$, allows a comparison with Fourier's law, eq. (2.14), $j = \lambda\nabla T$. Hence, one obtains the estimate $\kappa_{\text{int}} \sim \frac{\lambda\sigma T^2}{(\rho\sigma^3)^2}$ [11], cf. sec. 4.3.2. In consequence, the internal thermal relaxation constant κ_{int} is rescaled by $\sqrt{2}$.

Table 4.1 relates parameters of two systems discretised in N_{32} and N_{64} polymers. In order to keep physical properties invariant, the statistical segment length, $b = R_e/\sqrt{N_{64}}$, and the interaction range, σ_{64}, increase by a factor $\sqrt{2}$ and, in turn, the rate of internal energy transfer, κ_{int}^{64}, decreases by a factor of $\sqrt{2}$ (in the limit of high degree of coarse-graining). To verify this scaling procedure, a system of homopolymers is systematically reduced from $N = 64$ to $N = 16$ segments, with two successive steps $N_{64} \to N_{32} \to N_{16}$. The system size is invariant in units of R_e. The invariant degree of polymerisation, $\sqrt{\bar{N}} \sim 40$, is constant, too. Figure 4.1 shows the temperature profile of two equal systems represented on different

tation: [rnecurrent] $= \left[\frac{k_B T}{\tau_{\text{md}}\sigma^2}\right]$.

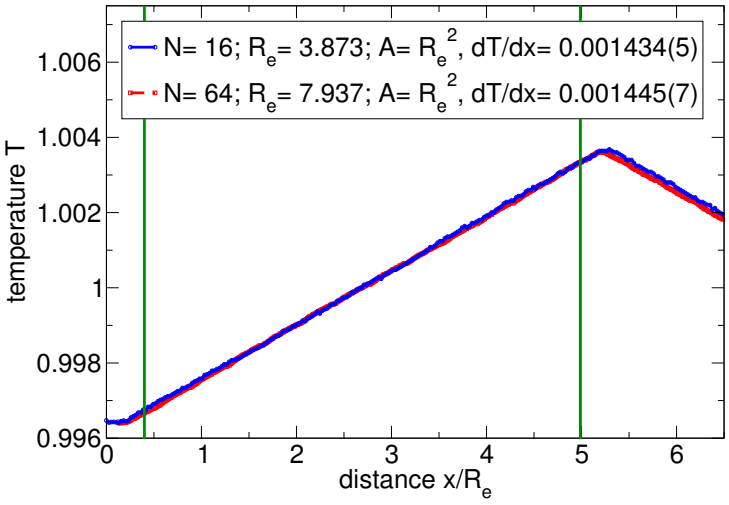

Figure 4.1 Temperature profile of two systems represented on different levels of coarse-graining $N = 64, 16$, with $\sqrt{\mathcal{N}} \sim 40$. The slope of the temperature profile emerges through the application of the **RNEMD** method to the internal **DoFs**. Parameters are compiled in tab. 4.2. In between the green vertical lines, the slopes agree to 99 percent.

levels of coarse-graining $N = 64, 16$. Parameters of the simulations are completed in table 4.2. The current to create a steady-state condition is realised via a **RNEMD** strategy, which is applied to the internal **DoF**s, cf. sec. 3.5.4. The cross-section in both systems is about $A \sim R_e^2$ [4].

Discussion The gradients of the two realisations of the same system agree with each other. Fitting a linear function to the steady-state temperature profile in the area that is enclosed by the two vertical green lines, results in a linear slope of temperature, which agrees to 99 %. This result affirms that **eMC** allows for an invariant representation of a polymer melt. Although, the slope in both systems agrees, fig. 4.1, there is a marginal difference in both temperature profiles, which has been compensated. Technically, the thickness of the *hot* and *cold* slab is set to σ. Hence, in units of R_e, the slabs have a different size, which can be observed in the fig. 4.1, too. To compensate for this effect, the system's width is approximately

[4] Technically, the implementation usually calculates the explicit energy, which is transported in a step t_{md}, through the cross-section area in units of σ. Hence, we modified the routine *rne(CONF *conf)* such that the calculation of cross-section area and amount of energy that is transported is in units of R_e.

Discretisation:	N=64	N=16	rescaling for k=2
R_e/σ	$R_{e,64}\sigma^{-1} = 7.937$	$R_{e,16}\sigma^{-1} = 3.873$	~ 2
c_V/k_B	10000	40000	4
V/R_e	$\sim 10 \times 1 \times 1$	$\sim 10 \times 1 \times 1$	const.
$\rho_0\sigma^3$	5.13	10.275	~ 2
ρR_e^3	~ 600	~ 2500	~ 4
κ^int	1000000	50000	$\frac{1}{2}$
Nn_{poly}	26304	6576	4
$\frac{(\mathrm{rnecurrent})\tau_\mathrm{md}\sigma^2}{k_\mathrm{B}T}$	200	200	const.
eMC update range	σ	σ	const.

Table 4.2 A coarse-grained system of homopolymers, with invariant degree of polymerisation $\sqrt{\mathcal{N}} \sim 40$, is systematically reduced from $N = 64$ to $N = 16$ segments. The polymer's end-to-end distance $R_e = b\sqrt{N-1}$ remains invariant. Statistical segment length σ, density ρ, specific heat capacity c_V, and internal thermal relaxation $\kappa^\mathrm{int}$are rescaled.

10 R_e only. Hence, the system size in x-direction was chosen to be $L_{N_{64},x}\sigma^{-1} = 80$, $L_{N_{16},x}\sigma^{-1} = 40$, because the different size of the slabs in units of R_e has to be compensated such that $\frac{(L_{N_{64},x}-2\sigma)}{R_{e,64}} \approx \frac{(L_{N_{16},x}-2\sigma)}{R_{e,16}} \approx 9.82R_e$. Here, $R_{e,64}$ and $R_{e,16}\sigma^{-1}$ are in units of σ. Hence, the temperature profile is symmetric, and the effective distance over which energy is transported between hot and cold slab is about 4.92 R_e. The fit area indicated by the green vertical lines is even smaller in order to leave out the effect of the external current. In the given rescaling scheme, the time scale is left invariant, because the **eMC** routine transports the same amount of energy in the same discrete time interval Δt. Here, we converge towards the universal equilibrium statistics. In fact, in the rescaling of parameters, the time scale has not been taken into account yet. In consequence, the time scale has to be redefined by diffusion constants obtained by the mean-squared displacement, which agrees with a universal conformational motion of a polymer, i.e., the thermal conductivity remains invariant but not the Lewis number (ratio of thermal and mass diffusivity).

4.3 Homopolymers - eMC

In the first section, we gave an overview of the parameters of **eMC** and showed that **eMC** can reproduce temperature profiles that are invariant under the explicit discretisation of the systems. Firstly, we will pick up the discussion on definition of a time scale following the idea of an universal conformational motion of a polymer. Secondly, thermal properties, e.g., macroscopic thermal conductivity, of a homopolymer melt are investigated systematically in steady-state by studying the **RNEMD** strategy, time-step dependencies, internal relaxation parameters, and length of a homopolymer.

4.3.1 Kinematic diffusion constant

A soft model of polymers has universal characteristics, which are embraced by a minimal set of parameters. This universal characteristics also corresponds to a universal time scale. This time scale is typically defined by kinematic diffusion. The mean-squared displacement of the polymers' centre of mass, g_3, characterises the diffusion via the relation $\langle \vec{x}^2 \rangle = 6Dt_{\mathrm{md}}$. D represents the self-diffusion coefficient. It remains the question whether the kinetic diffusion is influenced by **eMC** scheme.

The system is comprised of soft potentials. Hence, the diffusive characteristics are mainly driven by the friction induced by **eMC**, which destroys correlations of the velocities. However, we want to check the influence of the internal thermal relaxation, κ_{int}, on kinematic diffusion. The scheme is tested on this criterion, because it is common to distinguish between different internal thermal relaxations, κ_{int}. Indeed, diffusion of external **DoF**s should be independent from any of these influences. The probability distribution of the thermal noise δq, eq. (3.28), is scaled by κ_{int}, which could induce higher fluctuations in the internal DoFs. In consequence, the probability distribution of parallel momenta could change, because it is weighted by its local temperature T_{loc}.

The mean squared displacement of polymers, g_3, is measured for identical systems with different internal thermal relaxation constants. Figure 4.2 shows g_3 divided by time, t, for diverse internal relaxation constants, κ_{int}. Dividing g_3 by t enables to read the diffusion constant, D, directly. The trend of this figure reveals that internal thermal relaxation constant does not have a significant influence on the diffusive properties of the system. The scaling behaviour coincides Rouse like behaviour, too. There is (i) a ballistic regime, which is controlled by the local interactions that

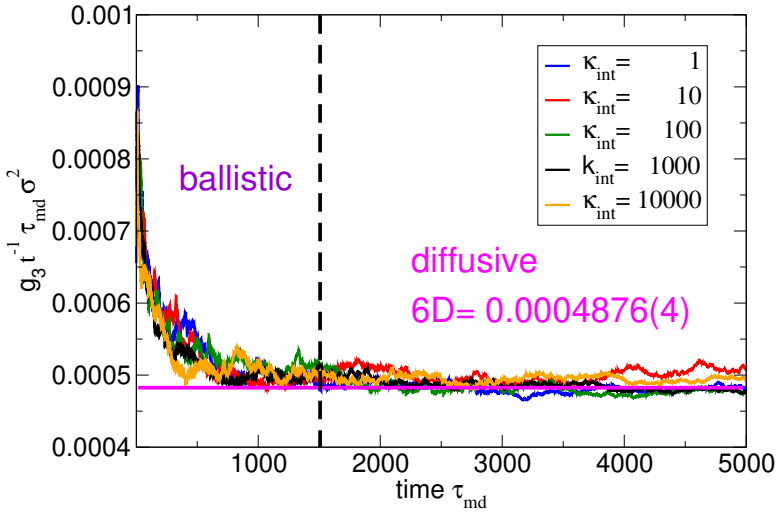

Figure 4.2 Displacement of polymers' centre of mass as a function of internal thermal relaxation, κ_{int}, divided by time t. The diffusion constant can be read from the graph $D\sigma^2\tau_{\text{md}}^{-1} = 0.00004879 \pm 4 \cdot 10^{-7}$ and is on average independent from κ_{int}. The system is comprised of homopolymers, discretised by $N = 32$. Partial re-equilibration constant is set to $\alpha = 0.1$. The system's mean density is $\rho_0\sigma^{-3} = 5.686$, $nN = 152832$.

scales with $\propto t^2$, (ii) a diffusive regime that scales with $\propto t$. This diffusive regime yields an invariant time scale, the Rouse time,

$$\tau_{\text{Rouse}} = \frac{Nb^2}{3\pi^3 D} = (13300 \pm 10)\ \tau_{\text{md}},$$

which is determined by the time that is needed to diffuse the distance of R_e. This time is calculated by the average over all trajectories which permits reasonable statistics. With common values for polymers (PMMA) $D_{\text{real}} \frac{\text{sec}}{\text{nm}^2} \approx 10$, $R_e/\text{nm} \approx 50$, the characteristic time scale can be estimated as $\tau \approx \frac{R_e^2}{3\pi^2 D\ \text{sec.}} \approx 8.44$, which relates the time scale between experiment and simulation. The Rouse time, which was estimated by the linear diffusion, can be used to connect the time scale of the simulation to $\tau_{\text{md}}/\text{sec} \approx 0.00114$. Hence, if the time scale of microcanonical integration scheme and **eMC** update is chosen equally, the time scale of internal thermal relaxation constant can be related as well with a real time scale given in unit of seconds. The Peters thermostat was introduced in sec. 3.2.2. We pointed out that this is a gentle way to keep correlations by usage of an additional weighting constant α. In the implementation we used the expression $\alpha = (1 - \alpha_{\text{couple}})$ that

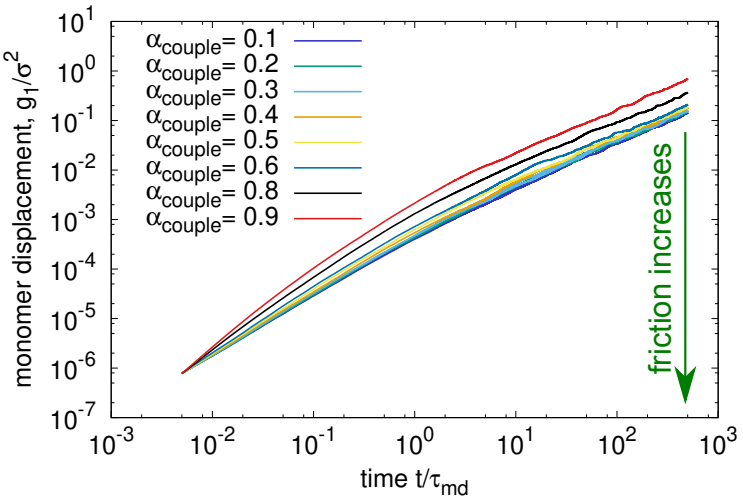

Figure 4.3 Displacement of monomers as a function of partial relaxation α of the parallel momenta in a melt of homopolymers, discretised by $N = 32$. Thermal relaxation constant is set to $\kappa_{\text{int}} = \frac{\kappa_{\max}}{10}$. The system's mean density is $\rho_0\sigma^{-3} = 5.686$, $nN = 152832$. A high α induces a high weighting of the old parallel momenta, which increases correlations.

α_{couple} controls the weight between the old and new drawn momentum. Thus, the new parallel momentum of two particles is modified by

$$p_{\parallel\text{new}} = \alpha_{\text{couple}} p_{\parallel\text{ old}} + \sqrt{(1-\alpha_{\text{couple}}^2)}\Delta p_{\parallel\text{new}}.$$

Here, $\Delta p_{\parallel\text{new}}$ is drawn from the Gaussian distribution $P_{T_{\text{old}}^{\text{loc}}}(\Delta p_{\parallel\text{new}})$, cf. eq. (3.19). Fig. 4.3 demonstrates the influence of α_{couple} on the system's diffusive behaviour. Considering the Rouse model and the diffusion of a single monomer, one observes the sub-diffusive characteristic, which is $\propto \sqrt{\frac{12 k_{\text{B}} T b^2 t}{\pi\xi}} \propto \sqrt{t}$ [59]. However, the diffusion constant is related to the **VAC** function $D = \frac{1}{3}\int_0^\infty \langle v_i(0) v_t(t)\rangle \mathrm{d}t$. If α_{couple} equals 0 the two successive velocities are uncorrelated[5]. If the weighting constant $\alpha_{\text{couple}} \to 1$ the correlation becomes high, too. This high correlation is connected with low friction, which results in a faster diffusion for $\alpha_{\text{couple}} = 0.9$, cf. fig. 4.3. All the following simulations are performed with a value $\alpha_{\text{couple}} = 0.1$, which means the system has a high friction but the old momenta are partially included. Additionally, the influence of the number of **eMC** calls at fixed time step and for different time

[5] In the implementation we set the input parameter $\alpha_{\text{couple}} = 1 - \alpha$. Hence Peters thermostat falls back to Lowe-Andersen thermostat for the value $\alpha_{\text{couple}} = 0$

steps has been tested, cf. appx. 6.5, appx. 6.4. As a side note, it should be mentioned that, if a **DoS** is determined, any kind of thermostats are switched off.

4.3.2 Thermal properties in steady-state

Thermal properties of a system are investigated by the **RNEMD** method. The method is explained in sec. 3.5.4. In short, during **RNEMD** simulations, we divide the system into small slabs along the long x-direction. In the leftmost slab – *cold* slab – we subtract a small portion of the internal energy, e_i, from each particle in each integration time-step, Δt. The energy is subtracted from the internal DoF, e_i, rather than from the kinetic energy, because the specific heat of the internal **DoF** is larger than that of the momenta and also dominates a system's thermal properties. Energy is added to the internal energies of particles in the *hot* slab, which is situated a distance$L_x/2$ away, sec. 3.5.4. This outer energy flux, j, is compensated by an energy flux through the system, and the concomitant temperature profile is monitored. Practically, some limiting cases of this strategy have to be considered.

- The number density of particles in the involved, hot and cold, slabs has to be large enough in order to include the transported energy properly.
- The density is influenced by the local temperature. In consequence, high temperature gradients can change the local densities that are indirectly related to the transport properties, too. In the worst case, this would result in non-linear steady-state conditions.
- If the temperature in the hot slab becomes too high, the density reduces. Hence, the mean free path of the hot particles increases and the number of particles in the hot slab decreases dramatically.
- If the rne-current implies a transported energy that is higher than the internal energies can take, **RNEMD** scheme will stop with an error output, i.e., the maximum internal energy is determined by the sum of all internal energies in a slab, so that a current, which is above the maximum value, fails.

In order to avoid this critical cases we restrict **RNEMD** to currents, which are an order of magnitude smaller than the specific heat capacity of a single particle. This yields an uncritical temperature difference, which also abates the argument that parametrisation of the potentials (external degrees of freedom) depends on the local temperature.

RNEMD - dependence of temperature profile and applied current

In this part, we investigate the follow question: does the applied current have an influence on the resulting thermal conductivity? Hence, we take a small system, comprised of homopolymers - discretisation $N = 16$. The system size is $L/\sigma^3 = 56\times6\times6$, averaged density is $\rho\sigma^3 \approx 12.7$, the total number of particles is $nN = 25600$, and the local non-bonded interaction $v_{\mathrm{ij}} = 0.5$. The internal specific heat capacity is set to $c_V/k_{\mathrm{B}} = 10000$, and the internal thermal relaxation is $\frac{\kappa^{\mathrm{int}}\tau_{\mathrm{md}}}{k_{\mathrm{B}}T^2} = 500$. The time-step of the **eMC** update and Velocity-Verlet algorithm will be $\mathrm{d}t = 0.005$. The resulting maximal internal thermal relaxation, which leads to an instantaneous thermal relaxation of two internal degrees of freedom, calculates to $\frac{\kappa^{\mathrm{int}}_{\mathrm{max}}\tau_{\mathrm{md}}}{k_{\mathrm{B}}T^2} = 1\cdot10^6$. The energy transported in each step is $A\cdot\mathrm{d}t\cdot(\mathrm{rnecurrent})$. A denotes the cross-section area $A = L_y \cdot L_z$. Using Fourier's law, eq. (2.14), we can determine the macroscopic thermal conductivity, λ, of the system by the gradient of the temperature profile in steady-state and the applied current.

$$\frac{\lambda\sigma\tau_{md}}{k_{\mathrm{B}}} = \frac{(\mathrm{rnecurrent})}{\partial_x T} \tag{4.1}$$

Since the macroscopic thermal conductivity has to be invariant when changing the applied **RNEMD** current the slope of the temperature profile, $\partial_x T$, has to change. Hence, we apply different **RNEMD** energy currents: $\frac{\mathrm{rnecurrent}\tau_{\mathrm{md}}\sigma^2}{k_{\mathrm{B}}T} = 100$, 200, 300 and 400, and measure the slope of the temperature profile in a steady-state condition. After the slope of the temperature does not change anymore, profiles have been averaged over a period of $t = 5000\ \tau_{md}$ with increments of $\Delta t = 10\tau_{\mathrm{md}}$. The results are compiled in tab. 4.3. These values allow the conclusion that the profile does not depend on the applied current. Errors of the gradients result from fit procedures. The form of this formula implies that the macroscopic thermal conductivity is invariant according to the choice of the applied current, because a higher current is compensated by a higher thermal gradient, i.e., system is in a linear-response regime.

This allows us to optimise the measurement of thermal conductivities by limiting the maximal slope of the temperature profile in steady-state. Hence, the temperature differences can be kept small so that the interaction parameters of explicit **DoF**s are in a range, where effects of temperature changes can be neglected. Practically, it has been shown that, if the transported energy is two orders of magnitudes smaller than the particle's internal energy, the equilibration to a steady-state condition will be

$\frac{\text{rnecurrent}\cdot\tau_{\text{md}}\sigma^2}{k_{\text{B}}T}$	100	200	300	400
$\frac{\partial_x T\cdot\sigma}{T}$	0.00294(6)	0.00583(2)	0.00873(3)	0.01146(6)
$\frac{\lambda\sigma\tau_{md}}{k_{\text{B}}}$	34013(6)	34305(7)	34364 (12)	34904(18)

Table 4.3 resulting macroscopic thermal conductivity of a polymer melt is invariant according to the choice of applied **RNEMD** current. Overall parameters are $N = 16$, $L/\sigma^3 = 56 \times 6 \times 6$, $c_V/k_{\text{B}} = 10000$, $\rho\sigma^3 \approx 12.7$, $v_{\text{ij}} = 0.5$. Weighted average $\langle\lambda\rangle_{\text{rnecurrent}} = 34204 \pm 4$.

uncomplicated. Nevertheless, if one considers a too high current, the equilibration to a linear stable steady-state condition will not be possible in a passable computational time.

RNEMD - Time-step dependencies

Next we investigate transport phenomena in polymer melts. It is important to make sure that the observed properties are independent from the choice of the time-step increment. Hence, the thermal conductivity of the system primarily is independent of the discretisation of our time scale. The time scale is dictated by the microcanonical integration scheme. We already mentioned that there are two different time scales: a microcanonical one defined by diffusion and a thermal one given by the internal relaxation parameter κ_{int}. These time scales are linked together by using the same increment of calling the Velocity-Verlet integration scheme and the **eMC** update, respectively. The proposed internal energy does not depend on the discrete time-step, because the deterministic thermal relaxation linearly scales with $\mathrm{d}t$

$$\kappa_{\text{int}} \left(\frac{\partial s_{\text{i old}}}{\partial e_{\text{i old}}} - \frac{\partial s_{\text{j old}}}{\partial e_{\text{j old}}} \right) \mathrm{d}t. \tag{4.2}$$

Fluctuations of the thermal noise depend on the probability function that is normalised by the local temperature and the time-step $\mathrm{d}t$, which also keeps the system invariant, eq. (3.28), eq. (3.31). Fig. 4.4 shows temperature profiles, created by the **RNEMD** simulation, cf. sec. 3.5.4. The discretisation varies between $\mathrm{d}t = 0.001\ \tau_{\text{md}}$ and $\mathrm{d}t = 0.009\ \tau_{\text{md}}$. The current is set to $\frac{\text{rnecurrent}\tau_{\text{md}}\sigma^2}{k_{\text{B}}T} = 100$. The specific heat capacity that determines the internal entropy is set to $c_V/k_{\text{B}} = 10000$. The internal thermal relaxation is $\frac{\kappa_{\text{int}}\tau_{\text{md}}}{k_{\text{B}}T^2} = 5000$. The invariant degree of polymerisation is $\bar{\mathcal{N}} = 3200$, with an average density $\rho b^3 = \rho\sigma^3 = 10$. Due to fluctuations, the

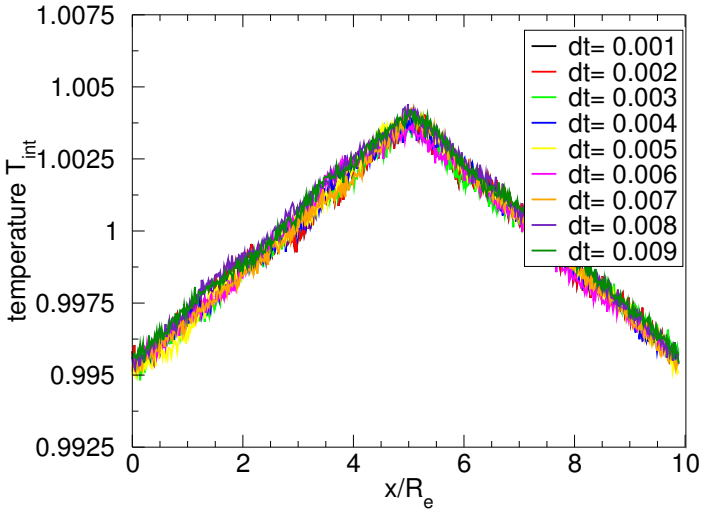

Figure 4.4 Invariant temperature profiles - non-averaged - in steady-state created by a constant current: $\frac{\text{rnecurrent}\tau_{\text{md}}\sigma^2}{k_{\text{B}}T} = 100$. Eq. (4.2) ensures that the gradient is invariant under time discretisation. The discretisation varies between $\text{d}t = 0.001 - 0.009\ \tau_{\text{md}}$. Internal specific heat capacity is set to $c_V/k_{\text{B}} = 10000$. Internal thermal relaxation, κ_{int}, is set to $\frac{\kappa_{\text{int}}\tau_{\text{md}}}{k_{\text{B}}T^2} = 5000$. Invariant degree of polymerisation $\bar{\mathcal{N}}$ with average number density $\rho\sigma^3 = 10$.

temperature profiles do not match completely - when averaged, they are congruent. The total energies in initial state differ, because the particles' positions are drawn randomly so that the potential energy differs, too. The **eMC** scheme conserves the energy so that this difference cannot be compensated. The gradients will be the same, but there will be a small offset in the temperature, too.

Discussion Fig. 4.4 permits the conclusion that **eMC** can mimic energy transport independent from the time discretisation. In consequence, the transport properties implemented by **eMC** can be decoupled from the microcanonical integration scheme efficiently. Hence, the integration step of the Velocity-Verlet scheme can be fixed to a value that satisfies that energy is conserved (limited by global error of the integration scheme $\mathcal{O}(\text{d}t^4)$), and that the computational expensive eMC update is controlled by a different time increment, which is larger, i.e., $\frac{\text{d}r}{\tau_{\text{md}}} = 0.005$ and $\text{d}\tau_{\text{eMC}} = 0.01$. In the best case scenario, one gets about two orders of magnitude in time performance, by decoupling the integration scheme, compared to common values that have been used by **eDPD** simulations $\text{d}t \sim 0.0001\tau_{\text{md}}$ [41].

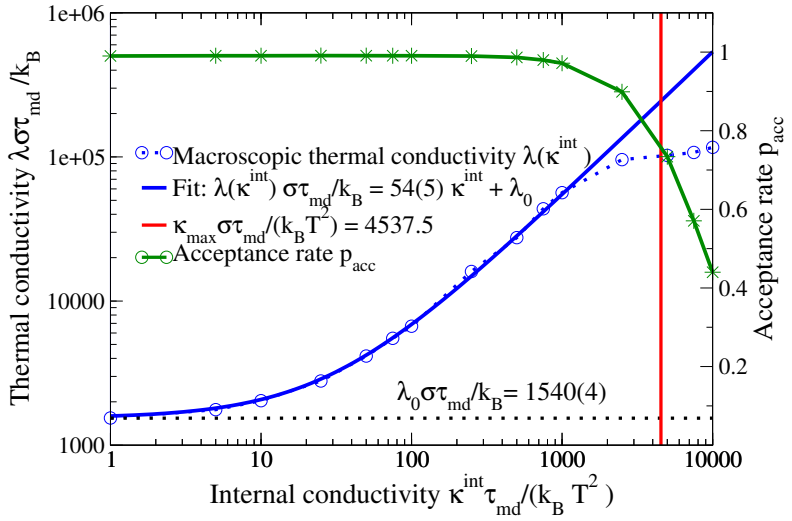

Figure 4.5 Macroscopic thermal conductivity as function of internal conductivity, $\kappa_{\rm int}$, as obtained by **RNEMD** simulations. The maximal conductivity $\kappa_{\rm int}^{\rm max}$ according to Eq. (3.38) is indicated by a red, vertical line. The green curve represents the acceptance rate of **eMC** moves, which sharply declines beyond $\kappa_{\rm int}^{\rm max}$ [11].

eMC - scaling of internal thermal relaxation $\kappa_{\rm int}$

In the previous sections, we gave an overview of the scaling of properties of **eMC**. Now we investigate the dependence of the macroscopic thermal conductivity as a function of the internal thermal relaxation $\kappa_{\rm int}$, cf. eq.(3.31). In the example, we use a chain discretisation, $N = 32$, a number density of coarse-grained segments, $\rho\sigma^3 = 11.32$, and system size $60\sigma \times (6\sigma)^2$. Periodic boundary conditions are applied in all directions. The specific heat is $c_V/k_{\rm B} = 45.375$, and the compressibility is $\kappa N = 50$. The velocity-Verlet integrator uses a time-step of $\Delta t/\tau_{\rm MD} = 0.005$. To drive the systems to a steady-state condition, we apply the **RNEMD** strategy to internal **DoF**s. From the slope of the temperature profile, we determine the macroscopic heat conductivity according to Fourier's law, (2.14), again: $\lambda = \frac{j}{\partial T/\partial x}$.

Fig. 4.5 presents the dimensionless thermal conductivity $\frac{\lambda\sigma\tau_{\rm md}}{k_{\rm B}}$ as a function of the normalised internal heat conductivity, $\frac{\kappa_{\rm int}\tau_{\rm md}}{k_{\rm B}T^2}$. In the limit $\frac{\kappa_{\rm int}\tau_{\rm md}}{k_{\rm B}T^2} = 0$, the energy is solely transferred via the particles' momenta and coordinates, and we find the value $\frac{\lambda_0\sigma\tau_{\rm md}}{k_{\rm B}} = 1540(4)$. Heat transfer involves two processes: a heat conduction (heat diffusion) and heat advection (heat transfer by bulk fluid flow, e.g., along the x-axis). The thermal relaxation between two interacting particles is mainly driven by the

internal **DoF**s' internal relaxation constants. Hence, the contribution of external **DoF**s to the energy transport is small compared to the direct exchange of energy between the internal **DoF**s. Thus, we study the dependence of the macroscopic thermal conductivity on the internal conductivity, κ_{int}. For intermediate values of κ^{int}, the thermal conductivity is well described by a linear relation,

$$\lambda(\kappa_{\text{int}})\frac{\sigma\tau_{\text{md}}}{k_{\text{B}}} = \frac{\lambda_0\sigma\tau_{\text{md}}}{k_{\text{B}}} + (54 \pm 5)\frac{\kappa_{\text{int}}\tau_{\text{md}}}{k_{\text{B}}T^2}. \tag{4.3}$$

Discussion To provide an analytical order-of-magnitude estimate of the macroscopic thermal conductivity, λ, we follow Mackie, Bonet Avalos and Navas [45], and estimate the energy transfer across a plane of area A. The energy transport per **eMC** step is given by the number of particle pairs that straddle the plane [6], $\rho A\sigma \cdot \rho\sigma^3$, and the mean energy transfer, $\kappa_{\text{int}}\Delta t\frac{\nabla T\sigma}{T^2}$, by a single pair [11]. The corresponding heat current scales like $j \sim \rho^2\sigma^4\kappa_{\text{int}}\frac{\nabla T\sigma}{T^2}$. In comparison with Fourier's law, eq. (2.14), $j = \lambda\nabla T$, one obtains the estimate $\kappa_{\text{int}} \sim \frac{\lambda\sigma T^2}{(\rho\sigma^3)^2}$. This order-of-magnitude estimate gratifyingly agrees with the slope found by the linear relation [11].

For large values of κ_{int}, we observe deviations from the linear relation, i.e., the macroscopic thermal conductivity increases slower and the acceptance rate, p_{acc}, of the proper **eMC** moves decreases. The deviations become significant around $\frac{\kappa_{\text{int}}^{\max}\tau_{\text{MD}}}{k_{\text{B}}T^2} \approx \frac{c_v}{2k_{\text{B}}}\frac{\tau_{\text{MD}}}{\Delta t} = 4537.5$. A simple strategy to overcome this limitation and increase λ consists in reducing the time-step Δt or in decoupling the time scales of the Velocity-Verlet integration and the **eMC** scheme, i.e., performing multiple **eMC** moves for one Velocity-Verlet integration step. To connect the macroscopic thermal conductivity to experiments, we use the value $\lambda = 0.18\text{W/mK}$ (PMMA) for the experimental heat conductivity, and obtain $\frac{\kappa_{\text{int}}\Delta t}{k_{\text{B}}T^2} \sim \frac{\lambda}{k_{\text{B}}}\frac{\sigma\Delta t}{(\rho\sigma^3)^2} = \frac{\lambda}{k_{\text{B}}}\frac{b_0^3}{D_0}\frac{g^{3/2}}{3\pi^2\eta^2}\frac{\Delta t}{\tau} \sim 10^7 g^{3/2}\frac{\Delta t}{\tau}$ for the dimensionless quantity. Thus, the larger the degree g of coarse-graining, the larger κ_{int} has to be. This value has to be contrasted with the limit value, $\frac{\kappa_{\text{int}}^{\max}\Delta t}{k_{\text{B}}T^2} \approx \frac{c_0}{2k_{\text{B}}}g$. Since the thermal diffusivity D_T and the heat conductivity λ are related via $D_T = \frac{\lambda}{c_V\rho}$, we obtain, for the ratio between thermal and mass diffusivity, the Lewis number $\text{Le} = \frac{D_T}{D} \leq \frac{\rho\sigma^3}{2}\frac{\sigma^2}{D\Delta t}$, i.e., large densities and small time intervals between proper **eMC** steps give rise to large Lewis numbers that are characteristic for polymer materials [11].

[6] The temperature gradient $\partial_x T$, is discretised to $\frac{\Delta T}{\Delta x}$ and the deterministic amount of energy that is transported per particle per time $\mathrm{d}t$, $\kappa_{\text{int}}\left(\frac{1}{T_1} - \frac{1}{T_2}\right)$ is rewritten into a temperature gradient $\frac{\Delta T}{T^2} = \frac{\Delta x}{T^2}\left(\frac{\Delta T}{\Delta x}\right)$.

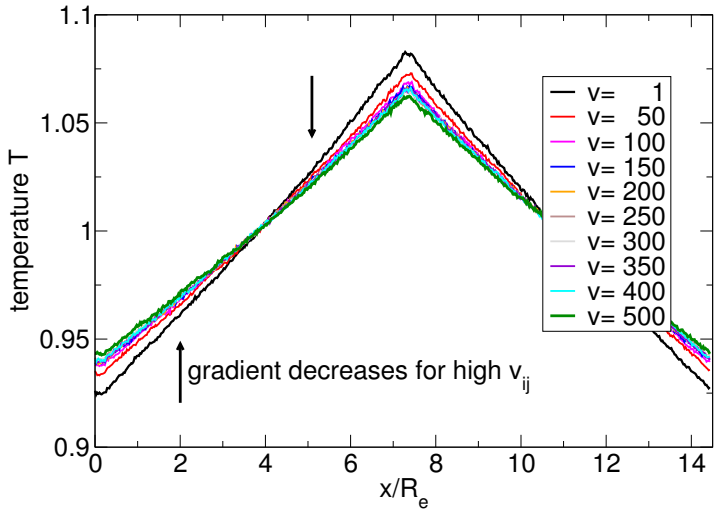

Figure 4.6 Temperature profiles in steady-state depend on the soft interaction parameter v_{ij}(cf. eq. 3.52). Macroscopic thermal conductivity increases for higher v_{ij}. Polymer segments are $N = 16$. Box dimensions are $L/\sigma^3 = 56 \times 6 \times 6$. Internal specific heat per particle is $c_V = 10000$. Number density is $\rho\sigma^3 \approx 12.7$, and the **RNEMD** current is $\frac{\mathrm{rnecurrent}\tau_{\mathrm{md}}\sigma^2}{k_{\mathrm{B}}T} = 200$.

Macroscopic thermal conductivity and isothermal compressibility

Performing **eMC** simulations, the main part of a system's energy is given by the internal **DoF**. Hence, the macroscopic thermal conductivity is dominated by the scaling of the internal thermal relaxation κ_{int}. Nevertheless the explicit **DoF**, i.e., positions, momenta influence thermal properties, matters.

Hence, we investigate whether the external **DoF**s have an influence on the slope of the temperature profile in steady-state, i.e., the macroscopic thermal conductivity. Thus, we fix the internal thermal relaxation constant $\frac{\kappa^{\mathrm{int}}\tau_{\mathrm{md}}}{k_{\mathrm{B}}T^2} = 500$ to a low value. The soft interaction parameter v_{ij} varies in the range of $v_{\mathrm{ij}} = 1 - 500$ (the relation of eq. 3.52 allows us to calculate the range $K^{iso}N \approx 42 - 2.13 \cdot 10^4$).

The general parameters of the system are: chain discretisation $N = 16$, system size in σ $L/\sigma^3 = 56 \times 6 \times 6$, specific heat capacity applied to universal form of entropy $c_V/k_{\mathcal{B}} = 10000$, and number density $\rho\sigma^3 \approx 12.7$. An energy current $\frac{\mathrm{rnecurrent}\tau_{\mathrm{md}}\sigma^2}{k_{\mathrm{B}}T} = 200$ is applied to the internal **DoF**s. Fig. 4.6 shows the steady-state temperature profiles that emerge by applying a **RNEMD** current. Here, different colours indicate the strength of the soft interaction parameter. Temperature profiles' slopes decrease as soft interaction increases, which indicates a higher macroscopic

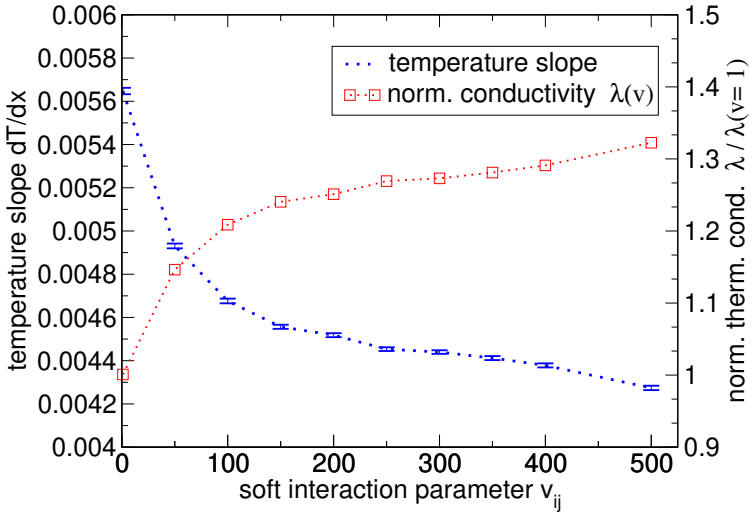

Figure 4.7 The blue chart represents the slope, $\frac{\partial T}{\partial x}$, of temperature of the profiles presented in fig. 4.6, as a function of the soft interaction parameter, v_{ij}, (eq. 3.52). Slopes give rise to the macroscopic thermal conductivity $\lambda(v_{\mathrm{ij}})$, which is normalised by macroscopic thermal conductivity $\lambda(v_{\mathrm{i}j}) = 1$. Parameters are equal to figure 4.6.

thermal conductivity at higher soft interaction parameter v_{ij}. Fig. 4.7 represents slope (blue) and thermal conductivity (red dashed line) of temperature profiles fig. 4.6, which have been evaluated. The slope was calculated by a linear fit, error bars result from the fit procedures. The thermal conductivity (red) was normalised by the homopolymer melt's thermal conductivity at soft interaction parameter $v_{\mathrm{ij}} = 1$. Hence, the second ordinate shows the fraction by which macroscopic thermal conductivity has increased. The normalised thermal conductivity can be divided in two areas. In the first interval up to $v_{\mathrm{ij}} < 100$, the conductivity increases fast, whereas in the second part, $v_{\mathrm{ij}} > 100$, the conductivity slightly rises.

Discussion Without any additional information about the system one can indicate two reasons for an increase of the thermal conductivity. The first reason: if the soft interaction parameter increases, the energy that can be exchanged by momenta is higher, i.e., the speed of sound of the system increases by $c = \sqrt{\frac{\partial p}{\partial \rho_m}}$, where p represents pressure and ρ_m mass density, respectively. Hence, we did simulations of a homopolymer melt without internal **DoF** of density waves in the system, sec. 4.8.3, but even if the speed of sound of a longitudinal wave (pressure wave) increases trough the soft interaction parameter, this does not explain the quantitative scaling of

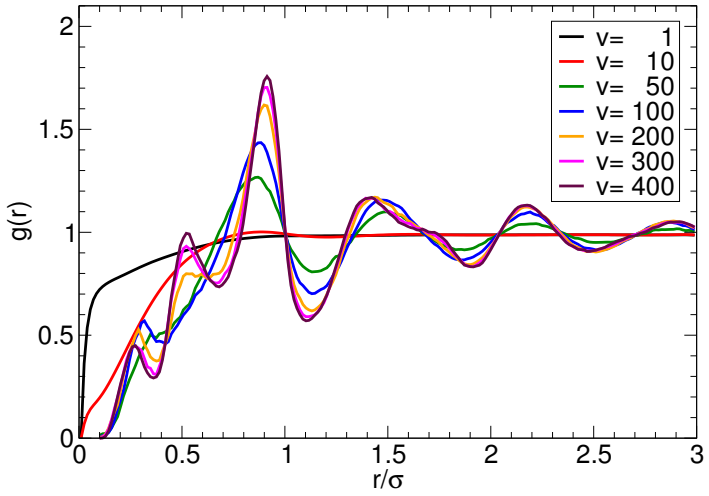

Figure 4.8 Pair correlation function, $g(r)$, of a soft polymer melt with varied soft interaction parameter v_{ij}. Peaks indicate that the polymer melt becomes a structured fluid for increased v_{ij}. Overall parameters are $N = 16$, $L/\sigma^3 = 56 \times 6 \times 6$, $c_V/k_{\mathrm{B}} = 10000$, $\rho\sigma^3 \approx 12.7$.

thermal conductivity, fig. 4.7. The second reason: the system undergoes a transition that implies fluid-like packing effects. Usually, the system's parameter are chosen so that homopolymers are a soft fluid, which radial pair distribution function equals $g(r) \approx 1$. Hence, $g(r)$ has been measured for all systems, fig. 4.8. The number of particles interacting via **eMC** in range σ is calculated by numerical integration of $g(r)$ from $r\sigma^{-1} = 0$ up to $r\sigma^{-1} = 1$. The number of neighbours are stated in second column of tab. 4.4. If the process is dominated by **eMC** (even if the maximum value of soft interaction is high $v_{\mathrm{ij}} = 500$ and the internal thermal relaxation was chosen to be small), the macroscopic thermal conductivity, $\lambda \sim (\rho\sigma^2)^2$, scales with the density that can be related to the number of interacting particles in a sphere with radius σ. Hence, we calculate the squared number of interacting particles and rescale this number by number of particles at $v_{\mathrm{ij}} = 1$ (third column tab. 4.4). This is compared with the thermal conductivity (tab. 4.4, fourth column), which has been rescaled by its value at $\lambda(v_{\mathrm{ij}} = 1)$, too. Finally, we conclude that the soft interaction parameter v_{ij} influences thermal conductivity mainly by structural change, i.e., a change of interacting neighbours that scales with density squared, too. Indeed this relies on a thermal transport that is mainly influenced by internal **DoF**s, because the **RNEMD** current has been applied to the internal **DoF**s, too. Hence, up to this

v_{ij}	neighbouring particles	$\frac{\mathrm{particle}(v_{ij})}{\mathrm{particle}(v_{ij}=1)}$	$\lambda(v_{\mathrm{ij}})/\lambda(v_{\mathrm{ij}}=1)$
1	53.00	1	1.00(1)
50	54.56	1.06	1.14(6)
100	56.94	1.15	1.20(8)
200	58.88	1.23	1.25(10)
300	59.64	1.26	1.27(3)
400	60.04	1.29	1.29(10)

Table 4.4 Number of particles in the interaction radius $r_0/\sigma = 1$ (second column) calculated from the pair correlation function, fig 4.8, as a function of soft interaction parameter v_{ij} (first column). (third column) squared number of interacting particles rescaled by the number of particles at $v_{\mathrm{ij}} = 1$. (fourth column) macroscopic thermal conductivity as function of soft interaction parameter, rescaled by macroscopic thermal conductivity at $v_{\mathrm{ij}} = 1$.

point, it remains open how thermal transport changes under modifying interaction parameters? If internal **DoF**s are left out, and if the thermal current is applied to external **DoF**s only. However, later, on we will investigate the thermal conductivity of a soft fluid without internal **DoF** cf. sec. 4.7.

Polymer length

Decimated **DoF**s are lumped together into an internal energy. In principle, these **DoF**s are specified by translation, rotation, vibration, etc., but the time and length scale of the dynamics of these **DoF**s are different from **eMC**. Certainly, vibrational frequencies, i.e., phonons, propagate much faster along a chemical bond than via a non-bonded interaction. Hence, the dynamics of these inter-molecular and intramolecular connections motivate a differentiation of the internal relaxation parameter κ_{int} depending on the underlying molecular architecture. Therefore, we choose a different thermal relaxation constant according to the underlying architecture. If two segments are bonded together, the deterministic thermal relaxation constant, κ_{int}, is called *intramolecular*. Considering the non-bonded interaction the thermal relaxation constant is the *inter-molecular* one. The transport along a polymer is modelled such that **eMC** is always applied to two bonded beads, even if their distance is outside of the normal **eMC** interaction range of one σ (the averaged distance between bonded particles is $b = 1\sigma$). The influence of chain length on conductivity is studied in a polymer melt, which is comprised of homopolymers discretised by $N_{xx} = [8, 32, 64, 128]$ segments. In sec. 4.2, we discussed the rescaling

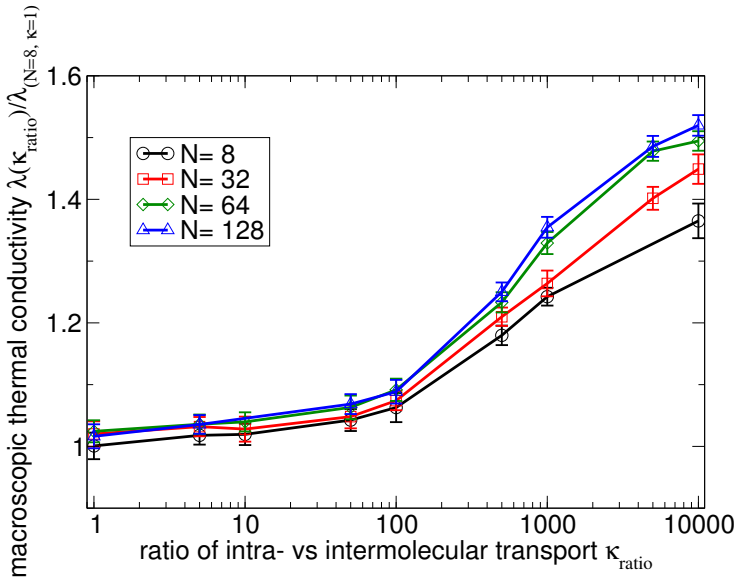

Figure 4.9 The thermal conductivity as a function of the ratio of inter- versus intramolecular thermal relaxation constant, for various lengths (number of segments) of a linear polymer chain, $N = 8$, 32, 64, 128. Thermal conductivities are observed by **RNEMD** simulations. All values are normalised to macroscopic thermal conductivity of a polymer consisting of $N = 8$ segments. The averaged density $\rho\sigma^3$ is kept constant. In consequence, the systems are distinguishable by their number of bonded interactions only.

of parameters, which allows us to observe a temperature profile in steady-state, which is invariant under the underlying explicit discretisation. Here, the averaged density $\rho\sigma^3$=11.9, specific heat capacity $c_V = 99$, total number of particles $N_{xx}n = 32512$, volume $V\sigma^{-3} = 80\times6\times6$, and soft interaction $v_{\mathrm{ij}} = 0.66$ are kept unaltered, whereas the intramolecular thermal relaxation is stepwise increased. The inter-molecular conduction is kept constant at a value of $\frac{\kappa_{\mathrm{int}}^{\mathrm{inter}}\tau_{\mathrm{md}}}{k_{\mathrm{B}}T^2} = 10$. This ensures that the difference of thermal conductivities mainly depends on chain connectivity. Fig. 4.9 represents the macroscopic thermal conductivity as a function of the ratio of intra- and inter-molecular thermal relaxation. The abscissa indicates the ratio of inter- and intramolecular thermal relaxation constant. The maximum ratio that has been considered is $\frac{\kappa_{\mathrm{int}}^{\mathrm{intra}}}{\kappa_{\mathrm{int}}^{\mathrm{inter}}} = 10000$, which agrees with an instantaneous thermal relaxation of two internal **DoF**s, i.e., the maximum is $\frac{\kappa_{\mathrm{int}}^{\mathrm{max}}\tau_{\mathrm{md}}}{k_{\mathrm{B}}T^2} = 100000$. The macroscopic thermal conductivities are extracted from the slope of a temperature profile in steady-state, which was created by the **RNEMD** scheme acting on internal **DoF**s [11, 65]. The colours indicate the discretisation of the homopolymer, black N_8, red N_{32}, green N_{64}, blue N_{128}. A high intramolecular relaxation induces a higher bulk

conductivity. The values have been rescaled by λ_{N_8} at $\kappa_{\text{ratio}} = 1$. In this figure, κ_{ratio} represents the ratio of relaxation constants $\frac{\kappa_{\text{int}}^{\text{inter}}}{\kappa_{\text{int}}^{\text{intra}}}$.

Discussion At first glance, one observes that the macroscopic thermal conductivity, λ, of an isotropic polymer melt increases by the ratio of inter- and intramolecular conductivity by a factor of ~ 1.5. At a fixed ratio, a higher number of segments increases the macroscopic thermal conductivity, too. The macroscopic thermal conductivities at a ratio $\kappa_{\text{ratio}} = 1$ differ, because the number of interactions that is given by the neighbouring shell of radius σ is different. The difference is caused by the additional condition that was introduced to **eMC**, because the **eMC** scheme will always be applied to bonded particles, even if their distance is larger than the cut-off distance σ. This number of additional connections increases by a polymer's degree of polymerisation.

The fact that the inter- and intramolecular transport acts on different scales[7] has been found in atomistic molecular dynamic simulations, e.g., the role of the molecular mechanism of heat conduction in a liquid of different alkane species has been calculated via non-equilibrium molecular dynamic simulations (Lennard-Jones potentials in atomic units). For the applied length scale of our universal linear polymers we qualitatively agree with their simulations [68], i.e., they have calculated different transport coefficients corresponding to stretching, angle, torsion, and the inter-molecular part of the van-der-Waals forces. They also concluded that, if the degree of the polymerisation is increased, the macroscopic conductivity will be dominated by intramolecular transport processes, and is increased [69]. Simulations on the thermal conductivity of single polyethylene chains using molecular dynamics simulations showed that intramolecular conductivities can outperform thermal properties of compared bulk systems by orders of magnitudes [70][8]. Finally, experimentalists showed that the thermal conductivity of polyethylene nano-fibres is 1000× higher compared to a bulk thermal conductivity, which is of the order of ~ 0.1 [W/mK] [71]. This indicates that the ratios that have been chosen for inter- and intramolecular thermal relaxation of internal **DoF** can be directly related to experimental results. Hence, the results provided by fig. 4.9 can be experimentally proven by the following setup: two systems of homopolymers with a ratio of degree

[7] Typically, molecular bond vibrations are in the tera-hertz regime, which reveals a high ability to transport energy. Unconnected molecules interact via van-der-Waals forces, which are comparatively weak and more susceptible.

[8] They calculated the thermal conductivity of a polyethylene nano fibre to $\frac{\lambda\,\mathrm{m\,K}}{\mathrm{W}} = 350$.

of polymerisation, which is 16 (N_{128}/N_8). A ratio of 1000 in the thermal relaxation constants indicates a difference of about 20% in macroscopic thermal conductivity, which is within the possibility of an experimental measurement.

4.4 Diblock copolymers - eMC in steady-state

A major goal in engineering applications is a control tactic of energy transport. Energy-transport phenomena, which give rise to a control tactic, have been known for a long time, e.g., thermal resistance at an interface [72]. Also, combining materials with different thermal characteristics into interface-forming composites can outperform the bulk properties of the materials. These composite materials benefit from a strongly reduced phonon propagation caused by the phonon mismatch at the interfaces. Promising candidates, tungsten/polycarbonate multilayers, have been found by pump-probe experiments [6]. In contrast to the expense of creating these structures, directed self-assembly of polymers gives rise to composite structures by minimal effort. Especially, if these polymers are highly functionalised, i.e., inclusion of silica and gold nano particles. Although, polymers are treated as insulators by the majority this is true for the bulk behaviour only, because thermal conductivity of a single chain can be orders of magnitudes higher, e.g., polyethylene nanofibres [71, 73]. Hence, we investigate two mechanisms: the first mechanism is the Kapitza resistance, i.e., thermal resistance, induced by an interface. The second mechanism uses the high intramolecular conductivity along the chain to compensate the thermal barrier of an interface.

4.4.1 Kapitza resistance

To verify the effect of a thermal resistance, we apply **eMC** simulations to AB-diblock copolymers, which have been self-assembled and equilibrated to a lamellar structure. The **eMC** scheme incorporates interface effects primarily by varying the internal relaxation, κ_{int}, according to the type of internal pairwise interaction. The first numerical example has an invariant degree of polymerisation $\bar{\mathcal{N}} = 15000$, density $\rho\sigma^3 = 21.5$, and an internal specific heat of a single **DoF** $c_V/k_{\text{B}} = 3000$. The thermal relaxation within a type A or B is assumed to be one order of magnitude higher than the thermal relaxation between different types. The internal conductivity along a chain is independent of the type of polymer. To be more accurate, we now differentiate between four different internal thermal relaxation constants into

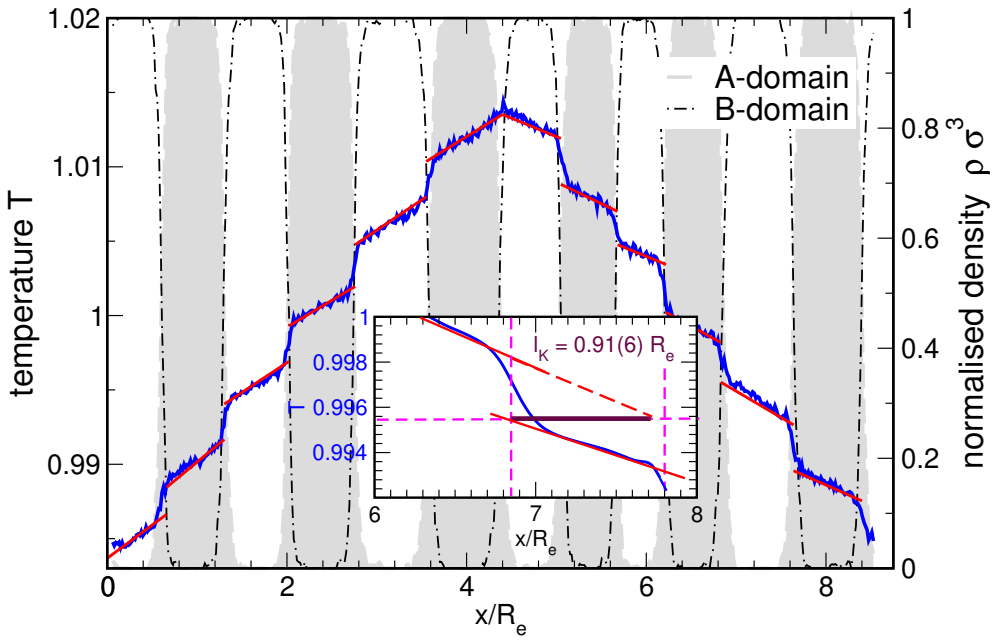

Figure 4.10 A heat flux is applied to an AB multilayer formed by directed self-assembly of diblock copolymers. The normalised number density $\rho\sigma^3$ indicates the alternating AB multilayers. **RNEMD** induces a temperature profile T(x). Reducing the internal thermal relaxation constant for inter-molecular interaction between A and B species induces a sharper gradient at the interface. This is illustrated in the inset more precisely. Parameters are $\frac{\kappa_{\text{intra}}\tau_{\text{md}}}{k_{\text{B}}T^2} = \frac{\kappa_{\text{AA}}\tau_{\text{md}}}{k_{\text{B}}T^2} = \frac{\kappa_{\text{BB}}\tau_{\text{md}}}{k_{\text{B}}T^2} = 1000$, $\frac{\kappa_{\text{AB}}\tau_{\text{md}}}{k_{\text{B}}T^2} = 100$, $K_{\text{iso}} = 10$.

the deterministic part of **eMC**. Depending on the architecture, we decide on a different kind of thermal relaxation. If two interacting particles are connected via a harmonic potential, the thermal relaxation constant is called intramolecular thermal conductivity, $\frac{\kappa_{\text{intra}}\tau_{\text{md}}}{k_{\text{B}}T^2} = 1000$. If particles interact via a non-bonded potential, only their internal thermal relaxation is $\frac{\kappa_{\text{AA}}\tau_{\text{md}}}{k_{\text{B}}T^2} = 1000$ and $\frac{\kappa_{\text{BB}}\tau_{\text{md}}}{k_{\text{B}}T^2} = 1000$. It is assumed that the **DoS** of two bulk systems are different. Hence, modes are only transported from one coarse-grained segment to the other if they can propagate in both bulk phases. Therefore, in a first approach, the inter-molecular internal thermal relaxation between A and B types is reduced, $\frac{\kappa_{\text{AB}}\tau_{\text{md}}}{k_{\text{B}}T^2} = 100$.

Using the **RNEMD** strategy, we apply an energy flux to a self-assembled multilayer of diblocks. This induces the steady-state temperature profile, shown in fig. 4.10. The abscissa has been rescaled by the invariant scale of the averaged end-to-end

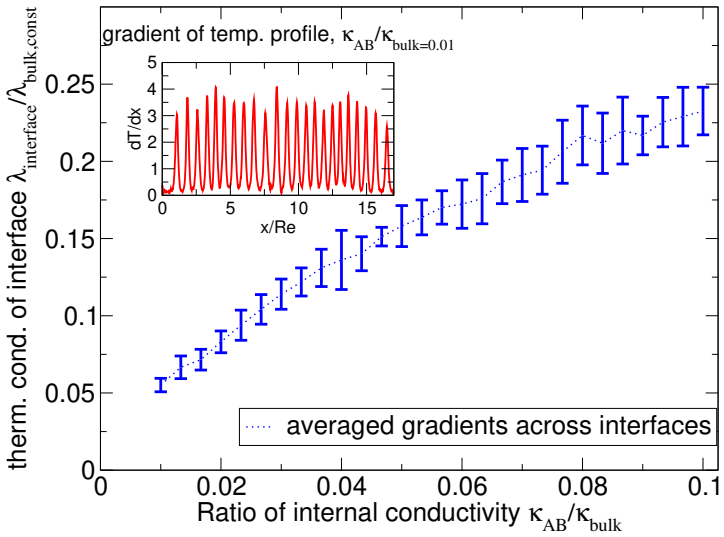

Figure 4.11 Macroscopic thermal conductivity, $\lambda_{\text{interface}}$, at the interface of alternating polymer domains formed by AB diblocks. Conductivity $\lambda_{\text{interface}}$ is normalised by thermal conductivity of the bulk, $\lambda_{\text{interface}}$. Inset: gradient of the observed steady-state temperature profile T(x), cf. fig. 4.10. To the left hand side, the internal thermal relaxation,κ_{intAB}, between AB interactions is reduced so that resistance of the interface increases.

distance $R_e = b \cdot \sqrt{N_{32}}$. A-phase is coloured grey and B-phase is coloured white. At the AB interface, the temperature gradient is sharper than in the bulk region. For the bulk region, the slope corresponds to the one of a melt of homopolymers [11]. Assuming that the interface is sharp, there is a jump in the temperature that can be related to the Kapitza resistance. The geometrical expression for the Kapitza resistance is given by the inset of fig. 4.10. The Kapitza length in this numerical example is $R_e = 0.91$. It has been shown before that the macroscopic thermal conductivity is proportional to the squared density ρ^2. In case of a melt of diblock copolymers, our soft model has a small density dip at the interface (this is model specific and larger than in experimental systems). This dip, in principle, influences the macroscopic thermal conductivity across the interface, but this dip (i) is small in contrast to the interaction range of **eMC** and (ii) averaged out by considering the average internal energy per particle in a specific slab. To demonstrate that the density dip does not dominate the behaviour, the thermal relaxation, κ_{AB}, between A and B types is reduced systematically. The averages over uncorrelated steady-state temperature profiles allows us to calculate a smooth gradient from the

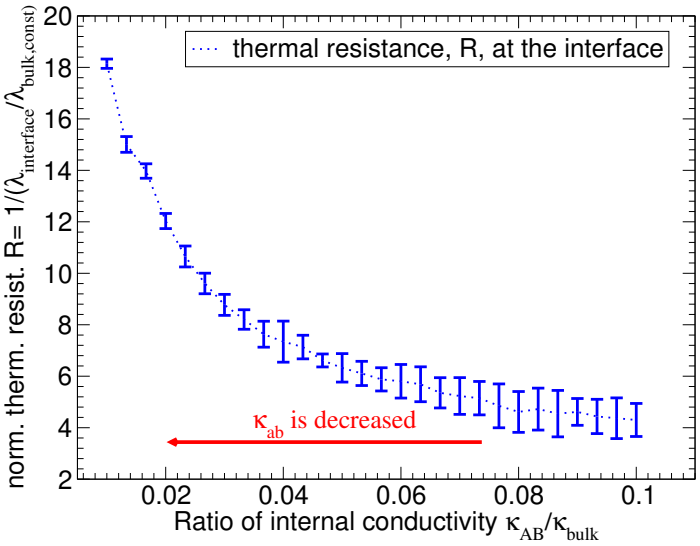

Figure 4.12 Macroscopic thermal resistance, $R = \lambda^{-1}_{\text{interface}}$ at the interface of alternating polymer domains formed by AB diblocks, cf. fig.4.11. Resistance is normalised to thermal resistance of the bulk. The resistance increases for reducing the internal relaxation, κ_{AB}

temperature profile, inset fig. 4.11. The maximum of the gradient is located at the interface and enables us to calculate the thermal conductivity at the interface λ_{inter}. The minimum belongs to the thermal conductivity of bulk phase of A or B, λ_{bulk}. Fig. 4.11 presents the thermal conductivity at the interface as a function of ratio of internal relaxation constant, $\kappa_{\text{ratio}} = \frac{\kappa_{\text{int AB}}}{\kappa_{\text{int bulk}}}$. For a low value of internal relaxation of $\kappa_{\text{int AB}}$, the conductivity of the interface is reduced. Fig. 4.12 presents the thermal resistance of the interface, $R(\kappa_{\text{ratio}}) = \frac{\lambda_{\text{bulk}}}{\lambda(\kappa_{\text{ratio}})}$. The resistance, R, represents a dimensionless quantity, because R was normalised by the bulk conductivity, λ_{bulk}. The bulk conductivity corresponds to a pure homopolymer melt without advanced structures, i.e., interfaces. In the limit $\kappa_{\text{int AB}} \to 0$ the resistance will go to $R \to \infty$ and in the limit of $\kappa_{\text{int AB}} \to \kappa_{\text{bulk}}$ and loss of structure information the resistance R will be one. However, measurement in this regime is computationally intensive, because small gradients require more statistics.

Discussion The essence of fig. 4.12 is to connect simulations and experiments: take any experimental setup and measure a thermal conductivity for (a) ordered polymer melt, (b) disordered polymer melt, e.g., PMMA-b-PS. In case of an ordered lamellar polymer phase (a) one can estimate by atomic force microscopy the average

number of interfaces, i.e., lamellar period. Knowing the number of interfaces and global thermal bulk conductivity (b) by experimental results allows for an estimation of the thermal resistance of a single interface. This can be used to determine the ratio of the internal relaxation constants κ_{int}, because the interfacial influence on thermal transport properties determine the internal relaxation constants according to a top-down approach by experimental results.

Kapitza resistance also has been observed by molecular dynamic simulations of a hard/soft interface [74], as well as by Lennard-Jones super-lattices [30], but these methods are limited to small time and length scales.

4.4.2 Cut diblocks

Interfaces created by directed self-assembly induce a thermal resistance. However, results also showed that intramolecular transport properties influence thermal conductivity, too. Hence the following hypothesis was confirmed: molecular connectivity across an interface influences macroscopic transport properties of the materials. This effect can be isolated by changing the morphology of AB diblocks to A and B homopolymers, i.e., cutting the diblocks at the junction point. The junction points of the AB diblocks are localised at the interface region. However, the part of intramolecular connections is much smaller than the inter-molecular ones. To enhance their influence one increases the intramolecular thermal relaxation constant by up to 5 orders of magnitudes, $\frac{\kappa_{intra}\tau_{\text{md}}}{k_{\text{B}}T^2} = 10^6$, $\frac{\kappa_{\text{inter}}\tau_{\text{md}}}{k_{\text{B}}T^2} = 10$. Hence, the intramolecular coupled internal energies relax fast. This is consistent with previous studies, i.e., experimental results indicate a high thermal conductivity of polyethylene nano-fibres [71, 73]. If the lamella structure is formed by directed self-assembly, a **RNEMD** current is applied to the system. Hence, a steady-state temperature profile is observed, fig. 4.13 (blue). The same system is taken, but the junction points are cut in order to have alternating domains of A- and B-homopolymers with the same characteristics [9]. Now, the intramolecular connections, which have compensated the interfacial resistance, are eliminated and one observes a small resistance at the interfaces of homopolymer layers (red dashed line). The interfaces are periodically averaged so that a geometrical expression of Kapitza length is observed, inset fig. 4.13. The linkage between the A- and B-block across the interface increases the macroscopic thermal conductivity that compensates for the Kapitza resistance,

[9] The alternating domains of homopolymers are only metastable and will undergo a transition from a micro- to a macro-phase.

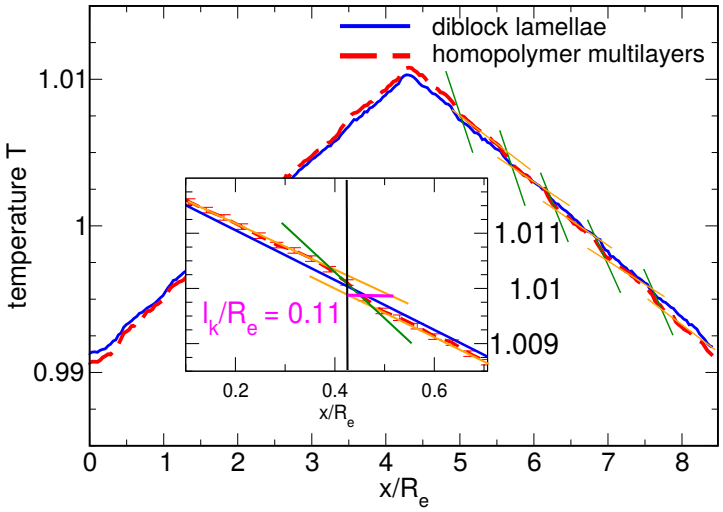

Figure 4.13 Thermal transport through alternating AB multilayers. The layers are either comprised of self-assembling copolymers or layers of macro-phase-separated homopolymers. The systems are identical with the exception of their molecular connectivity. The linkage between the A- and B-block in the copolymer increases the macroscopic thermal conductivity and decreases the Kapitza resistance, $l_K/R_e \approx 0.11$, at the interfaces. In the inset the temperature was averaged for all interfaces.

$l_K/R_e \approx 0.11$, which is observed for the case of alternating homopolymers without the connection of junction points.

Conclusion We conclude that junction points act like thermal bridges and compensate the barrier of the interfaces, i.e., they thermally connect the bulk regions and act like antennae that spread energy. The idea of spread energy to a system will be continued by investigation of energy transport of star polymers in the next sec. 4.5.

4.5 Star polymers - eMC in non-equilibrium state

As previously shown, thermal conductivities depend on the length of polymers, and polymers can act like thermal bridges to connect two bulk phases. Star polymers come along with an additional spatial arrangement, which is correlated with its thermal properties.

We define the structure of a star polymer by a junction point, which is the centre of the star, and a specific number of arms, which are connected to this junction point.

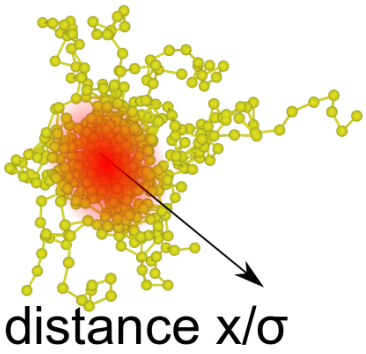

Figure 4.14 Star polymer with 15 arms. Each arm consists of 31 monomers. Total number of segments, which correspond to the star polymer is $n = 15 \cdot 31 + 1 = 466$. Size is measured in terms of the radius of gyration. The star polymer is surrounded by homopolymers, which are not visualised. Colour indicates decline of internal energy/temperature, compare fig. 4.17.

The length of an arm is fixed to 31 monomers. Hence, a star polymer with $N = 15$ arms consists of $n_{\text{star}} = 15 \cdot 31 + 1 = 466$ monomers, fig. 4.14. The star polymer's characteristic invariant length scale is defined by the radius of gyration R_g. Each simulation considers only one star polymer in a box $V \cdot \sigma^{-3} = 30 \times 30 \times 30$ with periodic boundary conditions. The star polymer is surrounded by homopolymers discretised into $N = 32$ beads. The averaged density of this system is $\rho_0 \sigma^3 = 11.32$ such that the system contains about $n_{\text{all}} = 3.05 \cdot 10^5$ particles. The number of arms of the star polymer is limited roughly by averaged density ρ_0 times volume of unit sphere $r = 1\sigma$. In consequence, the largest star polymer consists of 45 arms - $n_{\text{star}} = 1396$ monomers. In principle, more arms are possible but remaining under the limit of the averaged number density ensures that packing effects in the star remain small. The largest star polymer has a fraction of $n_{\text{star}}/n_{\text{all}} \approx 0.5\%$ according to the total volume. Hence, inserting a small portion of energies to the star polymer will not have an influence on global temperature $k_B T = 1$. Figure 4.15 shows the normalised density distribution of monomers, which correspond to the star polymer (top) or to surrounding homopolymers (bottom). The spatial position of the junction point is located at $x/\sigma = 0$. All polymers have an isothermal compressibility $NK_{\text{iso}} = 30$. The interaction between star polymers' arms and the surrounding homopolymers are chemically neutral, i.e., $\chi N = 0$. The systems are large, thence, they are created via **SCMF** simulations. The systems have been simulated for five Rouse relaxation times, which are defined by the surrounding homopolymers. Thereupon, the configuration is handed over to the implementation of **eMC** scheme. The structure that is read in, is relaxed for one Rouse time

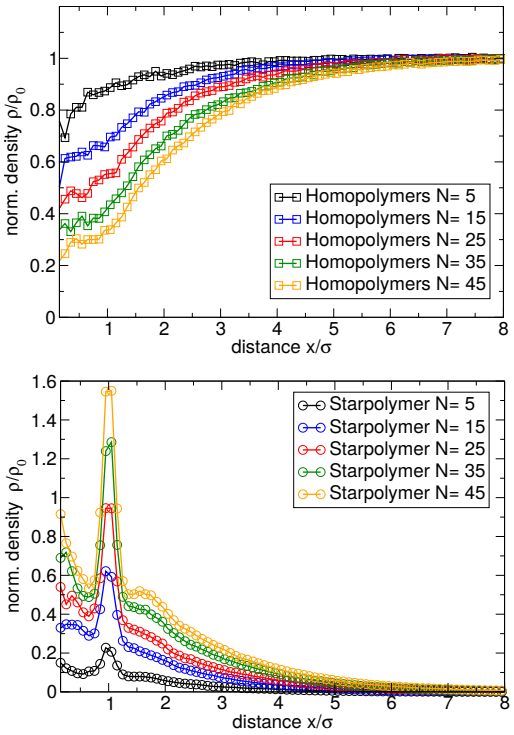

Figure 4.15 Normalised density distribution of a star polymer in a melt of homopolymers $N_{\text{homo}} = 32$. The junction point of the star polymer sets the origin $x/\sigma = 0$. Circles correspond to star polymers (top), and squares correspond to homopolymers (bottom). Each arm consists of 31 monomers, and N is the star polymer's number of arms. The x-length is scaled by the averaged bond distance.

again before the measurement of relaxing of an inserted energy portion starts. The internal thermal relaxation constant is set according to the molecular connectivity $\frac{\kappa_{\text{inter}}\tau_{\text{md}}}{k_{\text{B}}T^2} = 100$ and $\frac{\kappa_{\text{intra}}\tau_{\text{md}}}{k_{\text{B}}T^2} = 500000$. Hence, κ_{intra} matches the maximum thermal internal relaxation constant κ_{max}. The internal specific heat capacities are set equally to $c_V = 1000\ k_{\text{B}}$ independently from the type of segment. The integration and the **eMC** update is set to $\mathrm{d}t\tau^{-1} = 0.001$. Fig. 4.15 represents two types of densities, homopolymers' and star polymers' density. This densities are rescaled by the system's averaged number density ρ_0. Colours indicate the number of arms. Star polymers have a peak at $x/\sigma = 1$, which corresponds to the first nearest neighbours of the junction point, i.e., the star polymer's centre. The peak is increased by the star polymer's number of arms. The ends of the star polymer's arms are free, i.e., there is no preference to be dissolved by the surrounding fluid comprised of homopolymers. Hence, homopolymers smoothly enter the space between the arms. If the number of arms is low, the space in between is larger. If the number of arms is higher, the space in between is smaller, fig. 4.15. If one modifies the incompatibility, $\chi N = 20$, one induces a repulsion between the star polymer's arms and the surrounding fluid. Hence, the star polymer reorders into a sphere. The radius of the sphere depends on the volume, which is defined by the number of arms and the averaged density $R_{\text{sphere}}/\sigma = \left(\frac{3V}{4\pi\rho_0}\right)^{1/3}$. Figure 4.16 shows the normalised

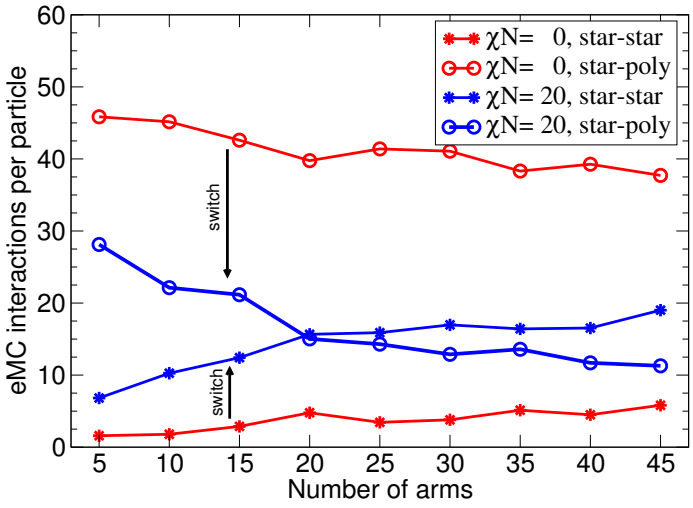

Figure 4.16 Number of eMC interactions per particle in interaction range $R = \sigma$ as a function of the number of arms. A particle that belongs to a star polymer has two types of interaction, star-star and star-(homo)poly(mer). Red curves correspond to full solubility with $\chi N = 0$. Blue curves corresponds to $\chi N = 20$, which induces a compression of the star polymer into a sphere. The number of interactions significantly decreases by switching, $\chi N = 0 \rightarrow 20$.

number of neighbours considered for internal energy exchange during the **eMC** step, i.e., denoted by *interactions* in the following, for two cases: star-to-star and homo-to-star polymer interactions. Technically, we iterate over all star polymer's particles and count the number of interactions that occur due to the interaction of star-star and star-homopolymer. The two kind of interactions are counted in two conditions $\chi N = 0$ and $\chi N = 20$, respectively. The red curves correspond to full solubility $\chi N = 0$. The blue curves correspond to stars that have been compressed into a sphere with $\chi N = 20$. In case of $\chi N = 0$, the star polymer's arms are fluctuating freely, hence star-to-homopolymer interactions are the largest ones. In case of changing from $\chi N = 0$ to $\chi N = 20$ the reordering into a sphere is accompanied by a reduction of possible homopolymer-to-star polymer interactions. Now we continue to investigate star polymers' dynamic properties. To determine a thermal relaxation of the star polymer, we double the internal energies of the monomers corresponding to the star polymer, $e_{\text{int}} = 2 \cdot e_0 \cdot k_{\text{B}}T$. Then, we track the averaged internal energy at distance r as function of time.

Figure 4.17 represents the internal energy normalised by the equilibrium internal

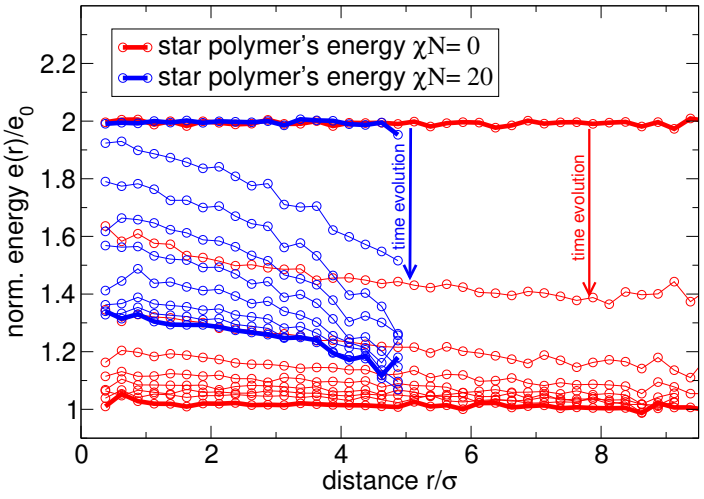

Figure 4.17 Origin $r/\sigma = 0$ is set by the centre of mass of the star polymer. Averaged energy $e(r)$ at position r is normalised by the equilibrium internal energy of a monomer e_0. Initial energy of the star polymer is twice as large as the equilibrium internal energy of a monomer e_0. The time interval between the curves is small, $0.125\ \tau_{\mathrm{md}}$.

energy e_0 as a function of distance from the centre of mass of the star polymer. In this example, the star polymer consists of 30 arms. Blue curves indicate $\chi N = 20$ and the red ones $\chi N = 0$, again. The time difference between each of the curves is $0.125\ \tau$. The blue curve ends at ~ 5, because this corresponds to the radius of gyration of a star polymer with 30 arms that has been compressed into a sphere. We observe that the relaxation of energy happens faster in the system where the star polymer's arms have good solubility, $\chi N = 0$. The example is extended to multiple number of arms. In these systems, the sum of internal energy of the star polymer is tracked by time, since the star polymer's internal energy has been increased by $e_{\mathrm{int}} = 2 \cdot e_0 \cdot k_{\mathrm{B}}T$. Hence, the total energy that is added to the star is twice the equilibrium energies of particles that correspond to the star polymer. This tracking allows us to determine a thermal relaxation parameter as a function of the number of arms. In the limit that the internal relaxation κ_{int} is high the heat-transfer is not exclusively diffusive. The form changes to Newton's law of cooling, i.e., Fourier's law, eq. (2.14), because the gradient of transported energy is constant. For the

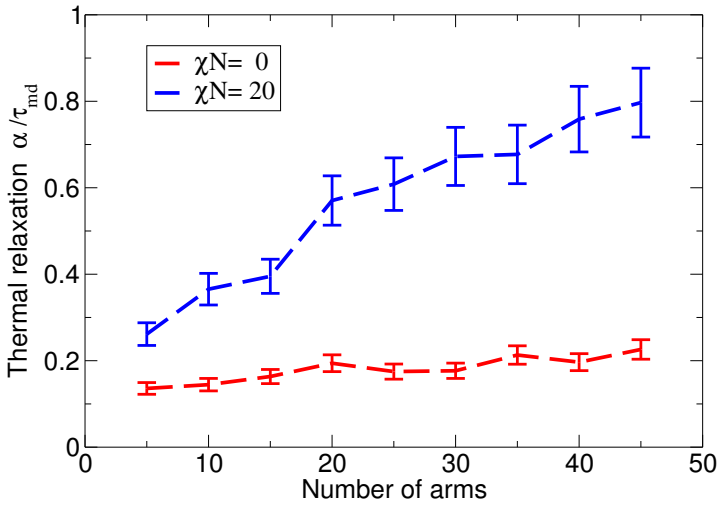

Figure 4.18 Thermal relaxation α, eq. (4.4) as a function of number of arms of the polymer. The red curve corresponds to full solubility with a $\chi N = 0$. The blue curve corresponds to a $\chi N = 20$, which induces a compression of the star polymer to a sphere. In this case, the number of **eMC** *interactions* reduces to the ones at the surface.

internal energy. i.e., internal temperature, we can formulate the relation

$$T_{\text{int}}(t) = T_{\text{int}} + T_{\text{int}} \cdot \exp\left(-\frac{t}{\alpha}\right). \tag{4.4}$$

α represents a relaxation time. Eq. (4.4) is fitted to the energy data - results are shown in fig. 4.18. It represents the two cases of $\chi N = 0$ (red curve) and $\chi N = 20$ (blue curve). If α is small, the relaxation will be fast. If α is high, the relaxation of energy from star polymer into the surrounding fluid will be slow. A more intuitive way to interpret α is the mean time of energy to stay in the star polymer.

Discussion In principle, we observe two time scales in the thermal relaxation of star polymers. The first time scale is defined by the distribution of energy in the star polymer itself. The second one is the time scale on which energy is absorbed by the surrounding fluid. In this example, we restricted us to the second case only. The internal thermal relaxation constant is chosen to be at the maximum limit in order to ensure a fastest thermal relaxation of two segments inside the star polymer. If

we double the equilibrium[10] energy of each star polymer's particle, this corresponds to an equally distributed energy in the star polymer, i.e., the first time scale is negligible. We showed that switching the morphology of the star polymer, which induces a compression into a sphere increase the time energy required to relax. Hence, the effective interface between star polymer and homopolymers reduces the possible **eMC** interactions as well. Therefore, the energy leaves the star polymer much slower. This can be related in a one-to-one correspondence to the number of surrounding particles, which absorb the star polymer's energy. The results might open the question: does the number of arms increase the thermal relaxation, because more arms should spread energy more efficiently? We conclude that the relaxation depends on the possibility of transferring energy contained in the arms to the fluid. This is reduced with an increasing number of arms, because the number of **eMC** interactions per number of arms decreases, fig. 4.16. It remains the question whether structures that have been investigated in this example can be addressed by real experiments. Fortunately, photo-responsive star-polymer shells have been created by Dennis Hübner [75]. Here, the junction point is set by a gold nanoparticle and the arms are functionalised by cis-to-trans isomerisation of azobenzene-containing molecules, for some details also compare to sec. 4.9. The essence is that they may be used as a tactic to control thermal relaxation by the solubility of the star polymers in the solution. In the spirit of thermal antennae that can be switched by light between two states, they exhibit high and low thermal relaxation, respectively.

4.6 Thermal conductivity of homopolymers separated by simple cubic soft crystals

The thermal conductivity of crystals is typically orders of magnitudes higher than the thermal conductivity of polymers. The difference can be rationalised by the structural difference of the bonds and the specific heat capacities. Hence, in order to represent hard and soft materials, we use a structural difference for the bond structure and external microcanonical interactions.

The polymers interact via a soft repulsive potential $\frac{V(r_{ij})}{k_B T} = \frac{v_{ij}}{2}(1-r)^2$ with repulsion parameter $v_{ij} = 1$ and a cut-off at $r/\sigma = 1$. The potential of two connected

[10] Equilibrium energy means energy of star polymer at internal temperature equals $T = 1$. Hence, when we double the internal energy, we increase the star polymer's temperature, too. Certainly, the fraction of star polymer's energy weighted to the complete system is about one-tenth of a per cent that global temperature is kept constant in first approximation.

monomers is harmonic and centred at $r_{\mathrm{ij}} = 1\sigma$, $\frac{V(r_{\mathrm{ij}})}{k_{\mathrm{B}}T} = \frac{E_B}{2}(1 - r/\sigma)^2$.

The crystal is formed via harmonic bonds, $\frac{V_{\mathrm{cry}}(r_{\mathrm{ij}})}{k_{\mathrm{B}}T} = 10 \cdot (a - r/\sigma)^2$, with minimum potential energy at $a = 0.5$. The structure is arranged on a cubic lattice such that each particle has six nearest bonded neighbours. The crystal also has a soft repulsive interaction between non-bonded particles with interaction parameter $v_{\mathrm{ij}} = 5$. The soft repulsive interaction between homopolymers and crystal segments is set to $v_{\mathrm{ij}} = 1$.

The thermodynamic properties are kept universal in the sense that we address specific heat capacities and internal thermal conductivities on the right order of magnitudes. Specific heat capacity of a crystal's particle is $c_V/k_{\mathrm{B}} = 5000$, and the specific heat capacity of a polymer segment is $c_V/k_{\mathrm{B}} = 500$. The internal thermal relaxation constants are (i) polymer $\frac{\kappa_{\mathrm{int}}^{\mathrm{Poly}}\tau_{\mathrm{md}}}{k_{\mathrm{B}}T^2} = 1000$, (ii) crystal $\frac{\kappa_{\mathrm{int}}^{\mathrm{Cry}}\tau_{\mathrm{md}}}{k_{\mathrm{B}}T^2} = 10000$,(iii) thermal connection between crystal and polymer $\frac{\kappa_{\mathrm{int}}^{\mathrm{CryPoly}}\tau_{\mathrm{md}}}{k_{\mathrm{B}}T^2} = 500$, (iv) directly connected bonds $\frac{\kappa_{\mathrm{int}}^{\mathrm{intra}}\tau_{\mathrm{md}}}{k_{\mathrm{B}}T^2} = 100000$. We apply an external current, $\frac{\mathrm{rnecurrent}k_{\mathrm{B}}T}{\tau_{\mathrm{md}}\sigma^2} = 100$. Figure 4.19 shows the resulting temperature profile in a steady-state condition, because the system is created symmetrically, the plot of the temperature profile has been reduced to one half only. To calculate a local temperature, the inverse temperatures of each particle within the slab, width $\delta x/\sigma = 0.2$, are averaged.

Discussion According to the underlying structure, one observes two independent thermal conductivities - the crystal's and polymer's thermal conductivity. The crystal (C) and polymer (P) regions are separated by the dashed green lines. In applying an external energy current, the system is driven far from equilibrium such that, in an unfavourable case one observes a non-physical behaviour of the temperature at an interface. The second law of thermodynamics dictates that a hot and a cold particle, with temperature $T_1 > T_2$, never reaches the condition $T_1 < T_2$ but $T_1^{\mathrm{equil.}} = T_2^{\mathrm{equil.}}$. If the difference of specific heat between two particles is large and the internal thermal relaxation is high, this law can be violated. From a microcanonical point of view, one could argue that energy that is transferred from a heavy to a light particle increases momenta, too. In consequence, the lighter particle has a higher mobility and kinetic temperature increases.

In the **eMC** scheme, depending on the time discretisation, a portion of the energy from the hot to the cold particle is transported, but this can evoke a temperature condition where temperatures have been crossed, i.e., in an update step, the cold particle becomes hotter than the hot particle was before. Hence, we introduced an

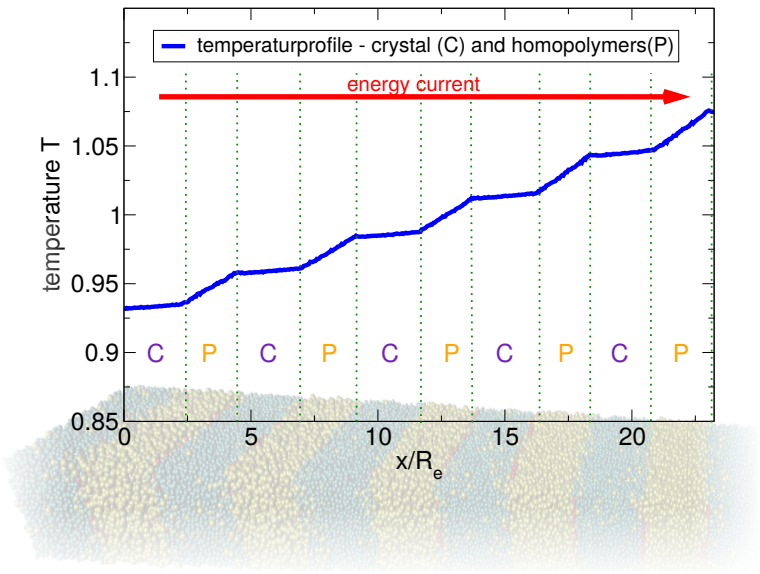

Figure 4.19 External energy current (red) applied to a mixture of homopolymers (P) $N = 16$ and simple cubic crystals (C), lattice constant $a = 0.5$, results in a steady-state temperature profile (blue). Internal specific heat capacities of each segment are $c_v^{\mathrm{Cry}}/k_{\mathrm{B}} = 5000$, $c_v^{\mathrm{Poly}}/k_{\mathrm{B}} = 500$. Internal thermal relaxation constants are $\kappa_{\mathrm{int}}^{\mathrm{Cry}} = 10000$, $\kappa_{\mathrm{int}}^{\mathrm{Poly}} = 1000$, $\kappa_{\mathrm{int}}^{\mathrm{intra}} = 100000$ $\kappa_{\mathrm{int}}^{\mathrm{Cry-Poly}} = 500$ and the applied current $\frac{\mathrm{rnecurrent}\tau_{\mathrm{md}}\sigma^2 A}{k_{\mathrm{B}}T} = 100$.

additional condition, $T_1^{\mathrm{old}} \leq T_2^{\mathrm{old}} \Leftrightarrow T_1^{\mathrm{new}} \leq T_2^{\mathrm{new}}$, which fulfils detailed balance and inhibits a crossing of temperatures.

In fig. 4.19, we cannot determine an additional thermal resistance at the interface. Firstly, the interface, which is visualised by the green dashed lines, is not sharp but very soft and smooth, because polymers are small $N = 16$ and the packing density of the crystal is not very high, too. In consequence, polymers can penetrate the crystal structure and the inter-facial effect is blurred, because of fluctuations of the interface position in the y and z plane. Secondly, the coupling between the crystal's particles and polymers is not significantly smaller than the internal thermal relaxation constant of non-bounded polymers. The contrast of specific heat of the two phases also can be motivated with a selective inclusion of silica or gold nanoparticles, in one phase [76], [77]. Also the description of crystal is ambitious: an ordered cross-linked network of polymers would be a more appropriate description, which also fits to studies on thermal properties of cross-linked polymers [78]. In these studies it was shown that cross-linked polymers have an increased thermal conductivity.

4.7 Thermal conductivity without internal DoFs

In the previous section we applied **eMC** to homo, diblock, and star polymers. Transport properties have been mainly influenced by the internal **DoF**s. Therefore we want to investigate thermal transport in systems without internal degrees of freedom. Hence, the following simulations are done without the **eMC** scheme or any other thermostat.

4.7.1 Thermal conductivity of a uniform fluid

We use the **RNEMD** technique again to drive the system into a steady-state condition. The energy current is applied to the particles' momenta. The system is treated microcanonically, thus, thermostats are completely switched off. Momenta are initialised with Maxwell-Boltzmann-distributed velocities. Hence, the system's global temperature, which is treated in reduced units $k_BT = 1$, is defined by the system's kinetic energy. Temperature is defined locally for each slab of thickness $\Delta x\sigma^{-1} = 1$, too. The dimensions are $L_x\sigma^{-1} = 40; L_y\sigma^{-1} = L_z\sigma^{-1} = 5$, the system's boundaries are periodic, and it contains $N = 15008$ particles. The density is $\rho\sigma^3 = 15$. System is considered in two cases. In the first case, the system contains monomers. In the second case, the system is comprised of homopolymers, discretised in $N = 32$ beads, and averaged bond length $b = 1 = \sigma$. Fig. 4.20 represents the macroscopic thermal conductivity as a function of isothermal compressibility, i.e., the soft interaction parameter, for the two mentioned cases. The thermal conductivity of the monomer system decreases for higher isothermal compressibilities whereas the thermal conductivity of the homopolymer system increases.

Discussion The thermal conductivity of monomers at small v_{ij} is driven by the mobility of the particles. If the soft interaction is small, the friction vanishes. Hence, the particles have a higher mobility and ballistic characteristics, which increases transport of energy. If the soft interaction is increased, the ballistic part is decreased. Hence, transport of the fluid is dominated by diffusive characteristics. Polymers already have a low ballistic regime, because it is suppressed by the bond connectivity. Hence, their transport characteristics are dominated by diffusion. Comparing monomer and polymer system for high soft interaction reveals a higher conductivity of the polymer system. Hence, polymers have a more directed transport, because intramolecular connections are strong and have a higher frequency than non-

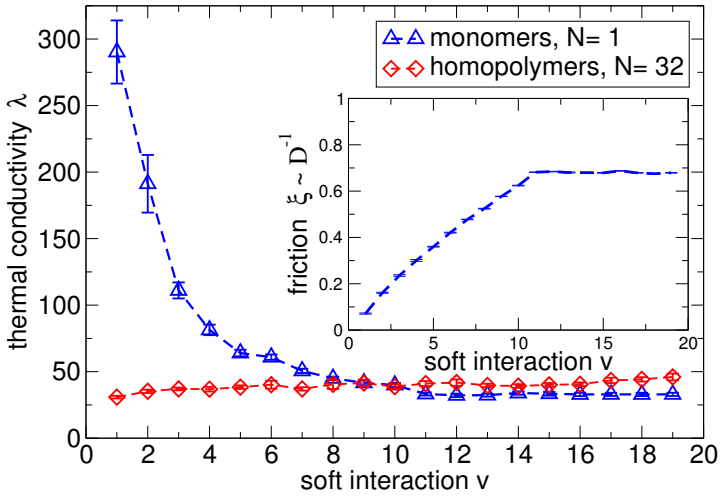

Figure 4.20 Macroscopic thermal conductivity, λ, of a soft fluid, without internal **DoF**, represented by a soft repulsive interaction v. The fluid is comprised of monomers (blue) or homopolymers (red). Inset represents the friction of the monomer system as a function of the soft interaction parameter.

bonded interactions. Hence, intramolecular connections induce a more deterministic part of kinetic energy, which is transported along segments. The length of this directed transport channel is higher than the random scattered part in the monomer system.

In sec. 4.3.2 we discussed the influence of the degree of polymerisation and intramolecular thermal conductivity on the macroscopic thermal conductivity using **eMC**, i.e., including internal **DoF**s. We discussed that the order of magnitude, which is in between intra- and inter-molecular connectivity, κ_{int}, can be motivated by experimental results. But a justification within our soft coarse-grained model is also possible, because we get at high soft interaction parameter, $v = 19$, and an increase of macroscopic thermal conductivity ~ 1.5 between systems comprised of monomers or polymers, respectively.

4.7.2 Thermal resistance of a mixture of soft monomers

Now, we continue to thermal transport of a soft fluid composed of two monomer types. The soft interaction of these monomers is chosen in such a way that the system macroscopically phase separates. This is accompanied by two interfaces

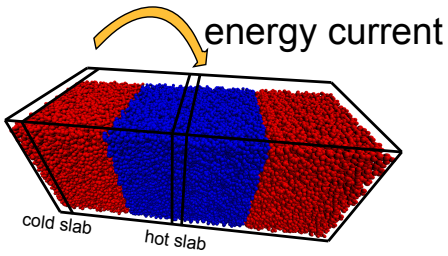

Figure 4.21 Soft fluid composed of two types. Types are distinguished in their soft interaction parameter v_{ij}. The two types macro-phase separate in such a way that two interfaces are formed. An energy current is always applied to the slab that is centred in the blue phase, red respectively.

between the phases if periodic boundary conditions are applied in each direction. If an energy current is applied to this system, the interface creates a resistance. Observing this resistance, we compare this qualitatively with the overlap of the **DoS** of the pure bulk systems, sec. 4.8.2. Similar strategies have been applied to Lennard-Jones fluids [40] and Lennard-Jones super-lattices [30]. The system is microcanonical such that temperature will be defined by the particles' kinetic energy. Energy is transported between a hot-slab and cold-slab region by rescaling particles' momenta. We use this approach, because it reduces the fluctuations in the temperature profiles. Per contra a normal swapping routine: (i) find the hottest particle in the cold slab (ii) find the coldest particle in the hot slab (iii) swap their corresponding momenta. This standard routine has a lot of fluctuations, which requires increased statistics, and it breaks down if the energy of the cold particle in hot slab is larger than the hot particle in the cold slab.

The system contains $N = 15000$ particles, half of which are type A and type B, respectively, fig. 4.21. The size of the system is $L_x\sigma^{-1} = 40; L_y\sigma^{-1} = L_z\sigma^{-1} = 5$ and is periodic, and the size of a slab is $\Delta x\sigma^{-1} = 1$. The soft interaction parameter is varied between $v = 1$ and $v = 7$ in steps of 1. This parameter range yields 7×7 possible configurations. The incompatibility between A and B monomers is set to $v_{\mathrm{AB}} = \left(\frac{v_{\mathrm{A}}+v_{\mathrm{B}}}{2} + 4\right)$. The choice of this value enables the system to relax in a macro-phase separated state. As a result of macro-phase separation two densities are observed. These two bulk densities are located in the red- and blue-coloured region, fig 4.21. The pressure and the density of the system are balanced. Hence, the local densities of phase A and phase B depend on the isothermal compressibility or soft interaction parameter v_{A}, v_{B}, respectively. Figure 4.22 represents the densities of bulk region A (left) and bulk region B (right), in the presence of a small thermal current $j = 0.25 \cdot A \cdot \mathrm{d}t$. The thermal current is applied via a **RNEMD** scheme to explicit **DoF**. Hence, the density in bulk region A is observed as a function of soft interaction parameters, v_{A} and v_{B}, of both phases. The densities in the configuration:

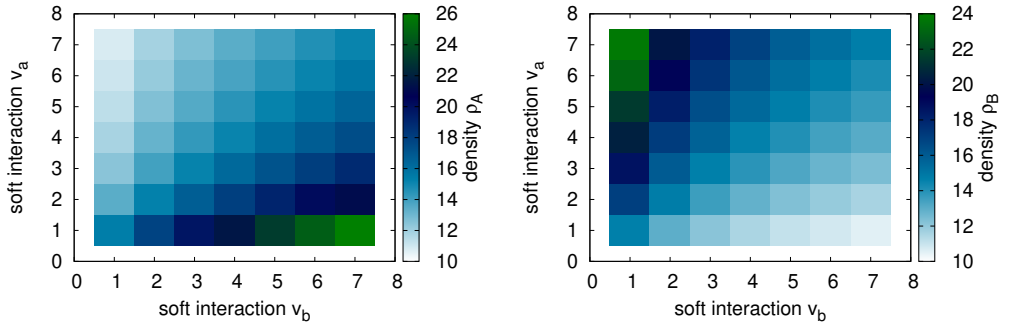

Figure 4.22 Colour code indicates the averaged density of the phase, as a function of the soft interaction parameters v_a and v_b. (left) chart indicates A phase, which includes the cold slab. (right) chart indicates the B phase which includes the hot slab.

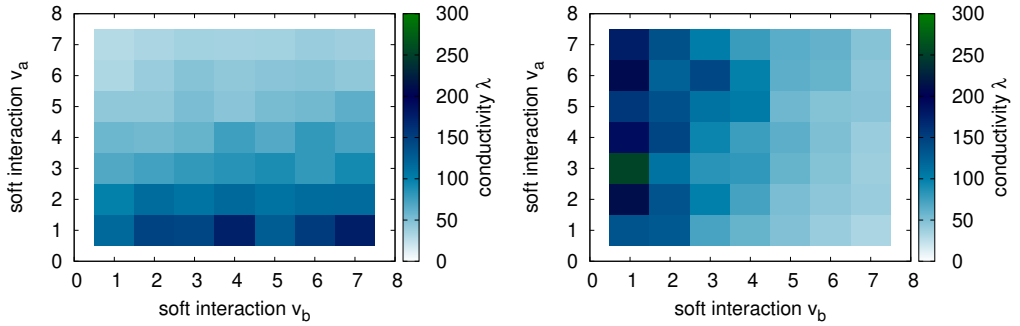

Figure 4.23 Colour code indicates the thermal conductivity of the phase A (left) and phase B (right), as a function of the soft interaction parameters v_{A} and v_{B}. The A phase includes the cold and the B phase includes the hot slab. Two trends can be identified: the thermal conductivity decrease for higher v (which quantitatively agrees with behaviour observed in pure monomer systems), and higher densities exhibit higher thermal conductivity, cf. fig. 4.22.

$v_{\mathrm{A}} = 1$ and $v_{\mathrm{B}} = 7$, $v_{\mathrm{A}} = 7$ and $v_{\mathrm{b}} = 1$, are not symmetric, because the phase A includes the hot and phase B the cold slab, which are used to create the external thermal current. At a constant finite current, the system forms a temperature profile in a steady condition. Fig. 4.23 presents thermal conductivities that have been observed by temperature profiles in steady-state condition again. We calculate the temperature jump that emerges at the interface in the steady-state temperature profiles. Since the system has two interfaces, we average the temperature jump. The temperature jump of a system is observed under two conditions: A→B and B→A depending on the direction in which the current is applied. The linear resistance, R, of the interface is independent of the current j. Here c is any constant, which

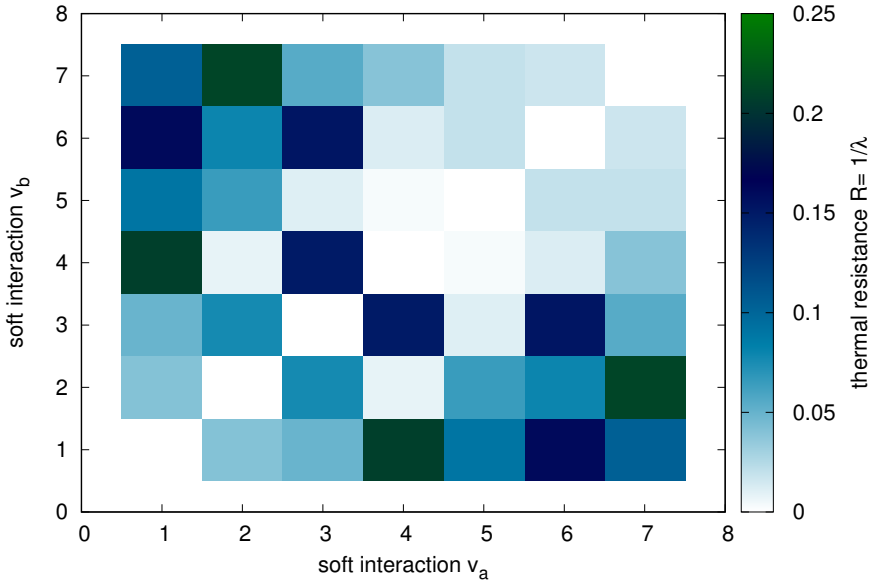

Figure 4.24 Thermal resistance of an interface formed by a binary mixture of A and B monomers. The colour scale indicates the thermal resistance, R, from zero to one via the colour gradient from white over blue to green. The thermal resistance has been extrapolated to zero current, cf. eq. (4.5). If phase A and B have the same soft interactions, the resistance of the interface vanishes. Vice versa, if the difference in v_a and v_b is high, resistance is increased. The error of the Resistance is about 20 percentage of the total value, which inhibits more detailed evaluation.

denotes the resistance which depends on the current applied to the system.

$$\left.\begin{array}{ll} \frac{\Delta T_{\mathrm{A}\to\mathrm{B}}}{j_{\mathrm{A}\to\mathrm{B}}} & = R + c \cdot j_{\mathrm{A}\to\mathrm{B}} \\ \frac{\Delta T_{\mathrm{B}\to\mathrm{A}}}{j_{\mathrm{B}\to\mathrm{A}}} & = R - c \cdot j_{\mathrm{B}\to\mathrm{A}} \end{array}\right\} \Rightarrow R = \frac{\Delta T_{\mathrm{A}\to\mathrm{B}} - \Delta T_{\mathrm{B}\to\mathrm{A}}}{2 j_{\mathrm{A}\to\mathrm{B}}} \tag{4.5}$$

Adding up the two left equations yields a resistance of the interface independent of the current that is assumed symmetrically $j_{\mathrm{A}\to\mathrm{B}} = -j_{\mathrm{B}\to\mathrm{A}}$. The resulting resistance of the interface, R, is represented by fig. 4.24. The figure suggests that the thermal resistance increases for a mismatch between soft interaction parameter v_{A} and v_b.

Discussion High differences in soft interaction parameters dramatically increase the densities in phase A and B, but staying in the restriction of the soft model this cannot be avoided. In general, high densities allow more possible interactions, hence the transport of energy can be faster. The thermal conductivity of a pure monomer system, in which the soft interaction parameters are small, is mainly

driven by friction, cf. fig. 4.20 (inset). Hence, in fig. 4.23 the same dependency can be observed: decreased thermal conductivities for higher interaction parameters. In contrast, higher densities increase thermal conductivity.

4.8 Phonon properties - microcanonical system

In general, studying phonon properties of fluids is quite challenging, because typically only longitudinal waves can be observed. If there are phonon vibrations in a polymer melt, they are local, decay very fast, and one expects an incoherent behaviour with respect to transport properties. The first part of this section studies the properties of a system of soft monomers. From here, we will go on to polymer blends. Finally, we outline properties of a simple cubic crystal and homopolymers to investigate transport properties of propagating modes induced by the crystal through the polymer melt.

4.8.1 Quench a soft MD simulation

The most challenging part before the harmonic matrix, i.e., the Hessian matrix, can be calculated and diagonalised, is to quench the system to a local minimum. Only if the quenching to a local equilibrium is successful, can stable modes be observed. It is a good criterion to check a quench procedure via monitoring the forces, because, in a local equilibrium, the gradient of the potential energy has to be zero.

Steepest descent We quench the system with the steepest descent method, which is an iterate first-order optimisation algorithm. Therefore, we introduce a viscosity in arbitrary units, which damps the forces and causes a local minimisation of the local forces. To quench the system in a local minimum, one sets the kinetic energy to zero and than applies a high damping rate, which can be understood as an intrinsic viscosity.

$$p_{\mathrm{i}}^{\alpha} = \varepsilon_{\mathrm{damp}} \cdot F_{\mathrm{new}}^{\alpha} = \frac{\varepsilon_0 \cdot \mathrm{d}t}{v_{\mathrm{ij}}} \cdot F_{\mathrm{new}}^{\alpha} \tag{4.6}$$

$$x_{\mathrm{i}}^{\alpha} = x_{\mathrm{i,old}}^{\alpha} + \frac{p_{\mathrm{i}}^{\alpha}}{m_{\mathrm{i}}^{\alpha}} \mathrm{d}t. \tag{4.7}$$

$\alpha = \{x, y, z\}$ addresses the index of the dimension. i is the particle's index. p is the momentum and x the position. $\varepsilon_{\mathrm{damp}}$ is the damping constant $\ll 1$. Eq. 4.6 means

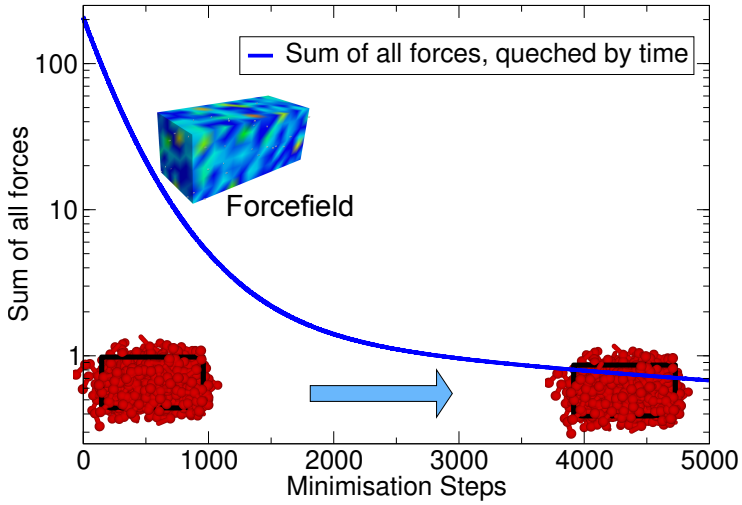

Figure 4.25 A small system is quenched down to a local minimum. In the initial step, kinetic energy is set to zero, and a viscous force damps the system, $L\sigma^{-3} = 4 \cdot 4 \cdot 8$, particles $N = 1280$. The damping, $\varepsilon_{\text{damp}} = 0.001$, is strong, hence, the system remains in a local minimum and not a global one, snapshots red.

that we follow the gradient to minimise the local potential. It is important that the minimisation of the system is very fast, and that the intrinsic viscosity induces a high damping. Otherwise, the system's local equilibrium is being undertaken and it ends up in a global minimum, which does not conserve the conformational structure of the particles. Furthermore, the strength of the potential influences the quenching procedure. Hence, the damping constant $\varepsilon_{\text{damp}}$ is scaled by time the increment dt and the largest soft interaction parameter that occurs in the system. The particles will optimise their local structure into a local minimum. Hence, the sum over all absolute forces allows an estimate of the quality of the local quench. Fig. 4.25 represents a small system that has been quenched. The initial system (coloured in red) is quenched and the local forces are optimised such that the sum over all absolute forces changes to zero. Finally, the quenched structure is quite similar to the initial one, but the initial forcefield coloured in shades of blue is minimised to uniform blue.

Build up of entries of the harmonic matrix We explained how a system is quenched to a local minimum by minimisation of the gradient of the forces. To apply a harmonic matrix to the quenched system, we postulate for the system following the properties:

- particles have a local equilibrium position,

- each normal mode acts like a harmonic oscillator and the centre of mass does not move,
- the normal modes do not interact,
- quenching the system is an instantaneous minimisation of the force fields.

Hence, we calculate the second derivatives of the pairwise bonded and non-bonded potentials from the structural information of the system. Non-bonded potentials are harmonic and soft repulsive, bonded interactions are harmonic, too, but the potential is shifted such that the minimum is at averaged bond distance $b\sigma^{-1} = 1$. This potential has also been applied in the quench. Bonded interactions are applied beyond the cut-off distance. The matrix has the size: dimension $\times$ number of particles, which results in n, m$= 3 \times N$. Each entry of the matrix $M_{\mathrm{n,m}}$ is indexed with n and m. These indices imply the direction x, y, z and the index of the particle i,j. Hence, we observe different forms of the matrix entries.

1. Same direction, same particle:
   $M[\mathrm{n(i},x),\mathrm{m(i},x)]$, $M[\mathrm{n(i},y),\mathrm{m(i},y)]$, $M[\mathrm{n(i},z),m\mathrm{(i},z)]$,
2. different direction, same particle:
   $M[\mathrm{n(i},x),\mathrm{m(i},y)]$, $M[\mathrm{n(i},x),\mathrm{m(i},z)]$, $M[\mathrm{n(i},y),\mathrm{m(i},z)]$,
3. same direction, different particle:
   $M[\mathrm{n(i},x),\mathrm{m(j},x)]$, $M[\mathrm{n(i},y),\mathrm{m(j},y)]$, $M[\mathrm{n(i},z),\mathrm{m(j},z)]$,
4. different direction, different particle:
   $M[\mathrm{n(i},x),\mathrm{m(i},y)]$, $M[\mathrm{n(i},x),\mathrm{m(j},z)]$,$M[\mathrm{n(i},y),\mathrm{m(j},z)]$.

All pairwise potentials are represented within the Hamiltonian, $\mathcal{H}\{\mathbf{r}\}$, where $\mathbf{r}$ represents all particles' spatial positions. The number of neighbours that are coupled by a potential is $\#P$. Based on the different types of matrix entries, we can define the general forms,

1. $M[\mathrm{n(i},x),\mathrm{m(i},x)] = \frac{\partial^2 \mathcal{H}\{r\}}{\partial x_i \partial x_i} = \sum_{\mathrm{j}}^{\#\mathrm{P}} \frac{\partial V(r_i,r_j)}{\partial x_i \partial x_i}$,
2. $M[\mathrm{n(i},x),\mathrm{m(i},y)] = \frac{\partial^2 \mathcal{H}\{r\}}{\partial x_i \partial y_i} = \sum_{\mathrm{j}}^{\#\mathrm{P}} \frac{\partial V(r_i,r_j)}{\partial x_i \partial y_i}$,
3. $M[\mathrm{n(i},x),\mathrm{m(j},x)] = \frac{\partial^2 \mathcal{H}\{r\}}{\partial x_i \partial y_i} = \frac{\partial V(r_i,r_j)}{\partial x_i \partial y_i}$,
4. $M[\mathrm{n(i},x),\mathrm{m(j},y)] = \frac{\partial^2 \mathcal{H}\{r\}}{\partial x_i \partial y_j} = \frac{\partial V(r_i,r_j)}{\partial x_i \partial y_j}$.

Here x, y, z indicate the directions and i and j indicate the particle's id. Hence, to get the other terms of the harmonic matrix, x can be replaced by y and z. The explicit form of the derivatives can be found in appendix, sec. 6.6. This formalism, which was enumerated, is applied to particles' potentials. The matrix entries, which emerge by the bonded potentials are predictable from the bond structure, i.e., they are independent from the microscopic configuration, whereas the non-bonded interactions have to be applied to the underlying configuration. Hence, in case of non-bonded interactions, one has to consider N^2 possible interactions which are limited by the cut-off distance of the bonded potential only[11]. To check if a matrix has been calculated in the right way, e.g., the matrix has to be symmetric, and the sum of each row and column has to be zero.

4.8.2 Thermal resistance of a soft fluid mixture by DoS

We will investigate the density of states of a soft system and vary the isothermal compressibility. The system is contains $N = 5145$ particles, has cubic dimensions $V\sigma^{-3} = 7 \times 7 \times 7$, and an averaged number density of $\rho\sigma^3 = 15$. The non-bonded interactions are scaled from $v = 1$ up to $v = 7$. We determine the density of states by harmonic matrix approximation. Hence, the system is quenched first. The quench follows the strategy explained in sec. 4.8.1. But we want to expose the main assumptions: to apply the harmonic matrix approximation the forces are minimised first. Hence, the system is quenched firstly by setting the kinetic energy to zero and secondly by applying a high damping rate - intrinsic viscosity controlled. For all systems, the time increment is $\mathrm{d}t = 0.0001$ and the damping is $\varepsilon_0 = 1$. According to different soft interactions, the total damping is between $\varepsilon_{\mathrm{damp}} = [0.000015 : 0.0001]$. The quench of the system is done for 10^5 steps.

Finally, the harmonic matrix is calculated from the quenched structure. This matrix is diagonalised via the Intel®MKL library, which allows us to determine the spectrum of eigenvalues, λ_{i}. Taking the square root of all eigenvalues, $\omega = \mathrm{sign}(\lambda)\sqrt{\mathrm{abs}(\lambda)}$, gives rise to a frequency spectrum, **DoS** $D(\omega)$ respectively. Taking the $\mathrm{sign}(\lambda)$ and the absolute values enables to show negative frequencies, i.e., complex modes too. These modes always appear if the system has not been quenched to an accurate local equilibrium state. They represent unstable modes that drive the

[11] Technically, calculating the entries for the harmonic matrix can be accelerated, because the system is already divided in boxes that have the size of to cut-off distance. Thus, in three dimensions, one has to consider $27 - 1$ neighboured boxes only as well as the box in which the particle is located.

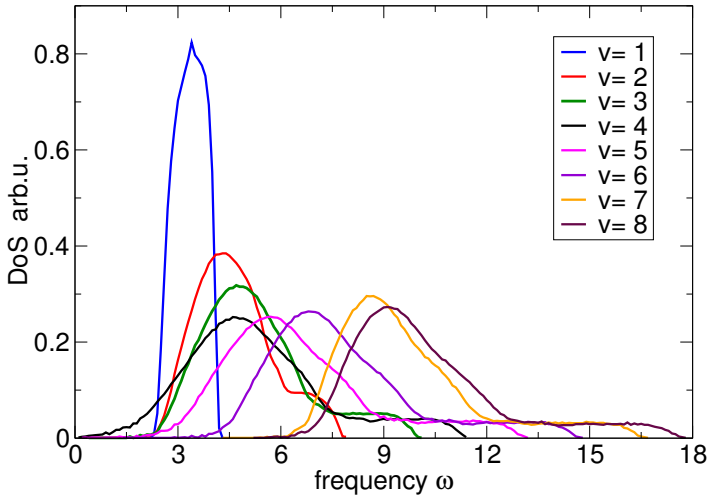

Figure 4.26 DoS of a soft fluid composed of monomers with bulk density $\rho_0\sigma^3 = 15$. The system was quenched by 10000 steps via steepest descent method to a local minimum, $\mathrm{d}t = 0.001$, $e_0 = 1$. Afterwards, the harmonic matrix has been calculated and diagonalised via Intel®MKL library. Eigenvalues' square roots have been collected in a histogram, which represents the **DoS** of the system.

system to its new local minimum [79]. Fig. 4.26 represents the **DoS**, which was calculated by the explained procedure, for various interaction parameter. In the small frequency regime of each **DoS**, a quadratic scaling ω^2 might be identified. Maxima in the **DoS** qualitatively could be explained by scaling of maximum frequency of Debye model, $\omega_\mathrm{D} = c_\mathrm{s} \cdot \left(\frac{6\pi^2 N}{V}\right)^{\frac{1}{3}}$, eq. 2.25. The velocity of sound, c_s, or velocity of a propagating density peak, respectively, linearly increases by the isothermal compressibility $K_\mathrm{iso}N$, cf. sec. 4.8.3. The quenching procedure becomes easier for higher soft interaction parameter. If the soft interaction becomes stronger, the energy barriers of local minima increase, become localised and sharper. Therefore, the local minima are shaped more precisely, and also higher frequencies are observed. Frequencies, i.e., the peak of the **DoS**, also increase by the density, appendix fig. 6.4.

The resulting **DoS**s are used to estimate a resistance at an interface and the transmission coefficient respectively. A vibrational mismatch at the interface can be formulated in claiming that only frequencies that propagate in both bulk systems, can overcome the interface. Other remaining frequencies are reflected by the interface and stay in the bulk material. Fig. 4.27 represents two **DoS**s. The overlap A is

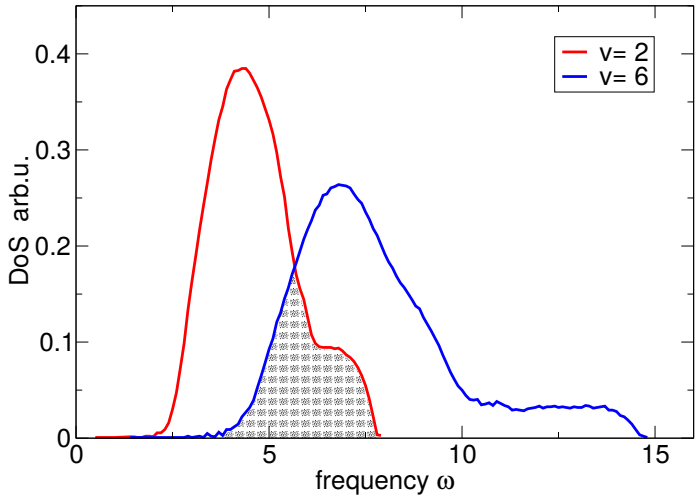

Figure 4.27 The overlap (shaded black) of two bulk **DoS**s for $v = 2$ and $v = 6$, cf. fig. 4.26, enables the estimation of resistance that is induced by a vibrational mismatch at the interface.

shaded black and characterises the modes, which can propagate in both systems. All possible combinations are shown in fig. 4.27. We define the thermal resistance by the part of modes that are reflected by a mismatch, and the resistance is crudely estimated as $R = 1 - A$. If two identical bulk systems are in contact they are indistinguishable. Hence, the approach to resistance, R, does not considers structural effects of interfaces, such that the diagonal is zero (shaded white), fig. 4.28. Systems that are not identical have a mismatch, hence there is a resistance. The resistance is maximised by increasing the deviation of interaction. The overlap of $v = 1$ and $v = 8$ is approximately zero. Hence, the resistance of the interface becomes 1, i.e., 100 percent.

Discussion The most challenging part of calculating a **DoS** is the quench. It can take multiple runs to observe a successful quench, because the system has imaginary modes left. A disadvantage of the framework is that we could not find a criterion that guarantees a quench in a stable local equilibrium before the **DoS** had been calculated. These calculations can be performed faster by using accelerator cards, i.e., Nvidia Pascal or Intel Knights Landing, but finally this is the most

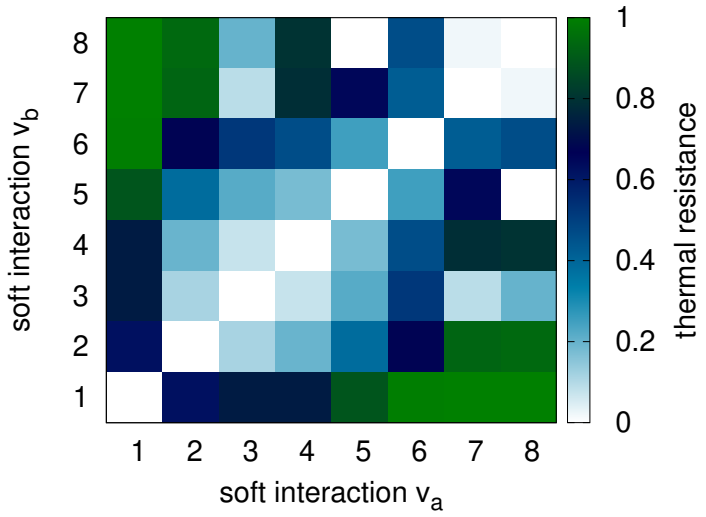

Figure 4.28 Thermal resistance observed by overlap, A, of **DoS** of bulk systems. The thermal resistance is defined by the part of modes, which are reflected by a mismatch, and the resistance is crudely estimated by $R = 1 - A$

time-consuming part [12].

As already mentioned, increasing the potential allows us to quench the system easier, because the *landscape* of the potentials becomes sharper and the local minima are better separated. In the quench procedure, one also has to consider small time increments, because too large increments are insensitive for local equilibrium positions. Hence the damping constant was chosen as a combination of time increment, interaction constant of potentials, and an additional damping constant.

4.8.3 Density waves in a homopolymer melt

The system is composed by linear harmonic chains, which interact via a soft potential, sec. 3.5.2. The strength of soft interactions is given by the inverse isothermal compressibility κN. The system is treated microcanonically without making use of thermostats. Hence, we set a kinetic energy such that the averaged kinetic temperature is $k_B T = 1$, cf. eq. 3.53. The system is considered to be three-dimensional with periodical boundary conditions. Nevertheless, we will focus the analysis on the one-dimensional case along the x-axis and average over the other

[12] Beside the computing, it is also challenging to handle the size of the matrices, in the context of storage and memory allocation on GPUs.

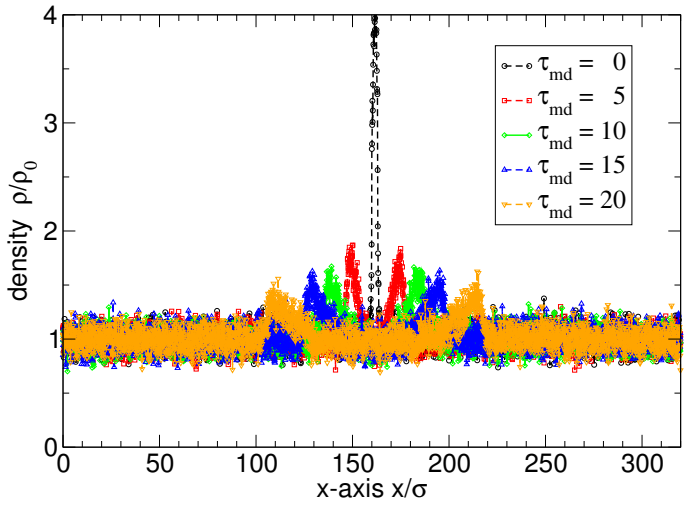

Figure 4.29 Density of a homopolymer $\rho_0\sigma^3 = 10$ for different time steps τ_{md}. At τ_{md}, densities have been increased by a factor of 4 at position $L_{\mathrm{x}}/2 \pm \Delta x/2$. The maximal amplitude of the peak $A_{\mathrm{peak}}(t)$ propagates through the system along the x-axis.

directions (y, z) to improve statistics. We divide the system into small Δx slabs according to the x-axis and measure the density by time. The starting point is a system with equally distributed densities, $\rho_0\sigma^3 = 10$. In the middle of the box at position $L_{\mathrm{x}}/2 \pm \Delta x/2$, the densities are instantaneously increased by a variable factor. Technically, we write a configuration file and add a specific number of particles in the area that was specified. The velocities of the new particles are drawn from a Maxwell Boltzmann distribution with $k_{\mathrm{B}}T = 1$. Of course, this can be understood as non-physically, - but particles are soft and the overlap does not induce singularities. While unrealistic conditions can be created, a few integration steps are adequate so that these overlapping effects can be fully compensated. Starting from this point, time evolution of the density profile can be examined whithout any difficulties. Such a density profile at different times is shown in figure 4.29. In this example the equilibrium density of the homopolymer melt was rescaled to 1 by the averaged density $\rho_0\sigma^3 = 10$. Hence, at time $t = 0$ the density at $L_{\mathrm{x}}/2 \pm \Delta x/2$ has been increased by a factor of 4 ($\Delta x\sigma^{-1} = 1$). The density peak splits in two parts and propagates through the system. In the course of propagation of the peak's amplitude is damped. Than, we can conclude that a longitudinal density wave in a soft, coarse-grained melt of homopolymers has damped ballistic behaviour. The position of peaks as a function of time allows us to extract the velocity of the peaks,

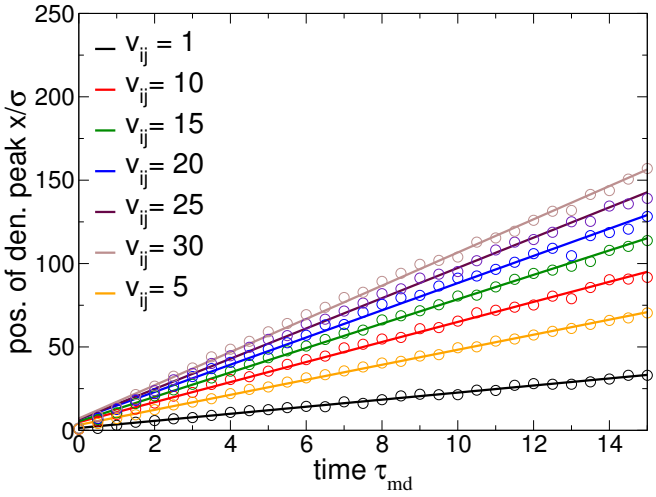

Figure 4.30 Position of density peaks along z-axis as a function of time τ_{md}. The position is averaged over the two peaks. Compare also to fig. 4.29.

fig. 4.30. We observe that the propagation of the peaks is constant and apply a linear fit to get the velocities of the peak. The velocities of the density peaks depend on the isothermal compressibility parameter $\kappa_{\mathrm{iso}}N. \propto v_{\mathrm{ij}}$. Figure 4.29 shows that the density peaks are damped. This damping is induced by local dissipation via non-bonded and bonded potentials. The damping of the amplitude can be described by an exponential decay.

$$A_{\mathrm{peak}}(t) = A_0 \cdot \exp(-t\tau). \tag{4.8}$$

The result of the fit is shown in figure 4.31 (blue).

Discussion We conclude that the maximum of the peak has a higher damping at low isothermal compressibility or v_{ij} respectively. If the isothermal compressibility is increased we observe that the decay time is lower and the density peaks can propagate through the system for a longer time. However, instead of a diffusive behaviour the created pressure wave splits into two parts and propagates as a longitudinal wave through the system. If the two pressure waves collide against each other they are reflected, too. The damping of the pressure wave is constant that an exponential decay of the amplitude is observed. The result that pressure waves propagate in a polymer melt has formed a concept that we want to outline in the following subsection.

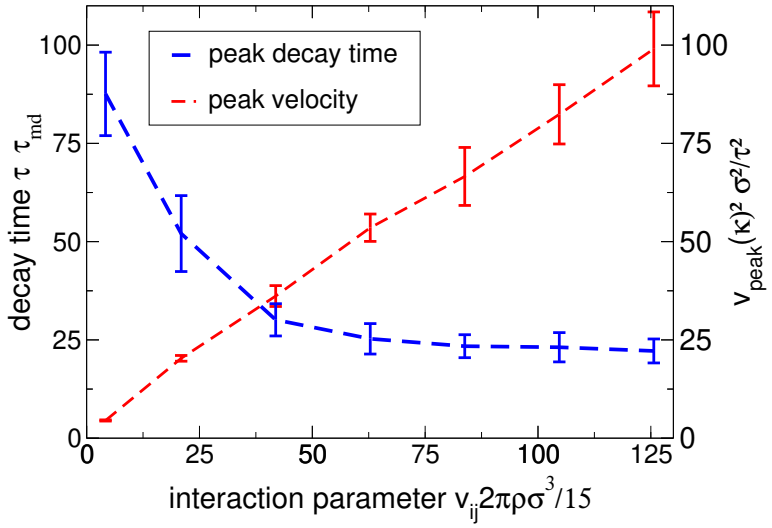

Figure 4.31 Red curve is the decay of the density peak's amplitude as a function of the isothermal compressibility, cf. eq.(4.8). Blue curve results from a linear fit of figure 4.30 varying the function of isothermal compressibility.

4.8.4 Outlook on homopolymer melts and simple cubic crystals

In section 4.6, a composite system, which consists of an alternating structure of homopolymers and soft cubic crystals, has been presented. This composite system is used again, with the difference that all contributions of internal **DoF**s and **eMC** are left out and the system deals only with explicit **DoF**s. In this system, propagating of modes that are generated in a soft crystals are studied. The system is tested to answer the following question: do the polymers in between two soft crystals have a range in frequency space that permits a better propagation of a mode. Here, the second crystal is used to detect the modes that have been created in the other soft cubic crystal and propagated through the polymer melt. Figure 4.32 summarises the setup that is used. An alternating structure of polymers and soft cubic crystals is putted into a periodical system. In the first crystal, a mode is created, whereas the second crystal detects the mode. A possible selective mechanism that confirms the hypothesis, might be found in bond vibrations that allow a better propagation.

In a first test, the response of the second crystal has been tested. Hence, the momentum of the centre of mass of the first crystal has been exited by a constant external frequency. This created a longitudinal wave, which exponentially decayed in the polymer melt. Therefore, the distance between the two crystals, which is

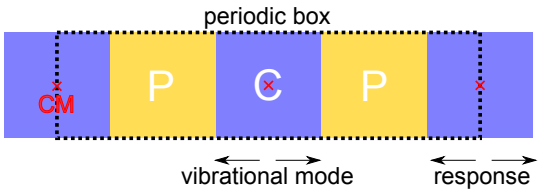

Figure 4.32 The system is comprised of soft repulsive harmonic bonded particle (light blue), which form a crystal-like structure, and homopolymers ($N = 16$, averaged bond distance of $b = 1\sigma$). In one of the crystals, a vibrational mode is inserted. The mode propagates through the homopolymer melt and is measured in the second crystal.

filled with polymers, has been chosen so that the propagating wave is not completely damped. The external frequency, which is inserted to the crystal's momentum, is generated by a modulation of a sine $\sim \sin(\omega t)$, with $\omega = \frac{2\pi}{\tau_{\text{md}}}$. Assuming that some frequencies propagate better through the polymer melt, one should obtain a higher amplitude of the induced frequency in the second crystal that detects the amplitudes. But no specific mode of the polymer melt that increases/reduces transport behaviour that is observed by the second crystal has been observed yet.

4.9 Results on azobenzene photo switches

In section 4.5, we motivated the structural change of the solubility of the star polymers by cis-trans azobenzene photo switches. Azobenzene is a chemical compound which consists of two phenyl rings that are linked by a double-bond of nitrogen. The change of structure and solubility via an interaction with light was first observed by Hartley in 1937. He found the cis-form of the azobenzene [80]. Fig. 4.33 shows the chemical structure of azobenzene in the trans- and cis-state. The cis-state is an excited state that can be obtained by an UV light. The other way around, the trans-state is reached by thermal noise or the backward reaction of an incident photon. Even if the structure returns to stable trans-states by thermal noise, structures created by an exited cis-state are stable for hours up to days [77]. Photo switches are good candidates to induce a structural change, because both of their reversible isomerisation and change of dipole moment. Recent experiments have shown that an in-situ light-controlled switching of a block-copolymer morphology during dip-coating of a thin film is possible [81]. Figure 4.34 shows two **AFM** images of phases emerged by dip-coating. The coating was performed under two conditions (i) in the dark (left image) and (ii) excited to the cis-state (right image) by UV light. Here, one observes either a lamella or a hexagonal phase. Similar

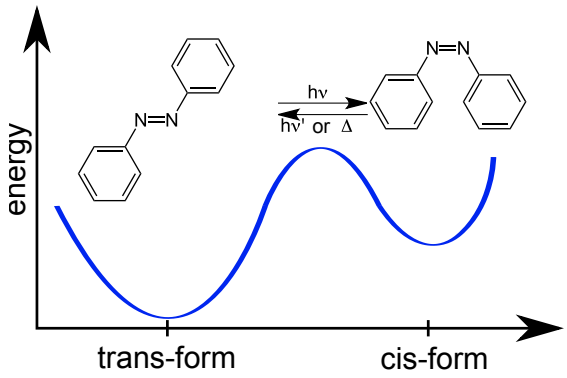

Figure 4.33 Azobenzene is a chemical compound which consists of two phenyl rings, which are linked by a double bond of nitrogen. An incident photon can induce a change of morphology and shift the azobenzene to an exited metastable cis-state (forward $\lambda \approx 370$[nm], backward $\lambda \approx 400$[nm]). Azobenzene can return down to the ground state again by thermal noise Δ or an incident photon.

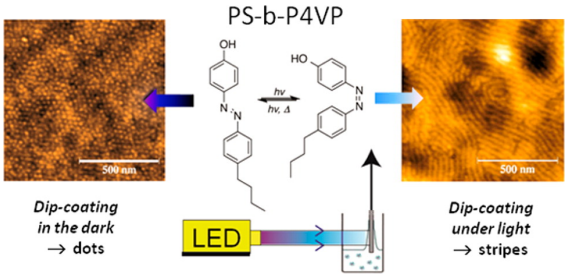

Figure 4.34 In-situ light-controlled switching of a block copolymer morphology during dip-coating of a thin film. Reprinted with permission from ACS Macro Letters, [81], Copyright (2002) American Chemical Society.

experiments have been done by Hübner, who investigated different phases of a PAzoPMA-b-PBA in trans- and cis-state [77].

Photo switches have also been investigated by atomic force probe experiments to motivate light-powered molecular machines [82]. In this atomic force probe setup they created a polymer that consists of azobenzene-repeating units. Additional linkers at the ends have been added to fix the polymer to the atomic force microscopy tip and to the substrate. The substrate itself is a glass, which hosts a TIR (total internal reflection) setup. Hence, the experimental setup allows the switch between trans- and cis-state by coupling in an UV light source. The authors found out that the change from a cis- to a trans-state changes the contour length of the polymer. This experimental setup also has been mimicked by molecular dynamic simulations [83]. In both cases, they measured the difference of extension Δl per switched azobenzene monomer at a given force. The experiment provided a change of $\Delta l/(\text{monomer } \mathring{A}) = 0.6$, and the simulations provided a change of $\Delta l/(\text{monomer } \mathring{A}) = 1.45$, here the switch was performed vice versa. From this, one can motivate that the influence of photo switches can be described by changing the harmonic bond distance. Experimentally, this could be confirmed on a larger scale by a macroscopic effect. They created a vertically oriented, self-assembled azobenzene monolayer, which was coated on a gold substrate. On top of the monolayer, they put a mercury electrode drop. Hence, they have created an electrical metal-molecule-

metal junction switching the trans- to cis-state (forward $\lambda \approx 370$[nm], backward $\lambda \approx 400$[nm]), which enables them to change the (tunnelling) distance between the electrodes that is also associated with mechanical work, i.e., lifting of the mercury drop [84].

Azobenzene photo switches have been studied for a lot of different applications. In the context of **SCMF** simulations we want to use photo switches to control the directed self assembly of a diblock copolymer on a substrate. In order to observe different phases that change the macroscopic thermal transport properties of the polymeric material we assume that the mechanical change, cf. [82], of the elongation of an azobenzene polymer can be represented by a change of the harmonic potential's bond distance. Therefore we introduced a scaling of the harmonic bond constant, which indirectly controls the bond distance and chain stress tensor, respectively. The **SCMF** method has been introduced in sec. 3.6.

4.9.1 In-situ switching during dip-coating

The natural lamella spacing of symmetric diblocks can be derived from minimisation of single chain stress tensor of a lamellar in a unit cell to $L_0 \approx 1.74\ [R_e] \approx 100$ [nm], for $\chi N = 30$, which enables the connection to the experimental measurement of the lamellar spacing and the length scale of the **SCMF** simulation. The typical thickness of one single lamellar is of the order of 50 [nm]. In conformity with the experiment, the film is thin and has a height $h/R_e = 0.5$. All other parameters are specified in table 4.5. The substrate, in an experiment, preferentially attracts the A or B part of the diblock. Hence, we introduce an additional preference for the A part on top of the substrate. This surface preference is exclusively applied to the first layer on top of the substrate. The height of this layer corresponds to one cell of the density fields or quasi-instantaneous field approximations, respectively. In collaboration with experimentalist, the group of Roy Shenhar, The Hebrew University of Jerusalem, different phases of thin films compromised of symmetric diblocks have have been identified. In a parameter study of the preference of the substrate was tuned to their observations, which are three different phases: a perpendicular lamellar phase from $\sigma_{\text{ext.}} = 0 - 17$, a hexagonal phase from $\sigma_{\text{ext.}} = 18 - 25$ and a horizontal lamella phase starting at $\sigma_{\text{ext.}} = 18 - 25$. In the numerical example, we prepare two systems, which have a surface preference of $\sigma_{\text{ext.}} = 17$, in the switched and the unswitched case. This preference enters in between the hexagonal and lamellar phase.

Fig. 4.35 represents these two numerical examples. The orange-black colour

Parameter	value	unit
Nreference beads	64	–
dt	0.17	t
χN	30	e
κN	30	e
$L_x \times L_y \times L_z$	$30 \times 30 \times 0.66666$	R_e^3
$n_x \times n_y \times n_z$	$360 \times 360 \times 8$	–
$\sigma_{\text{ext.}}$	17	e
diblock structure	$A\{32\}B\{32\}$	–
AA	HARMONICVARIABLESCALE	–
AB	harmonic	–
BB	harmonic	–
harmonicvariablescale	1.0; 1.5	–

Table 4.5 Simulation parameters of a thin film of symmetric AB diblocks coated on a preferential surface, with periodic boundary conditions in x- and y-direction. The z-layer $n_z = 7$ and $n_z = 0$ restricts polymers to be in layer $n_z = 1 - 6$. The z-layer $n_z = 1$ is modified with a repulsive/attractive field, which has the strength $\sigma_{\text{ext.}} = \pm 17$.

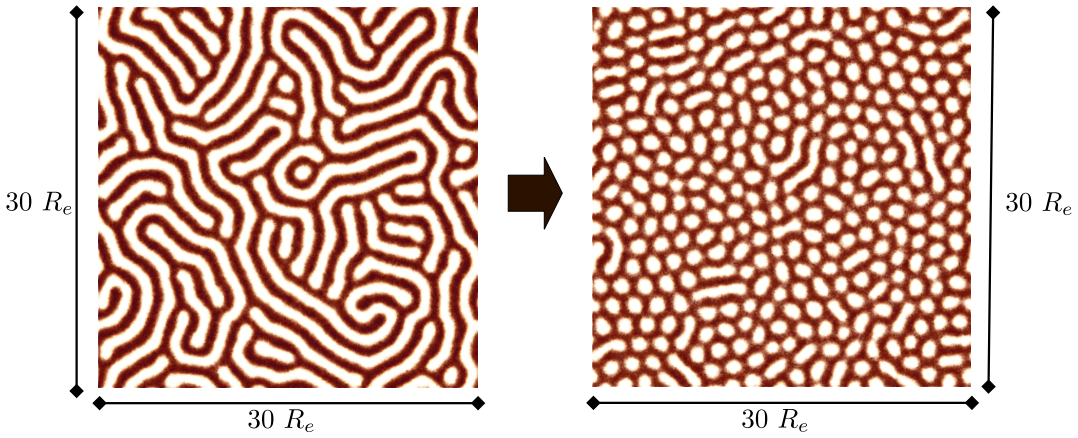

Figure 4.35 This is the top view of a thin film composed of AB diblocks, which have been simulated with **SCMF**. The left image represents the trans-state without excitation. In the right image the harmonic bond distance of diblocks' A part has been switched, i.e., rescaled a factor of 1.5. Hence, the right image represents the exited, switched case, in which a more compact hexagonal cis-state is observed. The black colour indicates the B part, the A part is left blank. Detailed parameters are summarised in table 4.5. Simulations ran for 400.000 Monte-Carlo sweeps or ~ 40 Rouse-relaxation times, respectively.

indicates the B part of the diblock, white space in between covers the switches A part of the diblock. The left unswitched system is in the lamella phase, whereas the

switched system is the hexagonal phase.

Discussion A simulation that is done at the boundary of two phases can be switched into another phase. This can be explained by the change of the stress that is induced by chain segments. Via switching, the elongation of the chain decreases. Hence, it becomes more compact and more blocks, which are attractive, can adsorb at the surface. Simulations have been started in a random, unordered phase that represents the initial, solvent-swollen state of dip-coating. Hence, free energy barriers are low and it is easier to end up in a final state. The energy barrier of an interface increases by increasing the invariant degree of polymerisation $\mathcal{N}$ and the incompatibility parameter χN. Nonetheless, it is possible to recover structures that have been observed by experiments.

4.9.2 In-situ switching in a thin film with periodic boundary conditions

Now, we discuss simulation results of diblock copolymers in a film with periodic boundary conditions. Figure 4.36 shows the phase diagram of a diblock copolymer. This phase diagram has been calculated by Matsen using SCFT calculations [85]. The x-coordinate represents the volume fraction and the y-coordinate corresponds to the incompatibility parameter χN. Black lines mark the phase boundaries in the case that distance of A and B segments are symmetric, $b_\mathrm{A}/b_\mathrm{B} = 1$. Blue lines mark phase boundaries in the case that statistical segment length of A and B segments are not symmetric, ratio $b_\mathrm{A}/b_\mathrm{B} = 1.5$. The motivation to select a ratio on this order is taken by the atomic force probe experiments, which have been discussed before [82, 83]. The important phases are marked by coloured areas: the blue area indicates a cylindrical phase, the red area indicates the region where a switch might be possible, the green area indicates a lamella phase. In between these three phases the two white intervals are left which correspond to a gyroid phase. The red point indicates the position in the phase diagram where simulations are performed, $f = 0.4$, $\chi N = 17$. Below the black dashed line, only a micellar ordering into phases is observed, i.e., the system is in the disordered phase. Hence, at the chosen position in the phase diagram, the free energy barrier, which has to be passed to change the phase, is lower and the probability increases to observe a switch of phase, which is induced by the change of harmonic bond distance. Figure 4.37 represents two top views of **SCMF** simulations that have been simulated for approximately

Parameter	value	unit
Nreference beads	64	–
dt	0.17	t
χN	17	e
κN	30	e
$L_x \times L_y \times L_z$	$30 \times 30 \times 0.9166$	R_e^3
$n_x \times n_y \times n_z$	$180 \times 180 \times 5$	–
diblock structure	$A\{25\}B\{39\}$	–
BB	HARMONICVARIABLESCALE	–
AB	harmonic	–
AA	harmonic	–
harmonicvariablescale	$1.0 \rightarrow 1.5$	–

Table 4.6 Simulation parameters of a thin film of AB diblocks. Periodic boundary conditions are applied to all directions.

40 Rouse-relaxation times. Detailed simulation parameters can be found in table 4.6. The two top views represent two cases: default state with an equal ratio of harmonic bonds and a switched state with a rescaling of the harmonic bond distance by $b = 1.5$. The left image is the default and the right image is the switched case. In the default state, the lamella phase dominates the system's phase, whereas in the switched case, the system changes its phase, which might be characterised by cylindrical phase. The switching was applied to the longer B part of the diblock. Hence, this can be related to the phase diagram: b_B becomes smaller, whereas the ratio $b_\mathrm{A}/b_\mathrm{B}$ becomes larger.

Discussion The **SCMF** simulations agree with the idea motivated by the form of the phase diagram. The phase diagram was calculated via self-consistent field theoretical calculations performed by Matsen [85]. These calculations do not consider thermal fluctuations, hence, these calculations predict a lower transition to a disordered state. Practically, we determined this phase transition in **SCMF** simulations by reducing the incompatibility parameter down to $\chi N \approx 15$. The simulations have been performed close above the disordered-to-ordered phase transition to have a high probability to observe a switched phase, which is not a lamella one. The phase transition between disordered to lamellar is fluctuation-induced first order, transitions between different spatially modulated phases are first order already within mean field. Probability in this context means that approximately

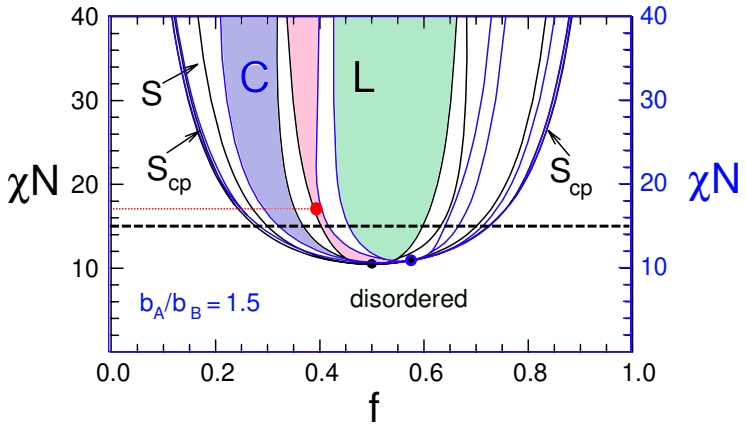

Figure 4.36 Phase diagram of a diblock with equal (black) and modified ratio bond distance (blue). The red point addresses values of the simulation: incompatibility $\chi N = 17$ and volume fraction $f \approx 0.4$. Below the black-dashed line, only a poor ordering of phases is observed. The phase named by S represents spherical micelles arranged on a cubic grid, BCC. The blue area indicates a cylindrical phase. The red area indicates the region where a switch might be possible. The green area indicates the lamellar phase. Between these three phases, the two white intervals correspond to the gyroid phase. Figure (modified) with permission from J. Phys. Cond. Mat., [85], Copyright (2018) IOP Publishing.

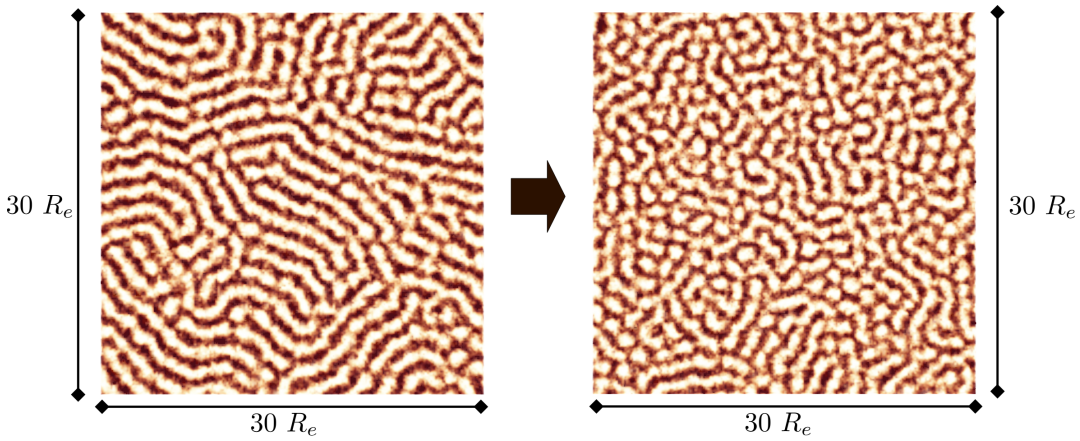

Figure 4.37 Top view of two **SCMF** simulations. Snapshot is taken at 40 Rouse-relaxation times. The left part is the default state, the right part is the switched condition. The colour code, which runs from white to black, represents the type of the block from A to B. Hence, the black part represents the B part that was switched. The incompatibility parameter is $\chi N = 17$, which exhibits fluctuations of interfaces. Hence, the system is close to a disordered phase, because being close to this transition point enables a high influence of the switching. Detailed parameter of the simulation can be found in table 4.6.

only two simulations out of ten show a change of morphology that can by observed in figure 4.37. Hence, getting a better understanding of the instabilities that are induced by the modification of the bonds, requires additional methods, for instance a string method that provides information about the change of system's free energy. We could show that a change of the structural phase induced by photo switches is possible.

Hence, assuming that in the different phases the alignment of interfaces is changed, this can be employed as a control tactic to modify thermal properties of a system. The transport properties of a bulk phase could also be modified by inclusion of nanoparticles to enhance the contrast in change of thermal conductivity. One observes a switched phase if the change induced by the bonds is large enough to drive a stable across a metastable condition into an unstable condition. Meta-stability is not enough, because nucleation can take a long time.

5 Conclusion

Coarse-grained systems allow a universal description of polymers by a minimal set of parameters: a length scale given by the mean end-to-end distance of a polymer, an isothermal compressibility that controls the strength of the non-bonded interactions, and an invariant degree of polymerisation. This universal description relies on explicit **DoF** that are coarse-grained particles' momenta and spatial positions. The new **eMC** scheme couples internal **DoF**s, which have been integrated out, to the explicit **DoF**s that each coarse-grained particle gets an additional internal **DoF**. **eMC** conserves system's total energy and bases on a microcanonical partition function. Based on the microcanonical description, we derived a universal form of the acceptance criterion, which considers the statistical weight of two particles and leaves the proposed new states open to the physics that covers realistic dynamics, i.e., a thermal relaxation between internal **DoF**s. A proposed new state depends on two particles' internal energies and parallel momentum that is accepted/rejected by the Metropolis rate. This Monte-Carlo approach prohibits discretisation errors of first-order integration schemes, which are characteristic for **eDPD** models. By overcoming this limitation **eMC** allows to study energy transport phenomena on long time and length scales, i.e., structural change of morphologies under temperature gradients - Thermophoresis, but also specific effects, which follow from local properties of the underlying molecular structure, e.g., specific heat capacity, polymer chain confirmations and density differences.

The new **eMC** scheme gave insights into transport phenomena in complex polymeric systems. We have shown that the explicit discretisation of a time step does not influence the macroscopic thermal conductivity. The friction in soft systems is mainly controlled by the thermostat, which is called more often for smaller time increments. The **RNEMD** method has been applied to the polymer melt, and caused a linear response, i.e., a linear temperature profile in a steady-state condition. This linear response of the polymer melt permitted that the resulting macroscopic thermal conductivity remains unaltered under the explicit choice of

the current. If the polymers' specific heat capacity is dominated by the internal **DoF**s, it confirmed that the dependency is linear between the internal thermal relaxation, κ_{int}, and the macroscopic thermal conductivity, $\lambda \sim \kappa_{\text{int}}$. The system's transport properties are also influenced by the isothermal compressibility, i.e., the soft interaction parameter of the non-bonded potential. Hence, increasing the isothermal compressibility results in an increased thermal conductivity, too. For this purpose, the polymer melt becomes a more structured fluid, which modifies the number of particles' interactions within the range of the **eMC** update. The **eMC** generated invariant transport properties, because a polymer melt was parametrised on different coarse-grained levels. On these different levels, temperature profiles in a steady-state condition, i.e., the thermal conductivities, became invariant. Therefore, a strategy was presented to rescale the specific heat capacity, c_V, internal thermal relaxation,κ_{int}, and external current by leaving the length scale, R_e, - averaged end-to-end distance - unaltered. These insights were combined to cover structural effects that also have been found in experiments by **eMC**. We emphasised that introducing a parameter set that separates between, e.g., inter- and intramolecular internal thermal relaxation or the length of a polymer, control the macroscopic thermal conductivity. We expanded our studies of thermal transport characteristics to a polymer melt of diblocks. Driven by an incompatibility parameter χN, diblocks formed lamella structures by directed self-assembly. We showed that interfaces influence the thermal conductivity and induce an additional thermal resistance, .i.e., Kapitza resistance. Therefore, we changed the ratio of the parameter set of internal thermal relaxation. A comparison between alternating domains of polymers compromised of (i) diblocks (ii) cut diblocks at the junction point showed a direct influence of molecular connectivity on **eMC**. We continued with the study of star polymers, whose thermal relaxation was controlled by the incompatibility parameter, χN. High incompatibility induced a compression of the free-fluctuating arms of the star polymer to a sphere - minimised interface with less contact to surrounding melt of polymers than before. Finally, we combined a simple cubic lattice of a soft cubic crystal with a polymer melt and expanded **eMC** to a broad range of internal thermal conductivities and specific heat capacities. Based on the simulation results, we conclude that macroscopic thermal conductivity is controlled by the polymer architecture and interfaces formed by directed self-assembly. Hence, these control tactics can be exploited by (a) tailoring the thermal relaxation constant, which is dependent on the architecture, (b) the varying the degree of polymerisation, (c) modifying the incompatibility parameter.

We calculated the **DoS**s by a diagonalised harmonic matrix. The matrices are obtained via a quench of the system. To quench the system the steepest descent method was chosen, which can be understood by introducing an intrinsic viscosity. From the **DoS**, we assumed a vibrational mismatch at the interface and calculated a transmission coefficient, and thermal resistance respectively.

Based on experiments that have been done on photo switches in polymers we motivated a strategy to implement the transition from trans- to cis-state (isomerisation and change of the dipole moment) by a rescaling of the harmonic bond constant. This strategy allowed us to recover trends of experiments conducted with dip-coated polymers, which indicated that phase changes from hexagonal to lamella phases are possible. But it also showed that an in-situ switching from one to another is possible.

6 Appendix

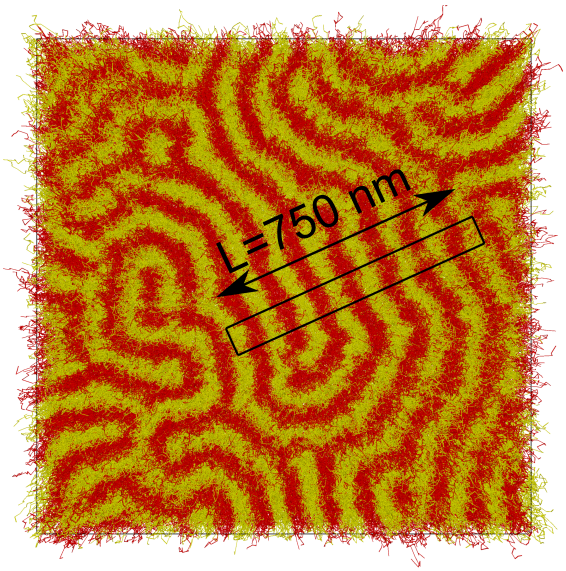

Figure 6.1 Symmetric diblock copolymers phase separated into a lamella pattern via self-assembly ($\sim 5 \cdot 10^5$ particle). **eMC** enables to investigate large structures even if system sizes in this thesis have been smaller, i.e., we studied thermal transport across alternating interfaces that are reduced to a one dimensional temperature profile, fig. 4.10. The typical size of these systems is added by the rectangular box.

6.1 Microphase separated diblocks

eMC allows to study energy transport on large time and length scales. Fig. 6.1 represents a large system that has been simulated by the **eMC** scheme. The red colour indicates the A and the yellow colour indicates the B phase. In this thesis, we focused on system sizes that allow a systematically study, i.e, of thermal transport across interfaces. These systems sizes are chosen smaller to reduce computational effort. A typical system size that has been considered in these studies is marked in fig. 6.1, too. This figure motivates that the capabilities of **eMC** are not exhausted yet.

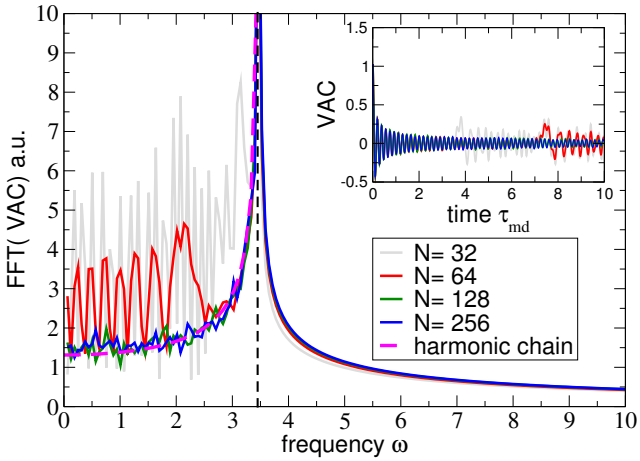

Figure 6.2 FFT power spectrum of **VAC** (inset). If **VAC**s have calculated for Gaussian chains without non-bounded interactions. Distance vectors of chain segments have been grown randomly by a three-dimensional Gaussian distribution. Even the **FFT** is in arbitrary units it can be related with the **DoS** of a harmonic chain. Maximum frequency is $\omega_{\max} = 2\sqrt{E_B/m} \approx 3.47\tau_{\mathrm{md}}^{-1}$.

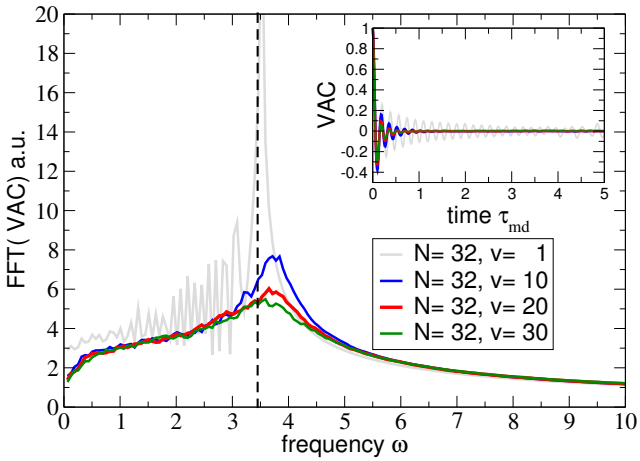

Figure 6.3 FFT power spectrum of **VAC** (inset). **VAC**s have been calculated a chain, which was discretised by N= 32, non-bounded interactions are increased. Vertical dashed line, $\omega_{\max} = 2\sqrt{E_B/m} \approx 3.47\tau_{\mathrm{md}}^{-1}$, vanishes by increasing the soft interaction v_{ij}. The number density of the system is $\rho\sigma^3 = 10$.

6.2 DoS of harmonic chains via VAC

Transport properties are strongly influenced by the chain conformations. This counts for simulations, which include and exclude internal **DoF**s. The structure

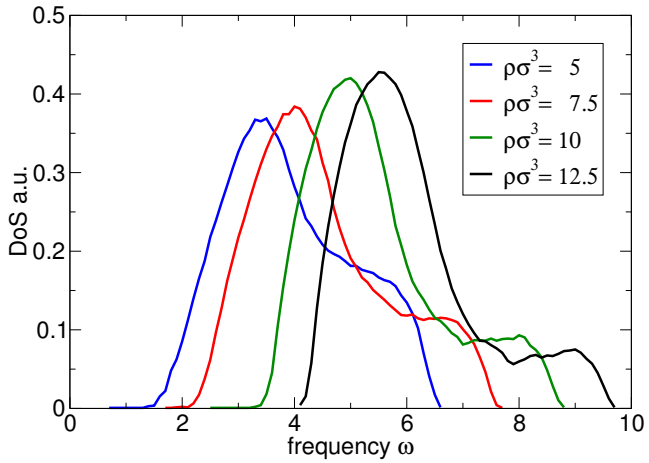

Figure 6.4 DoS for a system with fixed soft interaction parameter $v = 3$. Varying the densities of the system between $\rho\sigma^3 = 5, 7.5, 10, 12.5$. The number of particles is 4800. We observe that increasing the density shifts the peak of the **DoS** to higher frequencies.

of a polymer can be described by a linear harmonic chain. In section 2.2.3, we introduced a harmonic one-dimensional chain. Each segment's motion is affected by the forces of their neighbours only. Hence, there are no acting external forces or non-bonded interactions, respectively. Fig. 6.2 represents free harmonic chains without any external forces. They are the ideal set to test the work flow of identifying a **DoS** by a Fourier transformation of the **VAC**. Then, the maximum and minimum frequency, which can be observed in these systems, can be calculated analytically. Maximum frequency is calculated by the harmonic bonding constant, E_B, to $\omega_{\max} = 2\sqrt{E_B/m} \approx 3.47\tau_{\mathrm{md}}^{-1}$. In an additional step, we introduced soft repulsive non-bonded interaction to the system. The ability of chain segments to vibrata is restricted, and the frequency spectra of the chains are dumped, fig. 6.3.

6.3 DoS of a soft fluid for different densities

We explained the quenching procedure in the main part of the thesis for different interaction parameters, sec. 4.8.2. Fig.6.4 concludes the **DoS** of a system of soft monomers $v = 3$ containing 4800 particles. Box dimensions have been selected cubic. We observe that increasing the density shifts the peak to higher frequencies.

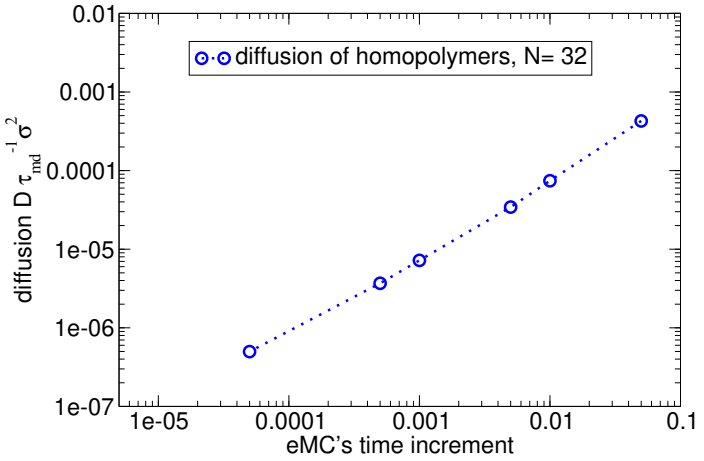

Figure 6.5 The diffusion time of homopolymers, $N = 32$, as a function of the time increment, scales linearly with the time increment of **eMC**, $D(\mathrm{d}t) = (0.05 \pm 0.001) \cdot \mathrm{d}t$. The time increment is equal for **eMC** and the Velocity-Verlet scheme. Hence, eMC is called once per integration.

6.4 eMC: dependence of time increments on external DoFs diffusion

The **eMC** scheme has been explained in terms of a thermostat. The polymer systems are described by soft models so that the friction in the system is mainly influenced by a thermostat. The thermostat destroys correlations between particles' momenta. In a small numerical example, we measure the mean-squared displacement of centre of mass of a polymer and determine the diffusion constant. The number density of the system is $\rho\sigma^3 = 6$, the soft repulsive interaction is $\frac{v_{\mathrm{ij}}}{k_{\mathrm{B}}T} = 0.6667$, internal thermal relaxation is $\frac{\kappa_{\mathrm{int}}\tau_{\mathrm{md}}}{k_{\mathrm{B}}T^2} = 1000$, specific heat capacity of each internal **DoF** is $c_V/k_{\mathrm{B}} = 1000$.

Fig. 6.5 represents the thermal diffusion constants, D, as the function of the time increment eMC has been called. The diffusion values are calculated from the mean-squared displacement of the polymers' centre of mass and long time behaviour $t \to \infty$ of g_3, respectively. Figure 6.5 shows a linear dependence between calling **eMC** and the diffusion constants. This has the advantage that the thermal conductivity increases on the one hand, and on the other hand the centre of mass diffusion decreases, which dictates the time scale and still rescales the macroscopic

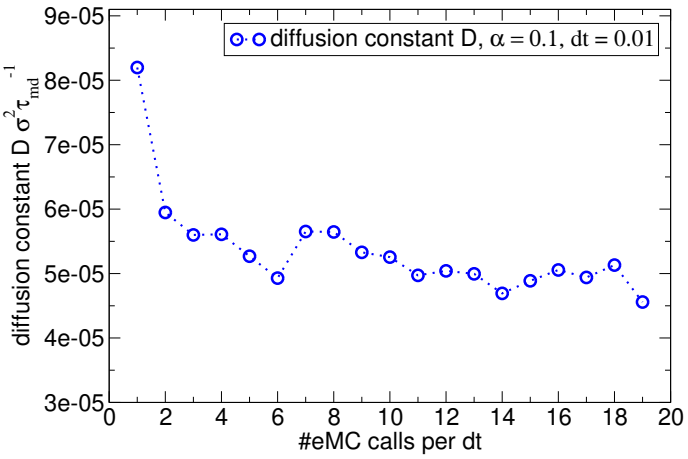

Figure 6.6 The diffusion time is determined via g_3, mean-squared displacement of polymer's centre of mass. The time increment equals the time increment of the Velocity-Verlet scheme. Within one Velocity-Verlet step the **eMC** scheme is called up to 20 times. The partially weighted parallel momenta are destroyed successively by number of **eMC** calls. Friction reaches the maximum when there are no correlations left and might becomes independent from number of calls.

thermal conductivity to larger values.

6.5 eMC: dependence of the number of eMC calls on external DoFs' diffusion

The **eMC** routine couples the internal **DoF**s by partially weighted exchange of the parallel momentum of an interacting particle pair. The parallel momentum is drawn from a Gaussian distribution, which has been normalised by the mean local temperature of the two particles. The partial weighting between old and new parallel momenta is controlled by a constant $\alpha = 0.1$. Hence, a higher number of calls destroys the correlation between two consecutive Velocity-Verlet integration steps, which increases friction in the system and reduces the diffusion time of the polymer's centre of mass. Figure 6.6 represents a numerical example, in which the number of **eMC** calls per Velocity-Verlet integration has been increased. The number density of the system is $\rho\sigma^3 = 6$, the soft repulsive interaction is $v_{\mathrm{ij}} = 0.6667$, internal thermal relaxation is $\frac{\kappa_{\mathrm{int}}\tau_{\mathrm{md}}}{k_{\mathrm{B}}T^2} = 1000$, and specific heat capacity of each internal **DoF** is $c_V/k_{\mathrm{B}} = 1000$, again cf. sec. 6.4.

One observes that the diffusion D, which is determined by the polymer's mean-squared displacement of the centre of mass, is reduced by increasing the number of **eMC** calls. However, at high number of **eMC** calls, i.e., when the number of calls is larger than 10, it seems to be that the diffusion constant D converges to a constant value. We also used the same framework to identify the dependence of number of calls of **eMC** on macroscopic thermal conductivities, cf. [11]. Here, we measured the decay length of a Gaussian profile, and thermal conductivity λ, respectively.

6.6 Explicit derivations to calculate entries of the harmonic matrix

Potential

$$\begin{aligned} V_{\text{soft}} &= \frac{k}{2} \cdot (1 - \Delta r)^2 \\ &= \frac{k}{2} \cdot \left(1 - \sqrt{(\Delta x)^2 + (\Delta y)^2 + (\Delta z)^2}\right)^2 \\ &= \frac{k}{2} \cdot \left(1 - \sqrt{(x_1 - x_2)^2 + (y_1 - y_2)^2 + (z_1 - z_2)^2}\right)^2 \end{aligned}$$

1st Derivatives

$$\begin{aligned} \frac{\partial V_{\text{soft}}}{\partial \Delta r} &= k \cdot (1 - \Delta r) \\ \frac{\partial V_{\text{soft}}}{\partial \Delta x} &= k \cdot \left(1 - \sqrt{(\Delta x)^2 + (\Delta y)^2 + (\Delta z)^2}\right) \cdot \frac{2(\Delta x)}{2\sqrt{(\Delta x)^2 + (\Delta y)^2 + (\Delta z)^2}} \\ &= k \cdot \Delta x \cdot \left(1 + \frac{1}{\sqrt{(\Delta x)^2 + (\Delta y)^2 + (\Delta z)^2}}\right) \\ \frac{\partial V_{\text{soft}}}{\partial x_1} &= k \cdot (x_1 - x_2) \cdot \left(1 + \frac{1}{\sqrt{(x_1 - x_2)^2 + (\Delta y)^2 + (\Delta z)^2}}\right) \end{aligned}$$

2nd Derivatives

$$\frac{\partial V_{\text{soft}}}{\partial \Delta x \partial \Delta x} = k\left(1 + \frac{1}{\sqrt{(\Delta x)^2 + (\Delta y)^2 + (\Delta z)^2}} - \frac{\Delta x^2}{((\Delta x)^2 + (\Delta y)^2 + (\Delta z)^2)^{3/2}}\right)$$
$$\frac{\partial V_{\text{soft}}}{\partial \Delta x \partial \Delta y} = k \cdot \frac{-\Delta x \Delta y}{((\Delta x)^2 + (\Delta y)^2 + (\Delta z)^2)^{3/2}}$$
$$\frac{\partial V_{\text{soft}}}{\partial \Delta x \partial \Delta y} = k \cdot \frac{-\Delta x \Delta y}{((\Delta x)^2 + (\Delta y)^2 + (\Delta z)^2)^{3/2}}$$

$$\frac{\partial^2 V}{\partial r_{x_1} \partial r_{x_2}} = k\left(1 + \frac{1}{\sqrt{(x_1 - x_2)^2 + (\Delta y)^2 + (\Delta z)^2}} - \frac{(x_1 - x_2)^2}{((x_1 - x_2)^2 + (\Delta y)^2 + (\Delta z)^2)^{3/2}}\right)$$
$$\frac{\partial^2 V}{\partial r_{x_1} \partial r_{y_2}} = k \cdot \frac{-(x_1 - x_2)(y_1 - y_2)}{((x_1 - x_2)^2 + ((y_1 - y_2))^2 + (\Delta z)^2)^{3/2}}$$
$$\frac{\partial^2 V}{\partial r_{x_1} \partial r_{z_2}} = k \cdot \frac{-(x_1 - x_2)(z_1 - z_2)}{((x_1 - x_2)^2 + ((\Delta y))^2 + (z_1 - z_2)^2)^{3/2}}$$
$$\frac{\partial^2 V}{\partial r_{y_1} \partial r_{x_2}} = k \cdot \frac{-(x_1 - x_2)(y_1 - y_2)}{((x_1 - x_2)^2 + ((y_1 - y_2))^2 + (\Delta z)^2)^{3/2}}$$
$$\frac{\partial^2 V}{\partial r_{y_1} \partial r_{y_2}} = k\left(1 + \frac{1}{\sqrt{(\Delta x)^2 + (y_1 - y_2)^2 + (\Delta z)^2}} - \frac{(y_1 - y_2)^2}{((\Delta x)^2 + (y_1 - y_2)^2 + (\Delta z)^2)^{3/2}}\right)$$
$$\frac{\partial^2 V}{\partial r_{y_1} \partial r_{z_2}} = k \cdot \frac{-(y_1 - y_2)(z_1 - z_2)}{((\Delta x)^2 + ((y_1 - y_2))^2 + (z_1 - z_2)^2)^{3/2}}$$
$$\frac{\partial^2 V}{\partial r_{z_1} \partial r_{x_2}} = k \cdot \frac{-(x_1 - x_2)(z_1 - z_2)}{((x_1 - x_2)^2 + ((y_1 - y_2))^2 + (z_1 - z_2)^2)^{3/2}}$$
$$\frac{\partial^2 V}{\partial r_{z_1} \partial r_{y_2}} = k \cdot \frac{-(y_1 - y_2)(z_1 - z_2)}{((\Delta x)^2 + ((y_1 - y_2))^2 + (z_1 - z_2)^2)^{3/2}}$$
$$\frac{\partial^2 V}{\partial r_{z_1} \partial r_{z_2}} = k\left(1 + \frac{1}{\sqrt{(\Delta x)^2 + (\Delta y)^2 + (z_1 - z_2)^2}} - \frac{(z_1 - z_2)^2}{((\Delta x)^2 + (\Delta y)^2 + (z_1 - z_2)^2)^{3/2}}\right)$$

6.7 Calculating large EV problems

Many physical problems can be expressed by an eigenvalue problem. Hence, it is necessary to find easy tools to solve such problems. In the following, we want to present tools that have been used to calculate large eigenvalue problems. The presented algorithms deal with dense symmetric matrices but can also handle sparse matrices. These algorithms are adopted from the documentation of **CUDA** and

Intel®MKL.

EV problems via CUDA **GPU** architectures can be used very efficient to calculate large eigenvalue problems. Pascal architecture gives rise to a new feature - **cudaMallocManaged**. Practically, this allows the **GPU** to handle more memory, which is physical available by using memory pages. The hard limit of the problem size is set by the size of the **lwork**, which is $\approx$ **32 000**. Due to the Licence of Nvidia, we only refer to the documentation of the Nvidia Toolkit [1] and suggest to start with the package CuSolver and the routine: cuSolverDN: Dense **LAPACK**.

EV problems via Intel®MKL Also, CPU architectures give rise to large eigenvalue problems. Intel64 has the advantage that **lwork** can be larger such that the problem size is not limited any more. The EV solver compiled for Knights landing architecture is only faster than a Nvidia P100 if the problem size pretends to use cudaMallocManaged. [2]

6.8 Change of the bonded potential to avoid the collapse of the Gaussian bond

In fact, quenching a system of polymers via steepest descent causes a collapse of chains. This collapse of Gaussian chains is predictable, because their distance of segments is proportional to the temperature. In principle, there are two different ways to preserve the structure of the bonds (i) re-scale the harmonic bond energy with the inverse temperature (ii) swap from Gaussian bonds to harmonic springs with an arbitrary origin, which is equal to $b\sigma^{-1} = 1$. Strategy (i) breaks down in feasibility, because it becomes quite challenging to define a temperature in quenched state. In consequence, we follow strategy (ii). The potential changes from $V_1(r) = \frac{k_1}{2} \cdot r^2$ to $V_2(r) = \frac{k_2}{2} \cdot (r-1)^2$. We claim the bonded energy to be constant under this transformation such that $\int_0^\infty P_1(r)V_1(r) = \int_0^\infty P_2(r)V_2(r)$. $P_1(r)$ and $P_2(r)$ are assumed to have a fixed second moment σ^2. We do this assumption, because other analytic approaches failed. The harmonic constant k_1 is given and k_2 is chosen so that the derivation $\sigma_1^2 = \sigma_2^2 = \sigma^2$ of both remains unaltered. We

[1] (http://docs.nvidia.com/cuda/index.html, April 12, 2018).
[2] (https://software.intel.com/en-us/articles/introduction-to-the-intel-mkl-extended-eigensolver, April 12, 2018).

solve the integral $\int_0^\infty P_1(r)V_1(r)r^2 = \int_0^\infty P_2(r)r^2V_2(r)$ and reshape the solution as a function of k_1 and k_2.

$$k_2 = \frac{\frac{2}{\sqrt{2\pi}}\exp\left(\frac{-1}{2\sigma^2}\right) + \frac{(1+\sigma_1^2)}{\sigma_1}\left(1+\mathrm{erf}\left(\frac{-1}{\sqrt{2}\sigma_1}\right)\right)}{\frac{2}{\sqrt{2\pi}}\exp\left(\frac{-1}{2\sigma_2^2}\right) + \sigma_2\left(1+\mathrm{erf}\left(\frac{1}{\sqrt{2}\sigma}\right)\right)}. \tag{6.1}$$

We define the constants $A = \exp\left(\frac{-1}{2\sigma^2}\right)$ and $B = \mathrm{erf}\left(\frac{-1}{\sqrt{2}\sigma_1}\right)$ and claim for a typical order of $\sigma = 0.1$ that $A \approx 0$ and $B = 1$. Hence, under these specific conditions, we get a relation between harmonic constants k_1, k_2 and σ.

$$k_2 \approx \frac{(1+\sigma^2)}{\sigma^2} \cdot k_1 \approx 101 \cdot k_1. \tag{6.2}$$

This strategy is however not quite accurate, because reducing the distribution of bonds to its mean distance $\mu = 1$ (for $k_\mathrm{B}T = 1$) and derivation σ is quite tough. Therefore, we already started the simulation with a modified potential with arbitrary origin at $b\sigma^{-1} = 1$. We chose the harmonic spring in the order of relation 6.2. As a side remark, towards the choice of the cut-off distance of the soft non-bonded potential, which is $r_\mathrm{cut}\sigma^{-1} = 1$, forces of bonded interactions are always calculated independently from cut-off.

6.9 C implementation of the eMC algorithm

For the interested reader, the core function of eMC scheme, cf. fig.3.2, is presented. This implementation is a strict realisation of the theoretical scheme introduced in sec. 3.3 and visualised in fig. 3.3.

```
1
3
5  ...
   kappa       = calc_kappa(conf,particle1,particle2);
7  e1_old      = particle1->e;
   s1_old      = s(particle1);
9  ds1_old     = ds(particle1);
   dds1_old    = dds(particle1);

11 e2_old      = particle2->e;
   s2_old      = s(particle2);
13 ds2_old     = ds(particle2);
   dds2_old    = dds(particle2);

15 m1          = particle1->m;
   m2          = particle2->m;
17 invmcm      = 1.0/(m1+m2);
   mred        = invmcm* m1*m2;
19    (r2>R2MIN) {\
    norm = 1.0/r2;
```

```
21 }
       {
23     norm = 1.0/R2MIN;
}
25 norm = sqrt(norm);
     (idim=0,ppara_old=0;idim<conf->Ndim;idim++) {
27   dist_omp[idim] *= norm;
     dp_omp[idim]     = m2*invmcm*particle1->p[idim] - m1*invmcm*particle2->p[idim];
29   ppara_old  += dp_omp[idim]*dist_omp[idim];
}
31 kqt_old     = kappa*conf->h*(ds1_old-ds2_old);
sigmaq       = 2*kappa*conf->h;
33 dq_old      = sqrt(sigmaq)*gauss_r250(0.0,1.0);

T_loc        = 2.0/(ds1_old+ds2_old);

35 sigmap_old = mred*T_loc*a2;
dp_old       = sqrt(sigmap_old)*gauss_r250(0.0,1.0);

37 ppara_new  = a1*ppara_old + dp_old;


39 e1_new      = e1_old + kqt_old + dq_old -de_kin*dds2_old/(dds1_old+dds2_old);

e2_new      = e2_old - kqt_old - dq_old -de_kin*dds1_old/(dds1_old+dds2_old);

41     ((e1_new>0)&&(e2_new>0)) {
   particle1->e = e1_new;
43   s1_new      = s(particle1);
   ds1_new     = ds(particle1);
45   dds1_new    = dds(particle1);
   particle1->e = e1_old;
47   particle2->e = e2_new;
   s2_new      = s(particle2);
49   ds2_new     = ds(particle2);
   dds2_new    = dds(particle2);
51   particle2->e = e2_old;
   sigmap_new = 2.0*mred/(ds1_new+ds2_new)*a2;

53




55



57     pre =    sqrt(sigmap_old/sigmap_new);
     arg      = s1_new+s2_new-s1_old-s2_old;
59     arg     += -0.5*dp_new*dp_new/sigmap_new + 0.5*dp_old*dp_old/sigmap_old;

                 prob     = pre*exp(arg);
61       }     {
                 pre =    sqrt(sigmap_old/sigmap_new);
63               arg      = s1_new+s2_new-s1_old-s2_old;

                 arg     += -0.5*(dq_new*dq_new-dq_old*dq_old)/sigmaq;

65               arg     += -0.5*dp_new*dp_new/sigmap_new + 0.5*dp_old*dp_old/sigmap_old;

                 prob     = pre*exp(arg);
67       }
         ((prob>1)||(double_r250()<prob)) {
69     nacc_omp ++;
     particle1->e = e1_new;
71     particle2->e = e2_new;
     fac = ppara_new-ppara_old;
73       (idim=0;idim<conf->Ndim;idim++) {
       particle1->p[idim] += fac*dist_omp[idim];
75     particle2->p[idim] -= fac*dist_omp[idim];
     }
77   }
}
```

6.10 Nomenclature and list of abbreviations

Latin character

Variable	meaning	unit
c	speed of sound	$\sigma/\tau_{\mathrm{md}}$
$D(\omega)$	density of states	**1**
E	energy	ϵ
f	Boltzmann eq. probability distribution function	**1**
F	free energy	$k_{\mathrm{B}}T$
F^{C}	conservative force	$m\sigma\tau_{\mathrm{md}}^{-2}$
F^{D}	dissipative force	$m\sigma\tau_{\mathrm{md}}^{-2}$
F^{R}	random force	$m\sigma\tau_{\mathrm{md}}^{-2}$
$\mathcal{H}_b$	Hamiltonian bonded potentials	$k_{\mathrm{B}}T$
$\mathcal{H}_{nb}$	Hamiltonian non-bonded+ potentials	$k_{\mathrm{B}}T$
J_Q	energy flux	ϵ/σ^2
k_{B}	Boltzmann constant	$1.380 \cdot 10^{-23}$ [J]/[K]
K	wavevector	σ^{-1}
m	mass	**1**
N	number of segments	**1**
$\bar{\mathcal{N}}$	invariant degree of polymerisation	**1**
$\vec{p}$	momentum	$m\sigma/\tau_{\mathrm{md}}$
P	probability distribution	**1**
δq	thermal noise in eMC	ϵ
$R_{\mathrm{interface}}$	thermal resistance at interface	**1**
$s(e)$	internal entropy	k_{B}
S	entropy	k_{B}
T	temperature	T
$\delta\mathcal{T}$	kinetic energy that is distributed	ϵ
rnecurrent	energy transported per area Ain time $\tau_{\mathrm{md}}\sigma^2$	$\frac{k_{\mathrm{B}}T}{\tau_{\mathrm{md}}A}$

E	energy	$k_\mathrm{B}T$
$\vec{U}$	averaged velocity in **BE**	σ/τ_md
v_ij	soft interaction parameter	$k_\mathrm{B}T\sigma^2$
v	velocity	σ/τ_md
$\mathcal{Z}_\mathrm{mic}$	microcanonical partition function	**1**

Table 6.1 List of Latin characters

Greek character

Variable	**meaning**	**unit**
α	re-equilibration constant of Peter's thermostat	**1**
α_i	transmission probability transmission of phonons	**1**
β	$1/k_\mathrm{B}T$	$1/\epsilon$
Γ	friction of Lowe-Andersen thermostat	$m\sigma^{-1}\tau_\mathrm{md}^{-1}$
ϵ	energy scale	ϵ
κ	isothermal compressibility	$\tau_\mathrm{md}^2\sigma/m$
κ_int	thermal conductivity for **eMC** move	ϵk_B
κ_T	inverse isothermal compressibility at fixed temperature	$(\tau_\mathrm{md}^2\sigma/m)^{-1}$
μ	reduced mass	m
ξ_r	Gaussian distributed friction	$m\sigma^{-1}\tau_\mathrm{md}^{-1}$
λ	macroscopic thermal conductivity	ϵk_B
θ_T	Einstein temperature	T
σ	length scale of the box	σ
ρ	density	m/σ^3
Φ	particle based density	m/σ^3
χ	Flory interaction parameter	ϵ
ω_D	weighting function in DPD	**1**
ω_D	Debye cut-off frequency	$1/\tau_\mathrm{md}$

ω_R	weighting function in **DPD** *(soft force)*	**1**
ω	frequencies	$1/\tau_{\mathrm{md}}$
ω_{E}	Einstein frequency	$1/\tau_{\mathrm{md}}$
Ω	microcanonical ensemble	**1**

Table 6.2 List of Greek characters

List of abbreviations

Abbreviation	meaning
AFM	Atomic force microscopy
AMM	acoustic mismatch model
BE	Boltzmann equation
CG	coarse-grained
CUDA®	Compute Unified Device Architectur, by Nvidia Corporation
DE	differential equation
DMM	diffusive mismatch model
DSA	directed self-assembly
DPD	dissipative particle dynamics
DoS	density of states
DoF	degrees of freedom
eDPD	energy conserving dissipative particle dynamics
eMC	energy Monte-Carlo
Intel®MKL	Intel ® Math Kernel Library
MD	molecular dynamics
LAPACK	Linear Algebra Package
LED	light-emitting diode
PMMA	Polymethylmethacrylate
PS	Polyethylene

RNEMD	reverse non-equilibrium molecular dynamic
SCMF	single chain in mean field
SCFT	self-consistent field theory
SCD	stochastic differential equation
SOMA	soft coarse-grained Monte-Carlo acceleration
SThM	scanning thermal microscopy
TDE	thermal diffusion equation
TRM	thermal reflection method
VAC	velocity autocorrelation function

Table 6.3 List of abbreviations

Bibliography

[1] G. Pearson, "Conductive device," Oct. 14 1941. US Patent 2,258,958.

[2] M. B. X. C. Dan Zhao, Simone Fabiano, "Ionic thermoelectric gating organic transistors," *Nature Communications*, vol. 8„ p. 14214, January 2017.

[3] P. L. Kapitza, "Heat transfer and superfluidity of helium ii," *Phys. Rev.*, vol. 60, pp. 354–355, Aug 1941.

[4] M. J. P.-P. X. H. W. S. J. A. M. Michael D. Bartlett, Navid Kazem and C. Majidi, "High thermal conductivity in soft elastomers with elongated liquid metal inclusions," *PNAS*, vol. 114, no. 9, 2017.

[5] D. G. Cahill and R. O. Pohl, "Thermal conductivity of amorphous solids above the plateau," *Phys. Rev. B*, vol. 35, pp. 4067–4073, Mar 1987.

[6] F. Döring, H. Ulrichs, S. Pagel, M. Müller, M. Mansurova, M. Müller, C. Eberl, T. Erichsen, D. Huebner, P. Vana, K. Mann, M. Münzenberg, and H.-U. Krebs, "Confinement of phonon propagation in laser deposited tungsten/polycarbonate multilayers," *New Journal of Physics*, vol. 18, no. 9, p. 092002, 2016.

[7] S. G. T. B.-T. S. D. Miguel Munoz Rojo, Jaime Martin and M. Martin-Gonzalez, "Decrease in thermal conductivity in polymeric p3ht nanowires by size-reduction induced by crystal orientation: new approaches towards thermal transport engineering of organic materials," *Nanoscale*, vol. 6, no. 7858, 2014.

[8] K. T. N. D. W. van Krevelen, *Properties of Polymers*. Radarweg 29, PO Box 211, 1000 AE Amsterdam, The Netherlands: Elsevier, fourth ed., 2009.

[9] J. B. Avalos and A. D. Mackie, "Dissipative particle dynamics with energy conservation," *Europhys. Lett.*, vol. 40, p. 141, Oct 1997.

[10] P. Espanol, "Dissipative particle dynamics with energy conservation," *Europhys. Lett.*, vol. 40, p. 631, 1997.

[11] M. Langenberg and M. Müller, "emc: A monte carlo scheme with energy conservation," *EPL*, vol. 114, p. 20001, April 2016.

[12] L. Onsager, "Reciprocal relations in irreversible processes. i.," *Phys. Rev.*, vol. 37, pp. 405–426, Feb 1931.

[13] R. Balian, *From Microphysics to Macrophysics*. Springer Berlin Heidelberg, 1992.

[14] N. Pottier, *Nonequilibrium Statistical Physics: Linear Irreversible Processes*. Oxford University Press, New York, 2010.

[15] M. L. Jacek Banasiak, *Methods of Small Parameter in Mathematical Biology*. Springer International Publishing, 2014.

[16] L. E. M. Landau, L. D., *Course of Theoretical Physics*, vol. 8. Pergamon Press, 1987.

[17] P. L. Bhatnagar, E. P. Gross, and M. Krook, "A model for collision processes in gases. i. small amplitude processes in charged and neutral one-component systems," *Phys. Rev.*, vol. 94, pp. 511–525, May 1954.

[18] M. N. O. David W. Hahn, *Heat Conduction*. John Wiley & Sons, Inc., Hoboken, New Jersey, 2012.

[19] C. Kittel, *Introduction to Solid State Physics*. John Wiley & Sons, Inc., 8 ed., 2005.

[20] A. Einstein, "Die plancksche theorie der strahlung und die theorie der spezifischen wärme [adp 22, 180 (1907)]," *Annalen der Physik*, vol. 14, no. S1, pp. 280–291, 2005.

[21] N. D. M. Neil W. Ashcroft, *Solid State Physics*. Harcourt College Publishers, 1976.

[22] M. J. M. A. Rahman and J. P. McTague, "Molecular dynamics study of an amorphous lennard-jones system at low temperature," *Journal of Chemical Physics*, vol. 64, no. 1564, 1976.

[23] G. Grest, S. Nagel, and A. Rahman, "Quench echoes in molecular dynamics–a new phonon spectroscopy," *Solid State Communications*, vol. 36, no. 10, pp. 875 – 879, 1980.

[24] G. S. Grest, S. R. Nagel, A. Rahman, and T. A. Witten, "Density of states and the velocity autocorrelation function derived from quench studies," *The Journal of Chemical Physics*, vol. 74, no. 6, pp. 3532–3534, 1981.

[25] G. S. Grest, S. R. Nagel, and A. Rahman, "Longitudinal and transverse excitations in a glass," *Phys. Rev. Lett.*, vol. 49, pp. 1271–1274, Oct 1982.

[26] S. V. Meshkov, "Low-frequency dynamics of lennard-jones glasses," *Phys. Rev. B*, vol. 55, pp. 12113–12120, May 1997.

[27] T. Keyes, "Instantaneous normal mode approach to liquid state dynamics," *The Journal of Physical Chemistry A*, vol. 101, no. 16, pp. 2921–2930, 1997.

[28] T. K. M. D. F. P. Moore, A. Tokmakoff, "The low frequency density of states and vibrational population dynamics of polyatomic molecules in liquids," *J. Chem. Phys.*, vol. 103, pp. 3325–3334, September 1995.

[29] G. Seeley, T. Keyes, and B. Madan, "From the density of states to the velocity correlation function in liquids," *The Journal of Physical Chemistry*, vol. 96, no. 10, pp. 4074–4076, 1992.

[30] S. M. Hideyuki Mizuno and J.-L. Barrat, "Beating the amorphous limit in thermal conductivity by superlattices design," *Scientific Reports*, vol. 5, no. 14116, 2015.

[31] F. Leonforte, R. Boissière, A. Tanguy, J. P. Wittmer, and J.-L. Barrat, "Continuum limit of amorphous elastic bodies. iii. three-dimensional systems," *Phys. Rev. B*, vol. 72, p. 224206, Dec 2005.

[32] X. Wang, W. Duan, M. Lin, and G. Wan, "Waves in three-dimensional simple cubic lattice," *Chaos, Solitons & Fractals*, vol. 30, no. 4, pp. 909 – 919, 2006.

[33] Y. M. Beltukov and D. A. Parshin, "Theory of sparse random matrices and vibrational spectra of amorphous solids," *Physics of the Solid State*, vol. 53, pp. 151–162, Jan 2011.

[34] I. Khalatnikov, "Heat exchange between solid and helium ii," *J. Exp. Theor. Phys.*, vol. 22, pp. 687–704, 1952.

[35] E. T. Swartz and R. O. Pohl, "Thermal boundary resistance," *Rev. Mod. Phys.*, vol. 61, pp. 605–668, Jul 1989.

[36] L. D. Bellis and P. E. Phelan, "Variations of acoustic and diffuse mismatch models in predicting thermal-boundary resistance," *Journal of Thermophysics and Heat Transfer*, vol. 14, pp. 144–150, April 2000.

[37] W. A. Little, "The transport of heat between dissimilar solids at low temperatures," *Canadian Journal of Physics*, vol. 37, no. 3, pp. 334–349, 1959.

[38] J. D. N. Cheeke, H. Ettinger, and B. Hebral, "Analysis of heat transfer between solids at low temperatures," *Canadian Journal of Physics*, vol. 54, no. 17, pp. 1749–1771, 1976.

[39] P. Reddy, K. Castelino, and A. Majumdar, "Diffuse mismatch model of thermal boundary conductance using exact phonon dispersion," *Applied Physics Letters*, vol. 87, no. 21, p. 211908, 2005.

[40] T. S. English, J. C. Duda, J. L. Smoyer, D. A. Jordan, P. M. Norris, and L. V. Zhigilei, "Enhancing and tuning phonon transport at vibrationally mismatched solid-solid interfaces," *Phys. Rev. B*, vol. 85, p. 035438, Jan 2012.

[41] E. Abu-Nada, "Energy conservative dissipative particle dynamics simulation of natural convection in liquids," *Journal of Heat Transfer*, vol. 133, p. 112502, 2011.

[42] M. C. A. and Y. J. M., "Dissipative particle dynamics: The equilibrium for finite time steps," *Europhys. Lett.*, vol. 37, p. 511, 1997.

[43] M. H. E. M. Ripoll, P. Espanol, "Dissipative particle dynamics with energy conservation: Heat conduction," *Int. J. Mod. Phys. C*, vol. 9, p. 1329, 1998.

[44] J. B. Avalos and A. D. Mackie, "Dynamic and transport properties of dissipative particle dynamics with energy conservation," *The Journal of Chemical Physics*, vol. 111, no. 11, pp. 5267–5276, 1999.

[45] J. B. A. Allan D. Mackie and V. Navas, "Dissipative particle dynamics with energy conservation: Modelling of heat flow," *Phys. Chem. Chem. Phys.*, vol. 1, pp. 2039–2049, 1999.

[46] G. Stoltz, "A reduced model for shock and detonation waves. i. the inert case," *EPL (Europhysics Letters)*, vol. 76, no. 5, p. 849, 2006.

[47] G. C. Ganzenmuller, S. Hiermaier, and M. O. Steinhauser, "Shock-wave induced damage in lipid bilayers: a dissipative particle dynamics simulation study," *Soft Matter*, vol. 7, pp. 4307–4317, 2011.

[48] J. B. Maillet, E. Bourasseau, N. Desbiens, G. Vallverdu, and G. Stoltz, "Mesoscopic simulations of shock-to-detonation transition in reactive liquid high explosive," *EPL (Europhysics Letters)*, vol. 96, no. 6, p. 68007, 2011.

[49] E. Antillon, K. Banlusan, and A. Strachan, "Coarse grain model for coupled thermo-mechano-chemical processes and its application to pressure-induced endothermic chemical reactions," *Modelling and Simulation in Materials Science and Engineering*, vol. 22, no. 2, p. 025027, 2014.

[50] E. O. Johansson, T. Yamada, B. Sundén, and J. Yuan, "Modeling mesoscopic solidification using dissipative particle dynamics," *International Journal of Thermal Sciences*, vol. 101, pp. 207 – 216, 2016.

[51] G. Bhanot, "The metropolis algorithm," *Reports on Progress in Physics*, vol. 51, no. 3, p. 429, 1988.

[52] P. J. Hoogerbrugge and J. M. V. A. Koelman, "Simulating microscopic hydrodynamic phenomena with dissipative particle dynamics," *Europhys. Lett.*, vol. 19, p. 155, 1992.

[53] P. Español and P. Warren, "Statistical mechanics of dissipative particle dynamics," *EPL (Europhysics Letters)*, vol. 30, no. 4, p. 191, 1995.

[54] E. A. Koopman and C. P. Lowe, "Advantages of a lowe-andersen thermostat in molecular dynamics simulations," *J. Chem. Phys.*, vol. 124, p. 204103, 2006.

[55] C. P. Lowe, "An alternative approach to dissipative particle dynamics," *Europhys. Lett.*, vol. 47, p. 145, 1999.

[56] E. A. J. F. Peters, "Elimination of time step effects in dpd," *Europhys. Lett.*, vol. 66, p. 311, 2004.

[57] L. Pastewka, D. Kauzlarić, A. Greiner, and J. G. Korvink, "Thermostat with a local heat-bath coupling for exact energy conservation in dissipative particle dynamics," *Phys. Rev. E*, vol. 73, p. 037701, Mar 2006.

[58] P.-G. Gennes, *Scaling Concepts in Polymer Physics*. Cornell University Press, 1979.

[59] S. F. E. M. Doi, *The theory of polymer dynamics*. Oxford [u.a.] : Clarendon Press, 1995, international series of monographs on physics ; 73 ed., 1995. SUB Göttingen: 96 A 19671.

[60] P. Espanol, M. Serrano, I. Pagonabarraga, and I. Zuniga, "Energy-conserving coarse-graining of complex molecules," *Soft Matter*, vol. 12, pp. 4821–4837, 2016.

[61] P. O. Scherer, *Computational Physics Simulation of Classical and Quantum Systems*. Springer-Verlag Berlin Heidelberg, 2010.

[62] M. E. Tuckerman, *Statistical Mechanics: Theory and Molecular Simulation*. Oxford University Press, New York, 2010.

[63] H. Yoshida, "Construction of higher order symplectic integrators," *Phys. Lett. A.*, vol. 150, pp. 262–268, 1990.

[64] M. Müller and G. D. Smith, "Phase separation in binary mixtures containing polymers: A quantitative comparison of single-chain-in-mean-field simulations and computer simulations of the corresponding multichain systems," *Journal of Polymer Science Part B: Polymer Physics*, vol. 43, no. 8, pp. 934–958, 2005.

[65] F. Müller-Plathe, "A simple nonequilibrium molecular dynamics method for calculating the thermal conductivity," *J. Chem. Phys.*, vol. 106, p. 6082, 1997.

[66] K. C. Daoulas and M. Müller, "Single chain in mean field simulations: Quasi-instantaneous field approximation and quantitative comparison with monte carlo simulations," *The Journal of Chemical Physics*, vol. 125, no. 18, pp. –, 2006.

[67] L. Schneider and M. Müller, "Multi-architecture monte-carlo (mc) simulation of soft coarse-grained polymeric materials: Soft coarse grained monte-carlo acceleration (soma)," *submitted*, 2017.

[68] T. Ohara, T. Chia Yuan, D. Torii, G. Kikugawa, and N. Kosugi, "Heat conduction in chain polymer liquids: Molecular dynamics study on the contributions of inter- and intramolecular energy transfer," *The Journal of Chemical Physics*, vol. 135, no. 3, p. 034507, 2011.

[69] T. B. S. Y. Hiroki Matsubara, Gota Kikugawa and T. Ohara, "Effects of molecular structure on microscopic heat transport in chain polymer liquids," *J. Chem. Phys.10.1063/1.4919313*, vol. 142, p. 164509, 2015.

[70] A. Henry and G. Chen, "High thermal conductivity of single polyethylene chains using molecular dynamics simulations," *Phys. Rev. Lett.*, vol. 101, p. 235502, Dec 2008.

[71] J. T. R. Z. . G. C. Sheng Shen, Asegun Henry, "Polyethylene nanofibres with very high thermal conductivities," *Nature Nanotechnology*, vol. 5, pp. 251 – 255, March 2010.

[72] P. L. Kapitza, "Heat transfer and superfluidity of helium ii," *J. Phys. (Moscow)*, vol. 4, p. 181, 1941.

[73] Z. Wang, J. A. Carter, A. Lagutchev, Y. K. Koh, N.-H. Seong, D. G. Cahill, and D. D. Dlott, "Ultrafast flash thermal conductance of molecular chains," *Science*, vol. 317, no. 5839, pp. 787–790, 2007.

[74] F. C. Jean-Louis Barrat, "Kapitza resistance at the liquid solid interface," *Molecular Physics*, vol. 101, p. 1605, 2003.

[75] P. V. Dennis Huebner, Christian Rossner, "Light-induced self-assembly of gold nanoparticles with a photoresponsive polymer shell," *Polymer*, vol. Volume 107, p. 503–508, 2016.

[76] D. Huebner, V. Koch, B. Ebeling, J. Mechau, J. E. Steinhoff, and P. Vana, "Comparison of monomethoxy-, dimethoxy-, and trimethoxysilane anchor groups for surface-initiated raft polymerization from silica surfaces," *Journal of Polymer Science Part A: Polymer Chemistry*, vol. 53, no. 1, pp. 103–113, 2015.

[77] D. Huebner, *Design strategies for photoswitchable polymer nanocomposites*. PhD thesis, Georg-August University School of Science, 2016.

[78] K. S. J. K. Vahid Rashidi, Eleanor J. Coyle and K. P. Pipe, "Thermal conductance in cross-linked polymers: Effects of non- bonding interactions," *j. Chem. Phys. B*, vol. 21, no. 17, p. 4600–4609, 2017.

[79] B. Madan and T. Keyes, "Unstable modes in liquids density of states, potential energy, and heat capacity," *The Journal of Chemical Physics*, vol. 98, no. 4, pp. 3342–3350, 1993.

[80] G. Hartley, "The cis-form of azobenzene," *Nature*, vol. 140, p. 281, 1937.

[81] C. P. Jaana Vapaavuori, Josue Grosrenaud and C. G. Bazuin, "In situ photocontrol of block copolymer morphology during dip-coating of thin films," *ACS Macro Lett.*, vol. 4, pp. 1158–1162, 2015.

[82] T. Hugel, N. B. Holland, A. Cattani, L. Moroder, M. Seitz, and H. E. Gaub, "Single-molecule optomechanical cycle," *Science*, vol. 296, no. 5570, pp. 1103–1106, 2002.

[83] H. E. G. Lars V. Schäfer, E. Matthias Müller and H. Grubmüller, "Elastic properties of photoswitchable azobenzene polymers from molecular dynamics simulations," *Angew. Chem.*, vol. 119, 2007.

[84] M.-M. Russew and S. Hecht, "Photoswitches: From molecules to materials," *Advanced Materials*, vol. 22, no. 31, pp. 3348–3360, 2010.

[85] M. W. Matsen, "The standard gaussian model for block copolymer melts," *Journal of Physics: Condensed Matter*, vol. 14, no. 2, p. R21, 2002.

7 Acknowledgement

An dieser Stelle möchte ich mich bei allen Personen bedanken, die mich in der Anfertigung dieser Arbeit unterstützt und motiviert haben.

Zuallererst möchte ich meinen Dank an Herrn Prof. Dr Müller richten, für seine stets sehr gute Betreuung und Geduld. Dies hat einen großen Beitrag geleistet, dass ich diese Arbeit anfertigen konnte. In Ihrer Arbeitsgruppe konnte ich mich fachlich stetig weiter entwickeln und spannenden physikalischen, aber auch technischen Fragestellungen nachgehen. Besonders danke ich Ihnen auch für die Ihrerseits eingeräumten Freiheiten, um an anderen Projekten, die nur indirekt mit dem Thema der Dissertation verknüpft sind, mitzuarbeiten. Vielen Dank, dass Sie mich auf diesem Weg begleitet haben und meinen Spass an der Physik stets gefördert haben. Die Zusammenarbeit mit Ihnen wird mir sehr lange in positiver Erinnerung bleiben.

Mein Dank gilt auch den beiden weiteren Mitgliedern meines Betreuungsausschusses, Prof. Dr Cynthia Volkert und Prof. Reiner Kree. Frau Prof. Volkert Danke ich für die interessanten Einsichten in Experimente an Polymeren und die Bereitschaft auch weit über die bestehenden technischen Grenzen der Experimente hinaus zu gehen. Insbesondere bei der Messung mechanischer Eigenschaften von Polymeren - Reibung. Herrn Prof. Kree gilt mein Dank für die konstruktiven Gespräche und nützlichen Hinweise in den Treffen des Betreuungsausschusses.

Diese Arbeit wurde in innerhalb eines Teilprojekt (A03) eines Sonderforschungsbereiches (SFB 1073, Atomic scale control of energy conversion) erstellt. Mein Dank gilt daher allen Mitgliedern des SFBs für die tolle interdisziplinäre Zusammenarbeit und die Möglichkeit diese Arbeit in einem übergeordneten Konsens einordnen zu können. Speziell die Zusammenarbeit mit Dennis Hübner und Torsten Fornefeld, die komplexe Strukturen von Polymeren erstellen konnten, sowie mit Henning Ulrich und Florian Döring, die eine erstmalige thermische Messung an Polymer-Systemen ermöglichten, möchte ich dankend erwähnen.

Vielen Dank an alle Mitglieder der Arbeitsgruppe, insbesondere an Ludwig Schneider, Juan Orozco Rey, und die ehemaligen Mitglieder Fabien Leonforte

und Ulrich Welling, die mir in den Gruppen Seminaren mit der Erfahrung und Informationsbereitschaft aus Ihrer eigenen Arbeit, bei Problemstellungen immer behilflich gewesen sind. Für das Korrekturlesen dieser Arbeit möchte ich mich bedanken bei Tobias Binder, Isabel Köhler, Nele Monsen und Ludwig Schneider.

Vielen Dank auch an meine Bürokollegen: Simone Dresti, Luca Giorgetti und Stephan Breuer.

In der langen Zeit die ich in Göttingen verbringen durfte, hatte ich das Glück viele liebe, nette, tolle Menschen kennen lernen zu dürfen, sodass eine Erwähnung jedes einzelnen den Rahmen dieser Arbeit sprengen würde. Daher fühlt euch angesprochen und vielen Dank an euch!

Zum Schluss möchte ich meinen Eltern, meinem Bruder Tristan und dir Merle danken, ihr seid super.